Uncoupled Stability of Haptic Simulation of Viscoelastic Virtual Environments

by

Seanna Marie Oliver

A thesis submitted to the

Department of Electrical and Computer Engineering

in conformity with the requirements for

the degree of Master of Applied Science

Queen's University

Kingston, Ontario, Canada

November 2023

Copyright © Seanna Marie Oliver, 2023

Abstract

Haptic simulation systems enable users to kinesthetically interact with virtual environments through interaction with a robotic mechanism, known as a haptic device. Application of these systems are in medical simulators, robotic rehabilitation, and entertainment. Viscoelastic medium is a common environment that is simulated as a virtual environment (VE) in haptic simulation systems. Kelvin-Voigt (KV) and Hunt-Crossley (HC) are models commonly used to simulate viscoelastic environments in haptic simulation systems. Due to the sample-and-hold process, the range of dynamics - viscosity and elasticity, that can be rendered in a stable way is limited.

While uncoupled stability, as a stringent stability condition, has been analyzed for KV VEs, it has not been evaluated for HC environments. In this thesis, we experimentally evaluate the range of dynamic parameters for each model that result in uncoupled stability. To compare the results, we map the HC parameters to the KV parameter space. Results show that higher values of n_{HC} are more suitable for interactions with stiffer environments, at the expense of damping, and compared to the dynamic range obtained from using KV VE, the HC model offers lower stiffness but higher damping range.

To confirm the mapping, we conduct a user study to compare the viscosity and elasticity effects perceived by the users. Results show that different penetrations may not affect the stable HC elastic and viscous ranges, but it affects the feel of the HC modeled environment, as is reflected by the identified KV ranges, which confirms that the HC model is penetration dependent.

In addition to determining the stable implementable range of HC and KV parameters for non-deformable environments, the stable implementable range of physical deformable objects implemented as a VE is also found. Physical gels with known Young's Moduli are experimentally tested to determine their point of contact apparent stiffness and damping for varying penetration. These parameters are utilized to implement a spring-mass-damper mesh VE model for each gel. These values are also interpolated and extrapolated to implement a larger range of deformable VEs for uncoupled stability tests. The results show a viscoelastic dynamic range that depends on the depth of penetration.

Acknowledgements

I want to dedicate this milestone to my family and friends. I could not have done this without their support over the years. Thank you to my parents, siblings, and grandparents for always being there for me, and thank you to my friends, especially my housemates, who were always there to support me. I am very grateful and would especially like to thank my supervisor, Dr. Keyvan Hashtrudi-Zaad, for all of his support. I would also like to thank everyone at the BioRobotics and Autonomous Systems Lab for their support, especially Dr. Leonam Pecly, for his guidance and assistance. Finally, I am very grateful for the Queen’s community, who provided me with this opportunity and helped me to achieve this milestone.

Contents

Abstract i
Acknowledgements ii
Contents iii
List of Tables vi
List of Figures vii
Chapter 1 1
Introduction 1
1.1 Haptics Simulation Systems 1
1.2 Virtual Environments 2
1.2.1 Non-deformable Environments 2
1.2.2 Deformable Environments 5
1.3 Problem Definition 7
1.4 Proposed Solution 8
1.5 Contributions 9
1.6 Thesis Outline 9
Chapter 2 11
Uncoupled Stability Dynamic Range for Hunt-Crossley Modeled Virtual Environments 11
2.1 Uncoupled Stability with the HC Model 11
2.1.1 Experimental Setup and Procedure 11
2.1.2 Uncoupled Stability Results for a HC VE 13
2.2 Uncoupled Stability with the KV Dynamic Model 15
2.2.1 Dynamic Identification 15
2.2.2 Uncoupled Stability of a KV VE and Mapped HC Parameters 18
2.3 User Study 20
2.3.1 Procedure 21
2.3.1.1 Part I Procedure 24
2.3.1.2 Parts II and III Procedure 24
2.3.2 Results 25
2.3.2.1 Part I Results 26

2.3.2.2 Part II Results 27
2.3.2.3 Part III Results 28
2.4 Summary 28
Chapter 3 30
Uncoupled Stability Analysis of Haptic Simulation Systems for Varying Material Properties 30
3.1 Experimental Setup and Procedure 31
3.1.1 Materials 31
3.1.2 Experiment 33
3.2 Identification and Results 40
3.2.1 Parameter Identification 40
3.2.2 Experimental Results 46
3.3 Spring-Mass-Damper Mesh 49
3.3.1 Simulation Setup and Equations 49
3.3.1.1 Stiffness Equation Formulation 52
3.3.1.2 Damping Equation Formulation 55
3.3.1.3 Spring-Damper VE Implementation 59
3.3.2 Simulation Results and Analysis 60
3.3.2.1 Mesh Implementation Results in the Simulation 60
3.3.2.2 Mesh Simulation Results Comparison 63
3.4 Haptic Simulation System Implementation 66
3.4.1 Haptic Simulation System 66
3.4.2 Interpolated Dynamic Properties 67
3.5 Stability of Haptic Simulation System 71
3.5.1 Uncoupled Stability Experimental Procedure 71
3.5.2 Uncoupled Stability Results and Analysis 73
3.5.3 Validation Results and Analysis 77
3.6 Summary 80
Chapter 4 81
Conclusions 81
4.1 Summary 81
4.2 Future Work 82
Bibliography 84

Appendix A 89
Spring-damper Mesh... 89

List of Tables

Table 3.3.2-1: The mean (standard deviation) for each experiment for varying parameters across all users. 25

Table 4.1.1-1: Details of each fabricated gel. 33

Table 4.2.2-1: Fitted function equations for the stiffness data of each gel , and the %RMSE of the fitted function and the actual stiffness. 48

Table 4.2.2-2: Fitted function equations for the damping data of each gel , and the %RMSE of the fitted function and the actual damping. 49

Table 4.5.2-1: Stability results for varying damping and stiffness functions, shown with the initial stiffness and damping values of each function, for small penetration (0.01 m). The green combinations show stability, and the red combinations show instability. 74

Table 4.5.2-2: Stability results for varying damping and stiffness functions, shown with the initial stiffness and damping values of each function, for large penetration (0.02 m). The green combinations show stability, and the red combinations show instability. 74

Table 5.2-1: Parameters and their relation to the mesh components. 89

List of Figures

Figure 2.1-1: Two haptic devices. 1
Figure 2.1-2: A haptic simulation system, showing a user interaction with a mass-damper-spring virtual environment through a haptic device. 2
Figure 2.2.1-1: Parameter identification for KV using batch least squares. 4
Figure 2.2.1-2: Parameter identification for HC using batch least squares. 5
Figure 2.2.2-1: Needle being inserted into elastic tissue, modeled in FEM [22]. 6
Figure 2.2.2-2: Mass-spring-damper model with force being applied at a node [30]. 7
Figure 2.3-1: Haptic simulation system showing uncoupled stability, where the user does not have interaction with the haptic device. 8
Figure 3.1.1-1: Quanser Engineering Trainer (QET). The system runs at the sampling rate of 1 kHz. 12
Figure 3.1.1-2: Samples of system responses for uncoupled stable and unstable cases. 13
Figure 3.1.2-1: Experimental HC KHC and BHC values for (a) 2, (b) 5, (c) 10 deg penetration, for nHC from 1 to 2. 14
Figure 3.2.1-1: Block diagram of the identification process to map HC to KV parameters, where x is the fed position. 16
Figure 3.2.1-2: %RMSE values for the HC to KV mapping for nHC = 1 at 5 degrees penetration. 17
Figure 3.2.1-3: Maximum %RMSE values for various penetration degrees and exponents. 17
Figure 3.2.1-4: The forces from the experimental HC values for one set (KHC = 1.3, BHC = 0.3, nHC = 1), and from the mapped KV values (KKV = 1.3, BKV = 0.0261), and (b) their difference. 18
Figure 3.2.2-1: Mapped KV KKV and BKV values for (a) 2, (b) 5, (c) 10 deg penetration, for nHC from 1 to 2. 19
Figure 3.3-1: The user study setup. 21
Figure 3.3.1-1: The waveforms that users were asked to follow for each part of the study. 23

Figure 3.3.2-1: The percentage of participants who selected the correct environment for each part of the user study. 25
Figure 4.1.1-1: MACH-1 single axis load cell used for unconfined compression tests and the six samples that were used for this test. 32
Figure 4.1.1-2: The four gels fabricated. 33
Figure 4.1.2-1: Gel with center node on the side of the gel marked. The “plane” that the later simulations will be assuming it also outlined. 34
Figure 4.1.2-2: The interaction with the thin prodding device is shown by the thick vertical line. Three “planes” of the gel are show by the thin lines. 35
Figure 4.1.2-3: Experimental setup with Pantograph and gel. 36
Figure 4.1.2-4: Pantograph-gel interaction with the thin prodding device, captured with the Logitech camera. 36
Figure 4.1.2-5: Desired penetration of the Pantograph prodding device with the gel. 38
Figure 4.1.2-6: Experimental penetration results of each gel. 39
Figure 4.1.2-7: Experimental force results of each gel. 39
Figure 4.2.1-1: Data collected from the physical experiments for the E = 18.96 kPa gel. 40
Figure 4.2.1-2: Data separated into the modelling data for the E = 18.96 kPa gel. 41
Figure 4.2.1-3: Data separated into the validation data for the E = 18.96 kPa gel. 41
Figure 4.2.1-4: Unfiltered and filtered velocity shown for two cycles of the modelling data for the E = 18.96 kPa gel. 42
Figure 4.2.1-5: Stiffness found from batch LS for the E = 18.96 kPa gel. 42
Figure 4.2.1-6: Damping found from batch LS for the E = 18.96 kPa gel. 43
Figure 4.2.1-7: Averaged, then moving averaged filtered stiffness for the E = 18.96 kPa gel. 43
Figure 4.2.1-8: Averaged, then moving averaged filtered damping for the E = 18.96 kPa gel. 44
Figure 4.2.1-9: Averaged modelling penetration over time for the E = 18.96 kPa gel. 44
Figure 4.2.1-10: Averaged modelling force for the E = 18.96 kPa gel. 45
Figure 4.2.1-11: The actual modelling averaged force, the calculated force from stiffness and damping, and the force contribution of the stiffness and damping. 45
Figure 4.2.1-12: The actual validation averaged force and the calculated force from stiffness and damping. 46
Figure 4.2.2-1: Stiffness and damping results found from identification for each of the gels. 47

Figure 4.2.2-2: Data split up into penetration and retraction data, shown for the E = 18.96 kPa gel. 47
Figure 4.2.2-3: Stiffness and damping data (solid lines) and fitted functions (dotted lines) for each gel. 48
Figure 4.3.1-1: Spring-damper network and equivalent spring-damper. 50
Figure 4.3.1-2: Simple spring-damper network with single equivalent spring-damper. 51
Figure 4.3.1-3: Simple spring-damper network force breakdown. 52
Figure 4.3.1.1-1: Vertical spring breakdown. 53
Figure 4.3.1.1-2: Breakdown of the two top springs. 53
Figure 4.3.1.1-3: Breakdown of the two cross springs. 54
Figure 4.3.1.2-1: Vertical damper breakdown. 56
Figure 4.3.1.2-2: Breakdown of the two top dampers. 56
Figure 4.3.1.2-3: Breakdown of the two cross dampers. 57
Figure 4.3.1.3-1: Block diagram for the spring-mass-damper mesh simulation. 60
Figure 4.3.2.1-1: The graphics for the mesh (left) and equivalent spring-mass-damper (right). The manipulated node of the mesh is the top center node, and the manipulated node of the equivalent is the top node. 61
Figure 4.3.2.1-2: Block diagram showing the relationship between the physical gel experiments and the spring-mass-damper mesh simulation. 61
Figure 4.3.2.1-3: Mesh stiffness and damping for each spring-mass-damper in the mesh. 62
Figure 4.3.2.1-4: The penetration at the manipulated mesh node compared to that of the equivalent and the error between these two penetrations. 62
Figure 4.3.2.1-5: The simulated force, which is the same for the mesh and equivalent, compared to the actual force from the physical experiment. 63
Figure 4.3.2.2-1: Nodal locations, in metres, after deformation for the physical gel. The initial nodal locations are shown in red, and the nodal locations after deformation are shown in blue. The coordinates are given as the horizontal then vertical location. 64
Figure 4.3.2.2-2: Nodal locations, in metres, after deformation for the FEM gel model. This is the middle plane of the 3D FEM model. The coordinates are given as the horizontal then vertical location. 65

Figure 4.3.2.2-3: Nodal locations, in metres, after deformation for the mesh spring-mass-damper network. The equivalent spring-damper is also shown on the right of the mesh. The coordinates are given as the horizontal then vertical location. 66

Figure 4.4.1-1: Block diagram for the VE implemented on the Pantograph. 67

Figure 4.4.2-1: Identified and extrapolated, and interpolated stiffness for varying Young's Modulus values over penetration. The extrapolated parts and identified functions are represented by solid dots. The interpolated functions are represented by dashed lines. 68

Figure 4.4.2-2: Identified and extrapolated, and interpolated damping for varying Young's Modulus values over penetration. The extrapolated parts and identified functions are represented by solid dots. The interpolated functions are represented by dashed lines. 69

Figure 4.4.2-3: Position and force responses in the VE for smaller penetration. 70

Figure 4.4.2-4: Position and force responses in the VE for larger penetration. 70

Figure 4.4.2-5: Equivalent stiffness and damping responses in the VE for smaller penetration. 71

Figure 4.4.2-6: Equivalent stiffness and damping responses in the VE for larger penetration. 71

Figure 4.5.1-1: Stable and unstable position responses for low (left) and high (right) initial penetrations. 72

Figure 4.5.1-2: Force responses for stable and unstable cases for low (left) and high (right) penetrations. 73

Figure 4.5.2-1: Limits of stability for stiffness vs damping functions. The function sets are stable for all area under and including the stability limit points. 75

Figure 4.5.2-2: The physical gels shown in the stability range determined from the uncoupled stability testing. 76

Figure 4.5.2-3: Limits of stability for stiffness vs damping functions with data bars showing the range of stiffness of each of the stiffness functions. 76

Figure 4.5.3-1: Position and force data from the physical uncoupled stability tests. 77

Figure 4.5.3-2: Stiffness and damping found from identification, with the fitted functions. 78

Figure 4.5.3-3: Position and force responses in the VE for smaller penetration. 78

Figure 4.5.3-4: Position and force responses in the VE for larger penetration. 79

Figure 4.5.3-5: The validation gels shown in the stability range determined from the uncoupled stability testing. 79

Chapter 1

Introduction

1.1 Haptics Simulation Systems

Haptic simulation systems enable users to kinesthetically interact with virtual environments (VEs) that are graphically and dynamically rendered by a computer. This interaction is possible through manipulating a robotic mechanism, known as a haptic device. Two haptic devices that are used in this research are shown in Figure 1.1-1a [1] and Figure 1.1-1b [2].

(a) Quanser Engineering Trainer.

(b) Quanser Twin Pantograph.

Figure 1.1-1: Two haptic devices.

When a user interacts with a haptic device, the virtual environment provides force feedback to the user through the haptic device, to the amount that a real environment would apply to the user, as shown in Figure 1.1-2. This way the user would obtain a feel of interacting with a real environment.

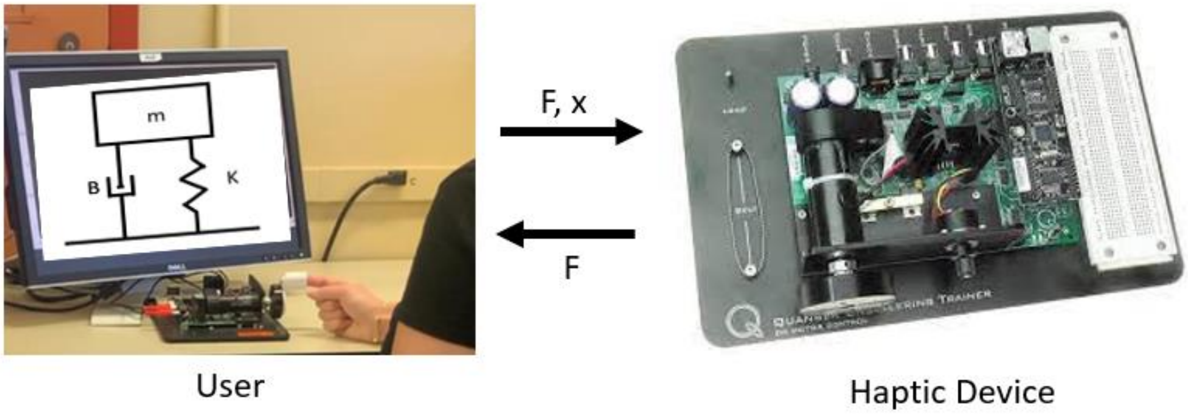

Figure 1.1-2: A haptic simulation system, showing a user interaction with a mass-damper-spring virtual environment through a haptic device.

Two applications of haptic simulation systems are robotic rehabilitation and medical training simulation [3] [4] [5] [6]. In the former, the patient tries to follow a desired trajectory while the patient's hand is constrained by virtual fixtures or is assisted. In other scenarios the user tries to move a virtual object from point A to point B [4]. In the latter, a surgeon-in-training practices a minimally invasive surgery procedure in a simulated environment [3] or receives training on administering epidural [6], or a sonographer-in-training practices ultrasound imaging from pre-scanned images from patients [5].

1.2 Virtual Environments

Virtual environments that mimic the behaviour of real environments are implemented as deformable or nondeformable models, which will be explained next.

1.2.1 Non-deformable Environments

Non-deformable objects are those in which the surface of interaction deforms uniformly, where all points of the object displace at the same rate, and by the same amount.

As the dynamic behavior of various objects include viscosity and elasticity, viscoelastic models are predominantly utilized to implement VEs. Kelvin-Voigt (KV) and Hunt-Crossley (HC) are two models commonly used to simulate viscoelastic environments in haptic simulation systems.

Spring-damper systems are the conventional method of implementing different environments [7] [8], as they can accurately represent deformable objects.

The linear viscoelastic KV model that will be implemented as VE in this thesis is presented as

$$f_{KV}(t) = \begin{cases} K_{KV}x(t) + B_{KV}\dot{x}(t) & x(t) \geq 0 \\ 0 & x(t) < 0, \end{cases} \tag{1.2.1-1}$$

where K_{KV} and B_{KV} are the KV stiffness and damping parameters, respectively.

Although KV is a linear damper-spring model [9] [10] and as such easy to implement [11] [12], it has physical inconsistencies in generating negative contact force during rebound [3] [13], making it less suitable for contact tasks with VEs displaying significant viscous behaviour [12] [14]. During rebound, when the device approaches the surface, the position reaches zero while the velocity is negative. As a result, the elastic term of the KV model approaches zero, whereas the viscous part of the model contributes to the negative contact force, which is not experienced in physical objects.

The non-linear HC model that will be implemented as a VE in this thesis is presented as

$$f_{HC}(t) = \begin{cases} K_{HC}x^{n}(t) + B_{HC}\dot{x}(t)x^{n}(t) & x(t) \geq 0 \\ 0 & x(t) < 0, \end{cases} \tag{1.2.1-2}$$

where K_{HC} and B_{HC} are the HC elastic and viscous parameters, respectively, $x(t)$ is the contact position, and n is the HC exponent which is between 1 and 2 and usually depends on the material properties.

HC is a nonlinear model that does not have the inconsistencies of the KV model [12] [15] [16]. This is because the damping related term is multiplied by the position. Therefore, HC does not have the negative contact force rebound inconsistencies since zero position will lead to zero VE force. As a result, the HC model may better represent environments with substantial viscous effect such as soft tissues [3]. Online and off-line identification methods have been proposed for HC parameter estimation [17].

When creating a VE from a physical object or environment, the elastic and viscous parameters of the model representing the environment need to be identified. When interacting with an environment and analyzing the environment, position and force data can be collected from the interactions. This data can be used for parameter identification to determine the dynamic model parameters. One such identification method is batch least squares. Batch least squares finds the optimal parameters to minimize the mean square of the prediction error over time using a regression matrix generated from a sliding window of the given data.

The LS process for a linear model such as KV is straightforward. For the KV model, the force can be expressed as

$$f_{KV} = K_{KV}x + B_{KV}\dot{x} = [K_{KV} \quad B_{KV}]\begin{bmatrix} x \\ \dot{x} \end{bmatrix} = \varphi\theta$$

where φ is the regression matrix, also known as H, and θ is the parameters matrix, which is what we aim to solve for. With L observations, the least squares solution would be

$$\theta = (\Phi^T\Phi)^{-1}\Phi^T F_{KV}$$

$$K_{KV} = \theta(1) = K$$

$$B_{KV} = \theta(2) = B$$

where $\Phi^T = [\varphi_1^T \ \ \varphi_2^T \dots \varphi_L^T]$ and $F_{KV} = [{F_{KV}}_1^T \ \ {F_{KV}}_2^T \dots {F_{KV}}_L^T]$. The process for identifying the KV parameters is shown in Figure 1.2.1-1.

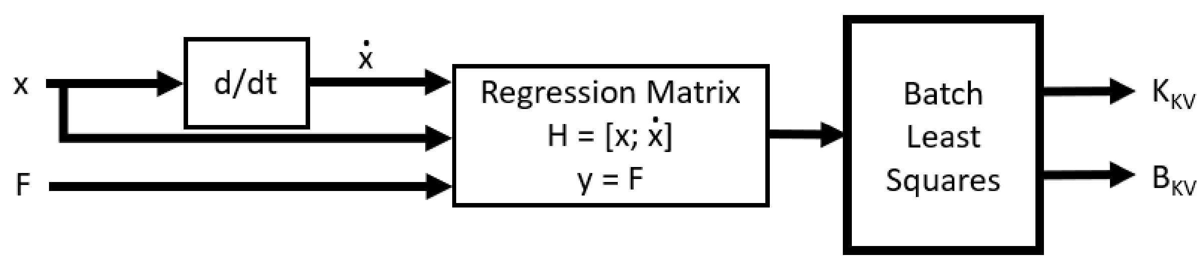

Figure 1.2.1-1: Parameter identification for KV using batch least squares.

Due to the nonlinearity of the HC model, its LS identification process is different [18]. For the HC model, the force can be expressed as

$$f_{HC} = K_{HC}x^n + B_{KV}\dot{x}x^n = [1 \quad \dot{x} \quad \ln{(x_{HC})}]\begin{bmatrix} \ln{(K_{HC})} \\ \frac{B_{HC}}{H_{HC}} \\ n_{HC} \end{bmatrix} = \varphi\theta$$

where φ is the regression matrix, also known as H, and θ is the parameters matrix, which we aim to solve for. This can be arranged to be

$\theta = F\varphi^{-1} = F(\varphi^T\varphi)^{-1}\varphi^T$

$K_{HC} = e^{\theta(1)} = e^{\ln(K_{HC})} = K_{HC}$

$B_{HC} = K\theta(2) = B_{HC}$

$n_{HC} = \theta(3) = n_{HC}$.

This process for identifying HC parameters is shown in Figure 1.2.1-2 [19]. This identification method is position-fed, where *x* is the position collected from interaction with the environment.

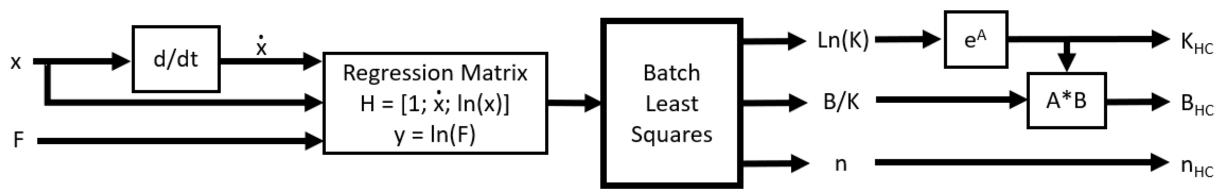

Figure 1.2.1-2: Parameter identification for HC using batch least squares.

1.2.2 Deformable Environments

Deformable objects are those in which upon excitation all the points within the object do not displace by the same amount. This implies that these objects project different elastic and viscous parameters depending on the depth of penetration during interaction [20] [21]. In order words, a deformable object is one where the VE dynamic behaviour changes during interaction [22].

Since these deformable objects cannot be modeled with the same model for all penetrations and types of interactions, other methods can be used. Two common methods include the finite element method (FEM) and the damper-spring mesh method. Both methods offer benefits and have downsides.

FEM is a method of simulating an object virtually by meshing the object into finite elements and determining the object response when undergoing deformation by analyzing the response of the finite elements. The FEM can accurately simulate the interaction among objects [23] [24]. However, this method is computationally expensive. In [25], FEM was used to model the interaction of a needle with elastic tissue, as shown in Figure 1.2.2-1. As can be seen from this figure, the tissue is meshed into finite elements, with the needle and area of interaction are modeled by a very fine mesh, to accurately capture this interaction, whereas the areas of the tissue further away from interaction, and therefore less affected by the interaction, are meshed with a larger mesh. The area closer to the interaction zone has more stress being applied to the individual elements compared to the area of the tissue further from the interaction, and therefore the mesh must be smaller in these higher-stress areas to allow the stress and movement to be accurately tracked.

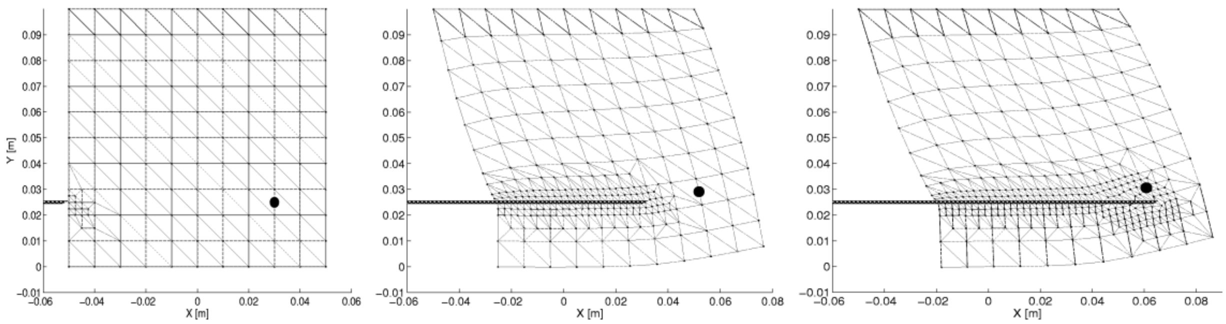

Figure 1.2.2-1: Needle being inserted into elastic tissue, modeled in FEM [25].

The damper-spring mesh is a much more common method for real-time interaction, as it can provide real-time feedback during interaction since it is computationally less expensive. However, this method is less accurate, as the elements are much larger than those of the FEM, and therefore more inconsistencies may appear. This method is also less accurate than FEM as each node in a 2D mesh, for example, can have a maximum of eight damper-spring attached to it to maintain a proper network, meaning that the force in each node is limited to eight directions, as opposed to the FEM, where each element considers the force in the entire element, and is not limited to a specific number of directions. The spring-damper mesh method consists of dividing up the object or environment into a network of damper-springs, which can be interacted with at any of the nodes. An example of this method can be seen in Figure 1.2.2-2, showing how an object can be represented with a damper-spring network providing a similar feel. When interacting with a damper-spring network, the point of contact must be at the nodes. These nodes can also have mass to represent the mass of a physical object the mesh may be representing. The damper-spring network has been used extensively in haptic simulation systems [26] [27] [28].

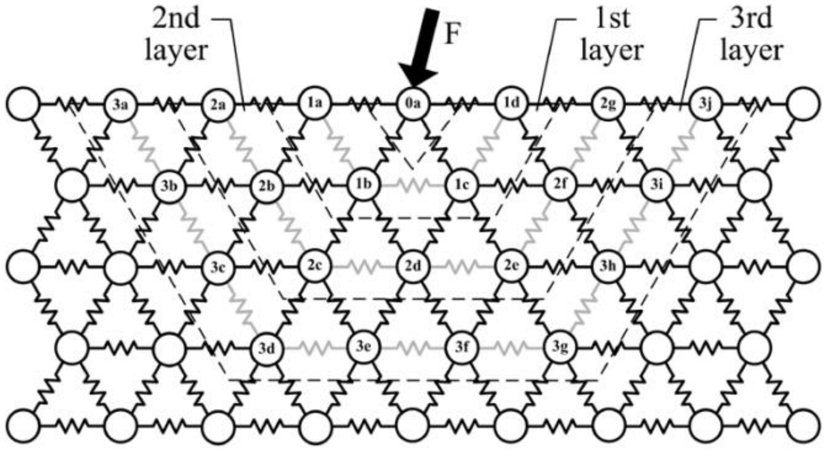

Figure 1.2.2-2: Mass-spring-damper model with force being applied at a node [29].

1.3 Problem Definition

Coupled stability of user and haptic simulation system is of paramount importance. Since human's interaction with passive real objects is stable, it is conjectured that the interaction between a user and haptic simulation system is stable as long as the haptic simulation system projects passive dynamics [30] [31].

Due to the sample-and-hold process, wherein continuous data is sampled for discrete time and held at the sample until the next sample is taken, the impedance projected by a haptic simulation system to a user may become non-passive for a certain range of VE dynamics. This results in coupled instability, which is caused by the output energy of the system being larger than the input energy of the system, which often occurs at high VE impedances and show itself as shaking or unwanted oscillations [32] [33]. Therefore, the range of the VE dynamics with which a user can interface in a stable manner becomes limited [11]. For example, in a medical simulator, stiffer viscoelastic environments, such as bone tissue, cannot be rendered in a stable way. This limitation may degrade the sense of realism, and as such the applications of these systems [32].

Uncoupled stability is a condition by which the system stays stable when the haptic device is not held by the user, as shown in Figure 1.3-1. Since users tend to stabilize their interaction with objects or systems they couple with, uncoupled stability is considered as a more stringent condition than coupled stability [11] [34] [35] [33]. Therefore, determining an uncoupled stability range will result in a more stringent range of dynamic parameters.

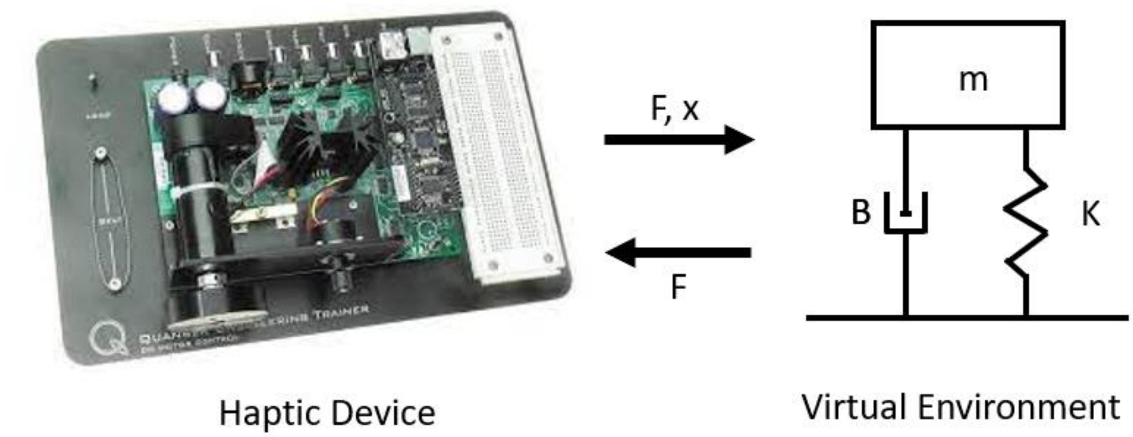

Figure 1.3-1: Haptic simulation system showing uncoupled stability, where the user does not have interaction with the haptic device.

1.4 Proposed Solution

Although the uncoupled stability range of the viscosity and elasticity components of the KV VEs, i.e., stiffness and damping, have been studied through analytical and experimental determination, such range has not been determined for the dynamic parameters of the discrete implementation of HC model. In this thesis, we will embark on experimentally investigating such a range for the HC model. Furthermore, since the interpretation of the dynamic parameters of the KV and HC models are different, we propose a means to determine the equivalent dynamic parameter in one model given the parameters of other model may help to better compare and interpret the results. We will also study how the KV and HC dynamic range will be perceived by the user.

In addition, uncoupled stability for deformable objects that demonstrate penetration dependent dynamics have not been investigated. We will experimentally study the uncoupled stability of deformable VEs modeled by spring-mass-damper mesh.

1.5 Contributions

This thesis studies the uncoupled stability condition for haptic simulation systems as an upper bound on the coupled stability condition for such systems. Through simulations and experimentations, the uncoupled stability dynamic range for viscoelastic non-deformable and deformable virtual environments have been identified.

The following are the specific contributions of this thesis:

1. Experimentally assess uncoupled stability for non-deformable viscoelastic environments modeled by Hunt-Crossley nonlinear. Use this nonlinear model to determine the uncoupled stability range of parameters.
2. Develop dynamic parameter mapping that maps the HC parameters to KV parameter space. Validate the mapping using a user study. Use this mapping to compare the HC uncoupled stability dynamic range to that of the KV model.
3. Experimentally investigate uncoupled stability for deformable objects modeled by damper-spring mesh.

1.6 Thesis Outline

The uncoupled stability dynamic range for Hunt-Crossley modeled virtual environments will be discussed in Chapter 2. The uncoupled stability with the HC model will be discussed, and an experiment will be proposed, and the results presented. The KV dynamic model will be reviewed, with a dynamic identification method proposed to allow comparison between this model and the HC model. A user study will be proposed to validate the conclusions made from the HC and KV model comparisons and the results of this study will be presented and discussed.

The uncoupled stability of haptic simulation systems for varying property materials will be discussed in Chapter 3. An experiment will be proposed to identify the stiffness and damping properties of a material. A virtual environment will be created with a haptic device to implement this mass-damper-spring mesh model and simulate the experimental interactions. Using FEM, the stiffness and damping properties of materials with varying properties will be determined, and these materials will be implemented in the virtual environment of the haptic simulation system. The uncoupled stability results of the various materials will be analyzed.

Chapter 4 will provide a summary of the information presented and draw conclusions. This chapter will also discuss how this work can be continued in the future.

Chapter 2

Uncoupled Stability Dynamic Range for Hunt-Crossley Modeled Virtual Environments

In this chapter, the uncoupled stability range of elasticity and viscosity will be determined through experiments for both the KV and HC models, and simulations will be used to produce the necessary data for identification, needed to map the dynamic parameters from HC to KV model. It will be shown that HC models offer lower stiffness, but larger damping range compared to KV models. A user study is also presented to verify the accuracy of the map between the KV and HC models as well as the user perception regarding the penetration variation. It will also be shown that varying the penetration may not affect the stable range of HC parameters, but it affects the feel of the HC modeled environment.

2.1 Uncoupled Stability with the HC Model

In this section, we will study the uncoupled stability results when an HC model is used to simulate a viscoelastic environment. Uncoupled stability analysis in discrete-time domain relies on the linearity of the system [12] [32]. Due to the inherent non-linearity of the HC model, the analytical study of uncoupled stability is a challenge. Therefore, we evaluate the uncoupled stability region experimentally. Next the experimental setup and procedures will be presented.

2.1.1 Experimental Setup and Procedure

The range of values for uncoupled stability for each VE were identified experimentally using a Quanser Engineering Trainer (QET), a one degree-of-freedom haptic platform, as shown in Figure 2.1.1-1a. A thimble fixture was 3D printed and has been installed on the QET wheel for the user study. The thimble was designed to provide users with a comfortable interaction. The distance from the thimble to the center is 34 mm. The setup is comprised of a Maxon DC motor with an incremental optical encoder (1,024 PPR). The maximum torque that the motor can generate is 0.055 Nm. The force at the thimble fixture was not measured, as the motor torque, found from the current, was monitored to ensure that the motor does not reach saturation.

However, given the maximum torque, the maximum force that could be expected at the end of the thimble fixture is 1.62 N, which will be considered in the user study. A 14-bit Quanser Q8 data acquisition board with QUARC software is used to command and measure the necessary signals at the rate of 1 kHz. The VEs were implemented bilaterally, and the discrete velocity was computed using the backward difference (BD) method. The QET dynamic parameters m = 2.3x10^{-5} kgm^2 and b = 1x10^{-4} Nms/rad, obtained through identification, is used in the simulations and analytical computations. Although the mass of the haptic device affects the uncoupled stability region, since the experiments were run only on one device (QET), with constant mass, mass was not a factor in our analysis.

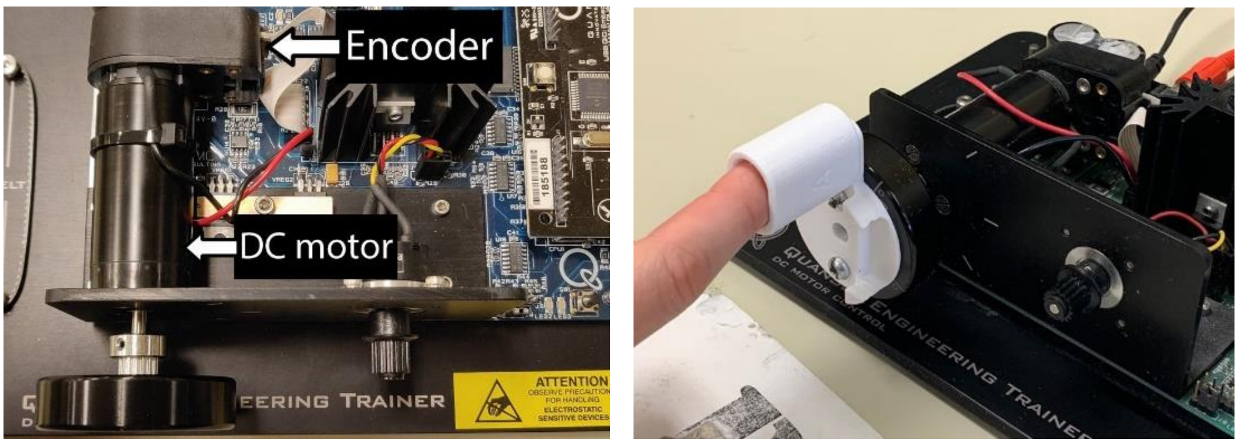

(a) QET components. *(b) QET with thimble fixture.*

Figure 2.1.1-1: Quanser Engineering Trainer (QET). The system runs at the sampling rate of 1 kHz.

As will be seen later, the range of K_{HC} vs B_{HC} depends on the chosen exponent and penetration. The penetration was implemented on the device as the amplitude of the step response. The specified penetration is used as the starting point for each experiment. For a given exponent and penetration, and for each B_{HC} value, the K_{HC} value was increased from zero until instability was reached and the B_{HC} value was increased from zero until no stable corresponding K_{HC} value existed, or saturation occurred. In our experiments, the penetration varied between 2, 5 and 10 degrees and the exponent varied among n_{HC} = 1, 1.25, 1.5, 1.75, and 2.

For the experiments on the QET, the system is considered stable if the position amplitude oscillation for the last 100 ms is less than 2% of the initial position since it was observed that for this system such oscillations will eventually phase out. The system is considered unstable if the states grow boundlessly or limit cycles are present. Figure 2.1.1-2 shows samples of system responses for the uncoupled stable and unstable cases.

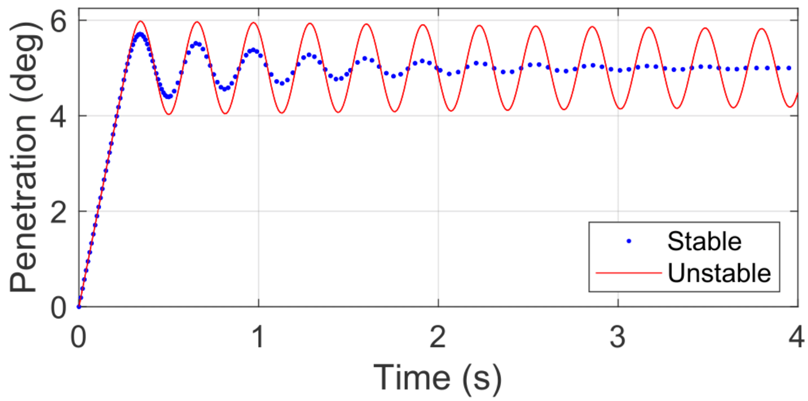

Figure 2.1.1-2: Samples of system responses for uncoupled stable and unstable cases.

2.1.2 Uncoupled Stability Results for a HC VE

Figure 2.1.2-1 shows the results for the varying penetration trials, with the HC experimental trials for three different penetrations, 2, 5, and 10 degrees, each with five values of n_{HC} = 1, 1.25, 1.5, 1.75, and 2. For the experimental HC ranges at different values of n_{HC} for each penetration, increasing n_{HC} did not noticeably change the values of B_{HC}, except for n_{HC} = 2, where it increased B_{HC} by about 50% of the other trials. However, increasing n_{HC} by 0.25 for each trial almost doubled the K_{HC} range for each consecutive trial. The K_{HC} and B_{HC} for corresponding n_{HC} values for each penetration are very similar. However, for low and zero viscosity, K_{HC} increases substantially as n_{HC} increases, particularly for the 2 degrees penetration trials.

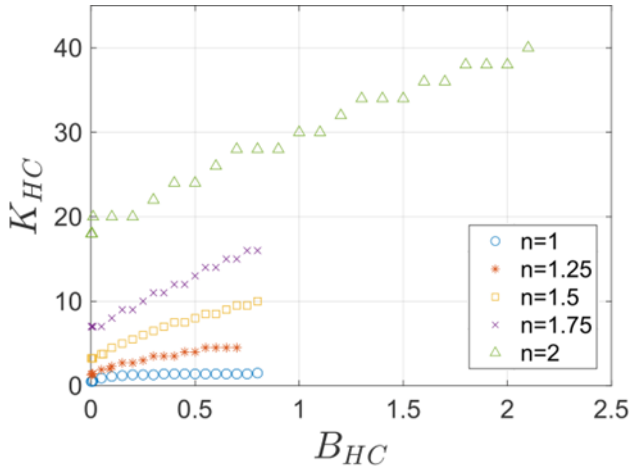

(a) 2 degrees K_{HC} and B_{HC}.

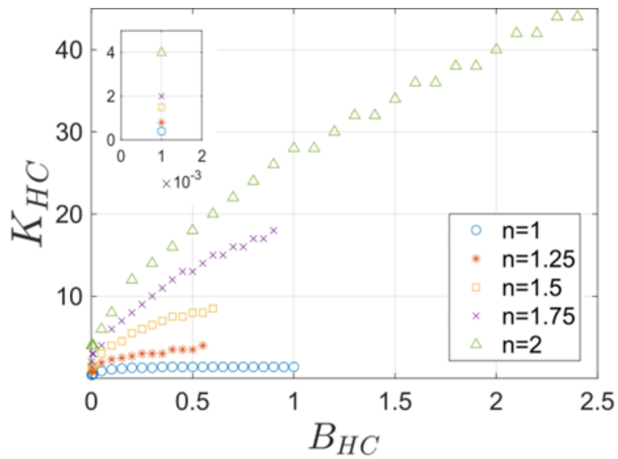

(b) 5 degrees K_{HC} and B_{HC}.

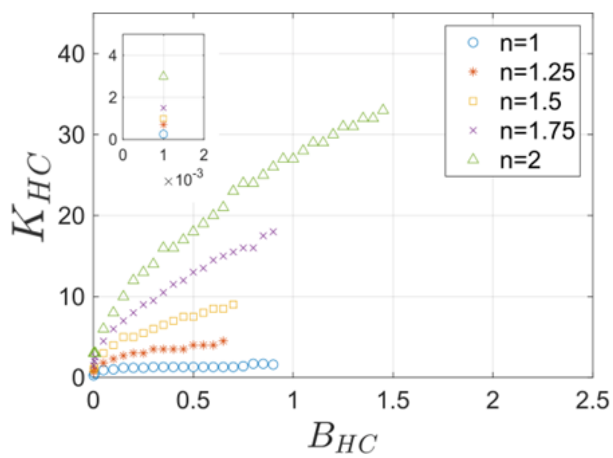

(c) 10 degrees K_{HC} and B_{HC}.

Figure 2.1.2-1: Experimental HC K_{HC} and B_{HC} values for (a) 2, (b) 5, (c) 10 deg penetration, for n_{HC} from 1 to 2.

This matter was investigated further through simulations for larger penetration range as well in [36] for only when elasticity is considered, i.e., $B_{HC} = 0$. The reported results shown that the maximum stable K_{HC} varies with the penetration $x(t)$ for n_{HC} > 1, and in fact it follows the relation

$$K_{HC}x^{n-1} = constant. \tag{2.1.2-1}$$

As depicted in [36], the maximum stiffness computed from the proposed relation *(2.1.2-1)* is very close to the ones obtained from our experiments. Therefore, we can conclude that the maximum stable K_{HC} for the elastic HC model is penetration dependant.

In the next section we will investigate two issues, i) how do the range of HC dynamic models found from uncoupled stability is perceived by a user, and ii) how does this range compare with the range obtained from a KV model?

2.2 Uncoupled Stability with the KV Dynamic Model

As presented in Chapter 1, KV is a linear dynamic model that directly relates the elastic and viscous feel of environments to tangible stiffness and damping parameters K_{HC} and B_{HC}, respectively. Therefore, in order to better interpret the range of elasticity and viscosity to be felt through the HC models obtained from the uncoupled stability experiments, we propose to map the HC parameters to the KV model parameter space. In this section, we will present a dynamic identification process to map the HC parameters to the KV parameter space, and the mapping results. We will also experimentally evaluate uncoupled stability when the VE is implemented as a KV model. A comparison between the KV parameter range and the equivalent KV parameters from the HC experiments sheds light on the range of stable viscoelasticity that each (HC and KV) model can support.

2.2.1 Dynamic Identification

Figure 2.2.1-1 shows the HC to KV parameter mapping block diagram, where HC parameter sets (K_{HC}, B_{HC}, n_{HC}) can be used to find their equivalent KV parameter set ($\widetilde{K}_{KV}$, $\tilde{B}_{KV}$) using a position-fed profile that generate a similar force in the least mean square error sense. Since the HC model is penetration dependent, the equivalent KV parameters may be influenced by the position profile.

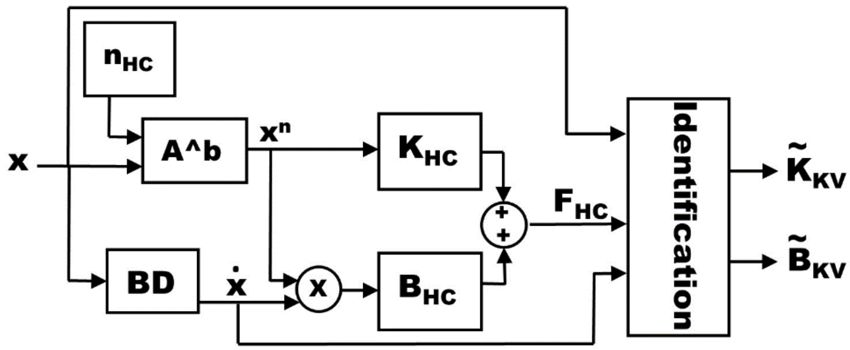

Figure 2.2.1-1: Block diagram of the identification process to map HC to KV parameters, where x is the fed position.

The dynamic identification is done through simulation, as opposed to experiment, as some of the HC parameters, although stable in the HC environment, may not produce equivalent KV parameters that are stable in the KV environment. In experiment, this instability will not allow proper identification. In simulation, instability does not occur, allowing proper identification.

In this work, the excitation signal used is the sum of two sinusoidal signals and a bias of 5 deg. The two sinusoidal signals have a peak-to-peak of 0.25 deg and the frequencies of 3 rad/s and 17 rad/s. The summed signal is then multiplied by 0.4, 1 or 2 to produce the desired penetration of 2, 5 or 10 deg, respectively.

Batch least squares was used for identification [19] [37]. The accuracy of the mapping process can be represented by the %RMSE (root mean square error)

$$\%RMSE = 100 * \frac{\sqrt{\Sigma\left(F - \hat{F}\right)^2}}{\sqrt{\Sigma F^2}}, \tag{2.2.1-1}$$

where F is the force generated from HC parameters and $\hat{F}$ is the force prediction from the identified KV parameters.

Figure 2.2.1-2 shows the mapping accuracy heatmap (%RMSE) for the range of stable B_{HC} and K_{HC}, for the 5 degrees of penetration trial at n_{HC} = 1. The maximum %RMSE of 0.53% occurs at maximum B_{HC} = 1. This is because, for n_{HC} = 1, the difference between the KV and HC models are in the viscous components.

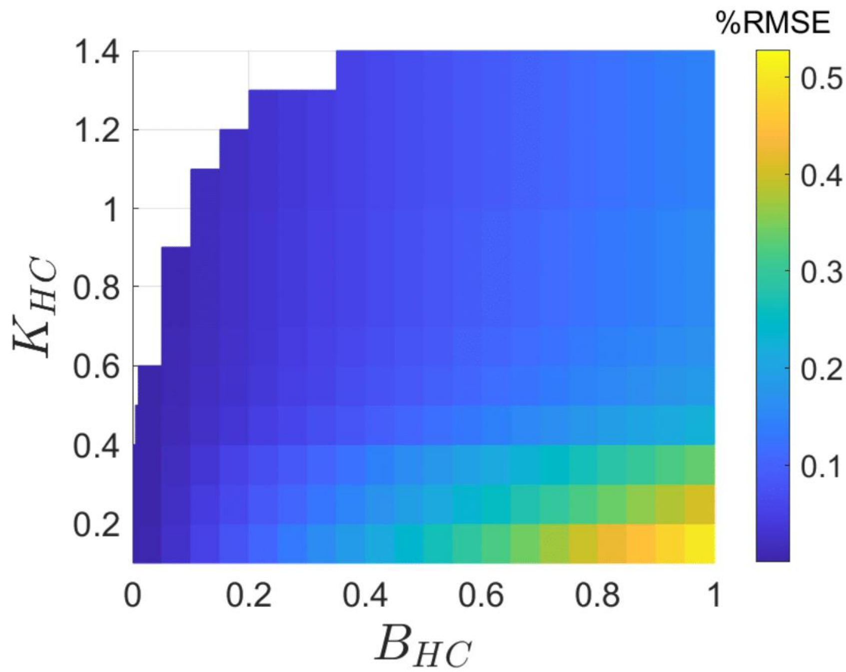

Figure 2.2.1-2: %RMSE values for the HC to KV mapping for n_{HC} = 1 at 5 degrees penetration.

Figure 2.2.1-3 shows the maximum %RMSE for various penetration degrees and exponents. As can be noticed, the mapping accuracy decreases as the penetration increases. In addition, the maximum occurs at the highest nonlinearity n_{HC} = 2.

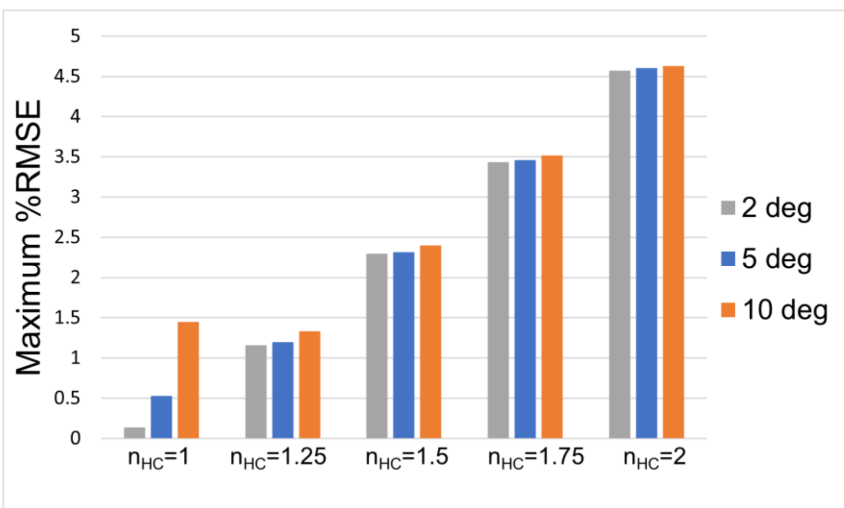

Figure 2.2.1-3: Maximum %RMSE values for various penetration degrees and exponents.

The experimental and mapped force values, generated from a set of dynamic parameters, and their difference are shown in Figure 2.2.1-4 for the 5 degrees at n_{HC} = 1. The force prediction error between the experimental HC and the mapped KV varied within ±1.5x10^{-4} N.

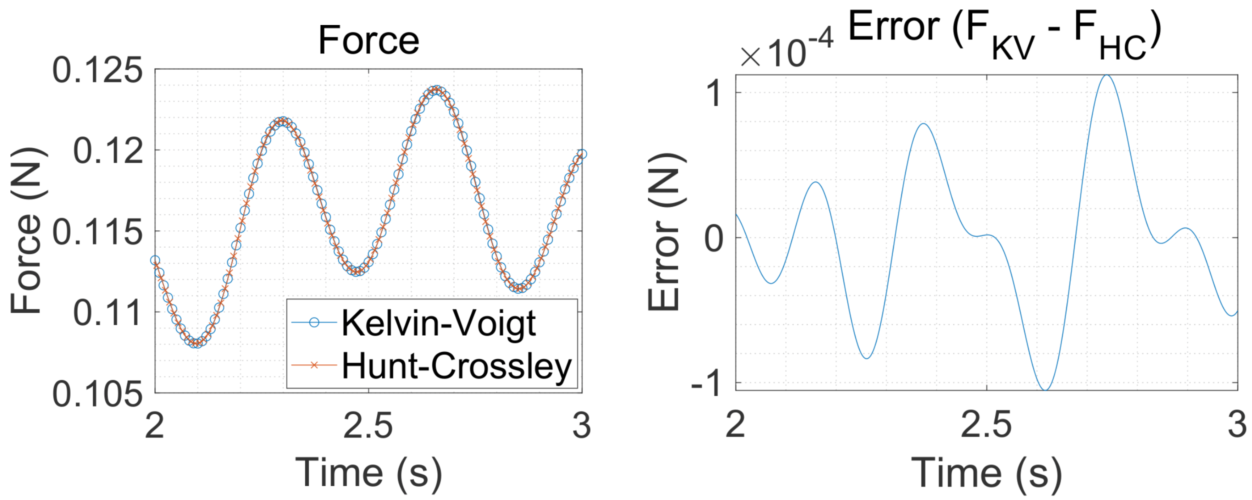

(a) HC and KV forces. *(b) Force difference.*

Figure 2.2.1-4: The forces from the experimental HC values for one set (K_{HC} = 1.3, B_{HC} = 0.3, n_{HC} = 1), and from the mapped KV values ($\tilde{K}_{KV}$ = 1.3, $\tilde{B}_{KV}$ = 0.0261), and (b) their difference.

2.2.2 Uncoupled Stability of a KV VE and Mapped HC Parameters

Figure 2.2.2-1 shows the equivalent KV values for each penetration, mapped from the corresponding HC values from Figure 2.1.2-1, using the identification process outlined in Figure 2.2.1-1. This mapping provides one set of KV parameters, $\tilde{B}_{KV}$ and $\tilde{K}_{KV}$, for each set of HC parameters, B_{HC}, K_{HC}, and n_{HC}, for each penetration, and therefore is valid for any set of HC parameters. The identification process does not provide a one-to-one mapping. The original HC parameters would not be obtained if the equivalent KV parameters obtained from Figure 2.2.1-1 were used in a reverse mapping as there is likely another set of HC parameters with different n_{HC} that would result in lower force error. However, if the n_{HC} is locked to its original value, then the original K_{HC} and B_{HC} will be recovered.

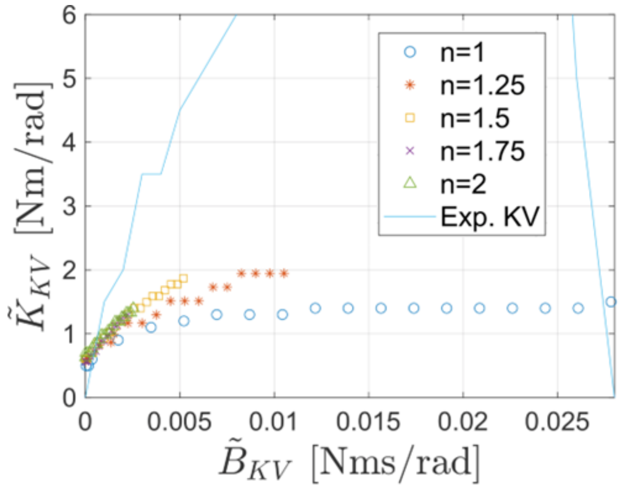

(a) 2 degrees $\widetilde{K}_{KV}$ and $\tilde{B}_{KV}$

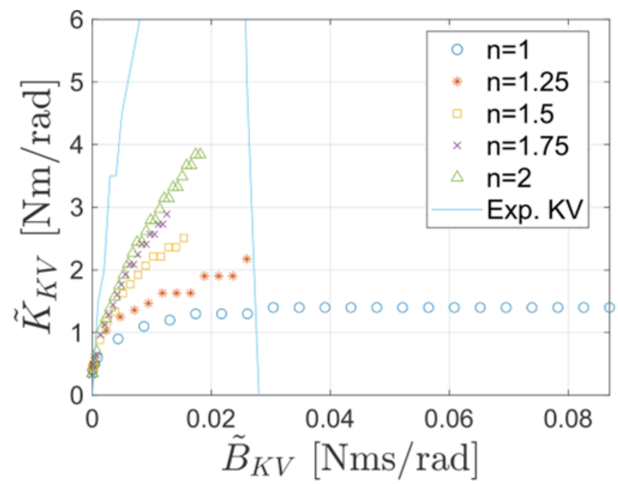

(b) 5 degrees $\widetilde{K}_{KV}$ and $\tilde{B}_{KV}$

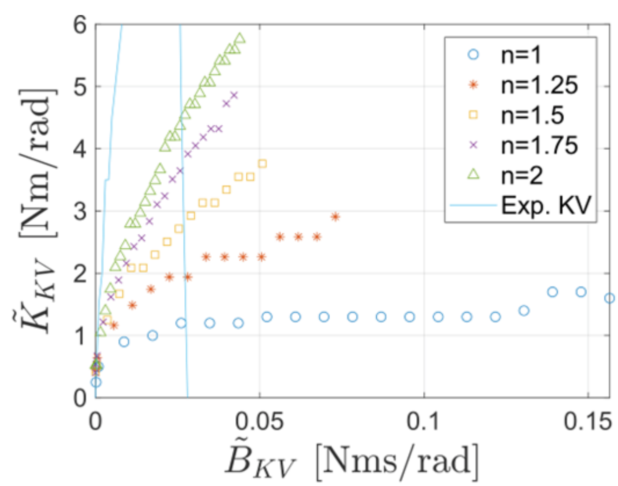

(c) 10 degrees $\widetilde{K}_{KV}$ and $\tilde{B}_{KV}$

Figure 2.2.2-1: Mapped KV $\widetilde{K}_{KV}$ and $\tilde{B}_{KV}$ values for (a) 2, (b) 5, (c) 10 deg penetration, for n_{HC} from 1 to 2.

This mapping process and results can be verified by comparing the HC and KV equations. Comparing the HC parameters from Figure 2.1.2-1 and the equivalent KV parameters from Figure 2.2.2-1, we can see that for n_{HC} = 1, the $\widetilde{K}_{KV}$ values are by and large similar to the K_{HC} values, because for n_{HC} = 1, the elastic terms of the HC and KV models require $\widetilde{K}_{KV}$ = K_{HC}. For n_{HC} = 2 the increase in $\widetilde{K}_{KV}$ is approximately proportional to the increase in the penetration, since $\widetilde{K}_{KV}$ = $K_{HC}x(t)$. For n_{HC} = 1, the increase in $\tilde{B}_{KV}$ is approximately proportional to the increase in the penetration, since $\tilde{B}_{KV}$ = $B_{HC}x(t)$. For n_{HC} = 2, the $\tilde{B}_{KV}$ values approximately increase by the square of the increase in penetration, as $\tilde{B}_{KV}$ = $B_{HC}x(t)^2$. For all penetrations between n_{HC} = 1 and 2, the $\widetilde{K}_{KV}$ and $\tilde{B}_{KV}$ values follow the same pattern with multipliers relative to the n_{HC} values.

The KV ranges for each of these varying penetrations are all different, showing that although the HC ranges may all appear to be the same across different penetrations, the feel of each are not actually the same. This is because the penetration makes a difference in the feel, which is not reflected by the HC ranges, but is reflected by the identified KV ranges.

From Figure 2.2.2-1a, it is clear that for 2 deg penetration, the HC model has a smaller equivalent implementable range of elasticity and viscosity compared to the KV model. From Figure 2.2.2-1b and Figure 2.2.2-1c, as penetration increases so does range of $\tilde{B}_{KV}$ to a point that at 10 deg penetration, HC offers a larger viscosity range for all n_{HC}. The same increasing pattern can also be observed for $\widetilde{K}_{KV}$. This suggests that HC models offer larger viscoelasticity range for uncoupled stability when the VE allows for larger penetrations such as in soft tissue simulations.

2.3 User Study

In the last section, we experimentally derived the range of HC and KV dynamic parameters for uncoupled stability and mapped the HC parameters to their equivalent KV parameter sets for comparison. In this section, we will focus on the dynamics that an HC model conveys to the user and the effect of penetration and the HC exponent on the dynamics felt.

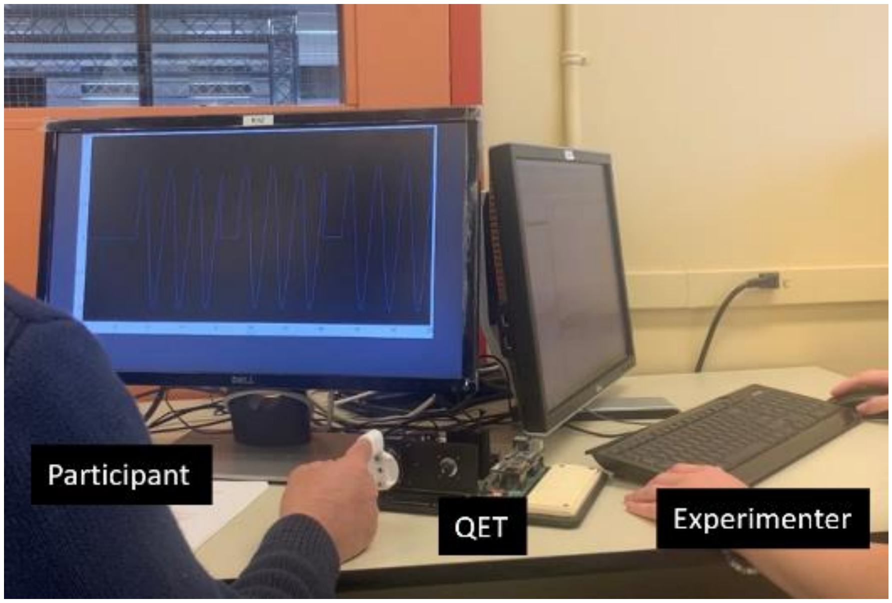

Figure 2.3-1: The user study setup.

We propose a three-part user study where the effect of penetration $x(t)$ on the HC environment impedance felt by the users could be gauged. The viscoelastic parameters chosen for each part of the user study were chosen such that the force applied a user's finger would not exceed the capabilities of the QET, which was limited to 1.62 N at the user's finger; however, the applied force was close to the maximum force, so that the user could feel enough force to accurately explore the environment. The knob on the QET would rotate to apply this force to the user. It is expected that for Part I, the feel of HC is penetration dependent, for all n_{HC} exponent values, and for Parts II and III, a human's feel of elasticity and viscosity follow the mappings discussed for stiffness and damping, for all penetrations and n_{HC} exponent values. The setup for the user study is shown in Figure 2.3-1. The participant was positioned so that they could not see what was displayed on the experimenter's screen.

2.3.1 Procedure

The user study experiment was broken down into three parts, and each part presented the participant with three different penetration environments (5, 10, and 20 deg). For each penetration, three different n_{HC} values were used (n_{HC} = 1, 1.5, 2). The participants were asked to follow a waveform, shown in Figure 2.3.1-1, displayed on the monitor in front of them by manipulating a knob with an attached thimble, as shown in Figure 2.1.1-1b. For the second and third parts of the user study, only one of these waveforms were shown at a time, depending on the desired penetration. The participants were asked to follow the waveform to the best of their ability. By following the waveform, the participants could interact with the VE. The participants were not made known of the expected results [38] and the participant could repeat any part of the experiment as many times as they needed to be certain of their decision [39] [40]. The viscoelastic parameters were chosen to avoid actuator saturation, and the velocity signal was low-pass-filtered to obtain a smooth signal. These measures in addition to the selected waveforms displayed in Figure 2.3.1-1 prevented any vibration or auditory cues that may bias the participant's answer. The same experimenter conducted the study for all participants to ensure uniformity [39] [40]. Upon receiving approval from the Queen's General Research Ethics Board (GREB), volunteer participants were recruited to contribute to the study.

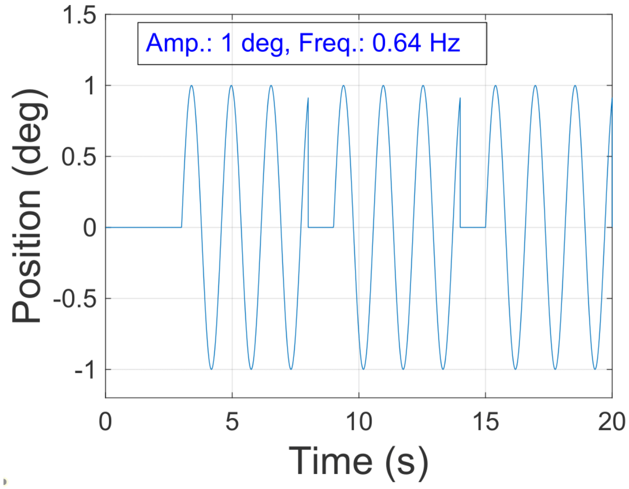

(a) Part I of the study.

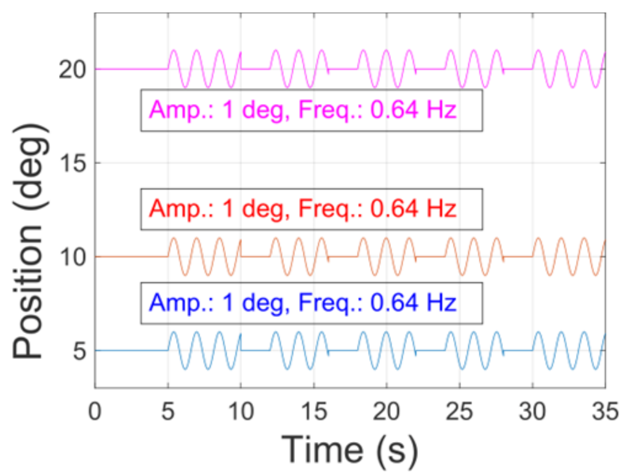

(b) Part II of the study.

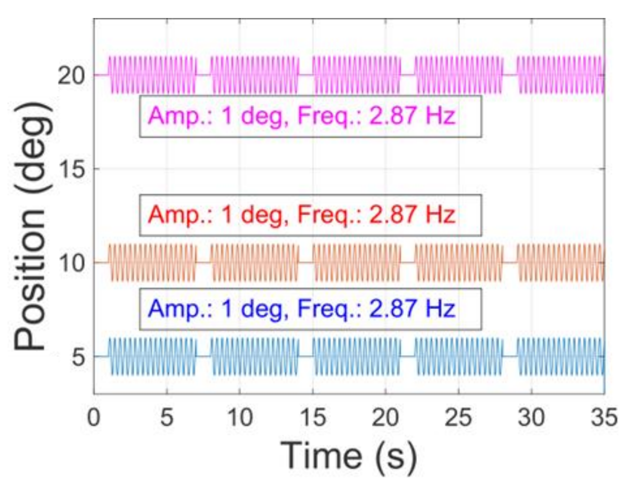

(c) Part III of the study.

Figure 2.3.1-1: The waveforms that users were asked to follow for each part of the study.

2.3.1.1 Part I Procedure

For the first part, the objective was to check whether the feel of HC is penetration dependent. For all trials, the K_{HC} and B_{HC} were kept at the same values. For each n_{HC} value, the participants were asked to rank the three penetrations from the lowest to the highest impedance. The expected results were that the 5 deg is the lowest, the 10 deg is medium, and the 20 deg is the highest. For each participant trial, the order of the penetrations presented was randomized.

2.3.1.2 Parts II and III Procedure

For these parts, the objective was to check whether a human's feel of elasticity and viscosity follows the mappings discussed for stiffness and damping. The participant was presented with five environments; the reference HC was presented, followed by three KV environments, then the reference HC was repeated at the end to provide the participant with an opportunity to check their answer. For the three KV environments presented, one of them is the KV equivalent of the reference HC, found from the identification process proposed in Section II. B. The other two were a certain percentage higher and lower. The percentage which was varied by participant was found through a calibration process. For each participant trial, these three KV environments were presented in a randomized sequence. The participants were asked which of these three KV environments was closest to the HC environment.

A calibration period was performed to identify the VE variation threshold of each participant. The control parameters used in the calibration were the 5, 10, and 20 degrees penetration trials for n_{HC} = 1. This is because, at n_{HC} = 1, the HC and KV models are the same for stiffness-only, and very similar for damping-only. Therefore, to calibrate the user, they needed to correctly identify this. For the stiffness-only part, the percentage started at 10%, and could increase by 10% increments up to a maximum of 60%. For the damping-only part, it was the same as the stiffness-only, but the percentage started at 20%. The starting percentages were chosen based on the just noticeable difference (JND), and the maximum was chosen to avoid large difference in feel.

For the calibration, the test was run for 5 degrees penetration, and the participants were asked if they could clearly feel a difference between the environments. If they could not, the percentage was increased, and the calibration restarted. If they could, they were asked to rank the three KV environments as low, medium, and high in terms of impedance, and asked to identify which they believed was closest to the HC environment. If they ranked incorrectly or chose the incorrect equivalent KV, the percentage was increased, and the calibration restarted. If they ranked correctly and chose the correct equivalent KV, they were tested for 10 then 20 degrees penetration, and the calibration restarted if incorrect for either. If they were correct for all penetrations or they were at the maximum percentage of 60%, regardless of their results, the calibration period was complete, and they would move on with the remainder of the part using that percentage.

For all three n_{HC} values and three penetrations (nine trials total), the process was repeated with different K_{HC} and equivalent K_{KV} values. The expected results were that the KV environment with the actual equivalent K_{KV} value was the closest. For the third part of the user study, the stiffness terms were set to zero, and the B_{HC} and B_{KV} environments were varied and explored.

2.3.2 Results

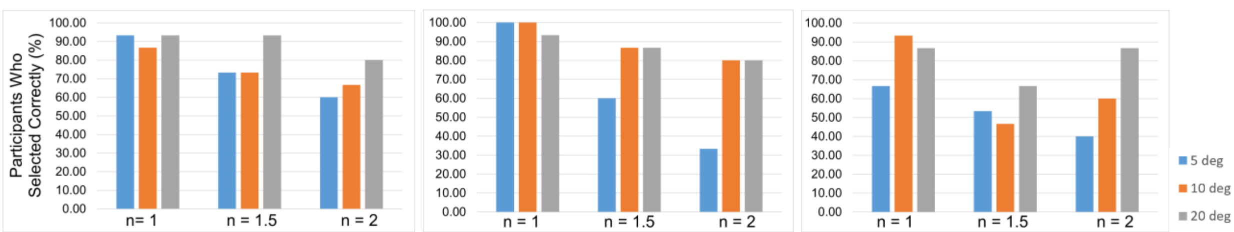

(a) Part I of the study. *(b) Part II of the study.* *(c) Part III of the study.*

Figure 2.3.2-1: The percentage of participants who selected the correct environment for each part of the user study.

Table 2.3.2-1: The mean (standard deviation) for each experiment for varying parameters across all users.

n_{HC}	Part I	Part II			Part III		
		5 deg	10 deg	20 deg	5 deg	10 deg	20 deg
1	2.73 (0.70)	1.0 (0)	1.0 (0)	0.93 (0.26)	0.67 (0.49)	0.93 (0.26)	0.87 (0.35)
1.5	2.4 (1.06)	0.6 (0.51)	0.87 (0.35)	0.87 (0.35)	0.53 (0.52)	0.47 (0.52)	0.67 (0.49)
2	2.07 (1.22)	0.33 (0.49)	0.8 (0.41)	0.8 (0.41)	0.4 (0.51)	0.6 (0.51)	0.87 (0.35)

The user study was conducted for 15 participants. The detailed results for each part of the study are illustrated in Figure 2.3.2-1. A z-test sample variation analysis was conducted to determine the validity of the results, based on differences in the rate of success (i.e., choosing the correct answer) between participants and experimental parameters. A significantly different environment means that participants had very different rates of success for the three varying parameters (n_{HC} = 1 vs 1.5 vs 2 or penetration of 5 vs 10 vs 20 deg). The minimum p-value threshold for the variation analyses was 0.05. For Part I, the variation analyses were conducted across users for varying n_{HC} values for the total success rates added across each penetration for each user. For Parts II and III, the variation analyses were conducted across users for varying penetrations for each n_{HC} value.

2.3.2.1 Part I Results

The participants were mainly successful at reaching the conclusion that 5 deg presented the lowest, 10 deg the medium, and 20 deg the highest impedance, since the average of correct answers for all participants for all trials was 80%. This demonstrates that the impedance displayed by the HC model is penetration dependent. As can be seen from Figure 2.3.2-1a, the users have the most success for n_{HC} = 1, and the least for n_{HC}. This is likely because, as n_{HC} increases, the interaction force decreases, and it becomes harder for users to discern the differences.

To further analyze the effect of exponent or model nonlinearity on the dependency detection, for each user and exponent we tallied the success for the three penetrations. This would result in three corrects for full success, one correct case for partial success, and zero correct cases for full failure. Table 2.3.2-1, column two, tabulates the averages and standard deviations over all users for a given n_{HC} value. A two-sample z-test has revealed no significant difference between n_{HC} = 1 vs 1.5 (p-value = 0.15) or n_{HC} = 1.5 vs 2 (p-value = 0.21), as they are rather similar, but demonstrated significant difference for n_{HC} = 1 vs 2 (p-value = 0.03) as they had a larger difference in their success rates.

To study the effect of penetration on success rate, as can be seen from Figure 2.3.2-1a, the success rate increases as the penetration increases. This is likely because as penetration increases so does the interaction force. In addition, the effect of n_{HC} on detection reduces for larger penetration. For example, the success rate for 20 deg penetration varies between 80% to 93%, whereas the rate changes between 60% and 93% for 5 deg of penetration.

2.3.2.2 Part II Results

For this part, where the participants were presented with elasticity, and asked to compare the HC VE with the equivalent KV VE, the participants were highly successful for n_{HC} = 1 or for higher penetrations. Table 2.3.2-1, columns three to five, tabulate the averages and standard deviations over all users for a given penetration for each value of n_{HC}. This demonstrates that the KV equivalent VEs are accurate representations of the stiffness-only HC VEs for these cases. The average percentage of the calibrated difference between environments for the participants was 44%.

As can be seen from Figure 2.3.2-1b, the users have the most success for n_{HC} = 1, and the least for n_{HC} = 2. This is likely because, for n_{HC} = 1, the HC and KV models for elastic-only environments are identical. As a result, the participants could easily perceive the correct equivalent KV model. For n_{HC} = 2, the HC has the highest nonlinearity.

To study the effect of penetration on success rate, as can be seen from Figure 2.3.2-1b, the success rate generally increases as the penetration increases. This is likely because as penetration increases so does the interaction force. In addition, the effect of n_{HC} on detection reduces for larger penetration.

A two-sample z-test has revealed that, for n_{HC} = 1, there were no significant differences between penetrations, with 5 vs 10 deg (p-value = 0.5), 5 vs 20 deg (p-value = 0.16), and 10 vs 20 deg (p-value = 0.16), as the force was the largest for this n_{HC} value; therefore, users could easily discern the differences, resulting in high rates of success. For n_{HC} = 1.5, 5 deg performed poorly, but 10 and 20 deg performed well, as the n_{HC} = 1.5, made the force smaller, but 10 and 20 deg provided more force than 5 deg penetration. Due to this, 5 vs 10 deg (p-value = 0.047) and 5 vs 20 deg (p-value = 0.047) were significantly different, but 10 vs 20 deg (p-value = 0.5) were not. This was the same for n_{HC} = 2, with 5 vs 10 deg (p-value = 0.002), 5 vs 20 deg (p-value = 0.002), and 10 vs 20 deg (p-value = 0.5); however, the rates of success were smaller, due to the even smaller force, especially for the 5 deg trials.

2.3.2.3 Part III Results

For this part, which was similar to Part II of the study, but with zero-stiffness VEs (i.e., damping only), the participants chose the correct equivalent KV environment 67% of the time, as opposed to 80% for the zero-viscosity case in Part II. Table 2.3.2-1, columns six to eight, tabulate the averages and standard deviations over all users for a given penetration for each value of n_{HC} . Therefore, this demonstrates that the KV equivalent VEs are accurate representations of the damping-only HC VEs, for n_{HC} = 1, or 20 deg penetration. The average percentage of the calibrated difference between environments for the participants was 55%.

As can be seen from Figure 2.3.2-1c, on average the users have the most success for n_{HC} = 1. This is likely because, for n_{HC} = 1, although the HC and KV models are not identical, they are the closest among all n_{HC} values. To study the effect of penetration on success rate, as can be seen from Figure 2.3.2-1c, the success rate generally increases as the penetration increases. This is likely because as penetration increases so does the interaction force. In addition, at high penetration, higher interaction velocity is possible which provides it easier for the users to feel the nature of viscosity.

2.4 Summary

In this chapter, the uncoupled stability conditions for a 1-DOF haptic simulation system using HC virtual environments were experimentally determined. In order to be able to compare the viscoelastic behavior offered by each model, a parameter mapping scheme was proposed to identify the equivalent KV dynamic parameters.

The mapped experimental uncoupled stability range for n_{HC} = 1, 1.25, 1.5, 1.75, and 2 at each penetration were determined, and it was found that for each individual penetration, the stiffness range increased slightly, and the damping range decreased significantly for each n_{HC} increment of 0.25. This suggests that higher values of n_{HC} are more suitable for interactions with stiffer environments, at the expense of damping. Compared to the dynamic range obtained from using KV virtual environment, the HC model offers lower stiffness but higher damping range.

To compare the difference in the feel of each model for different parameters, a user study was conducted. Varying the penetration showed that different penetrations may not affect the stable HC elastic and viscous ranges, but it affects the feel of the HC modeled environment, as is reflected by the identified KV ranges. This confirms that the HC model is penetration dependent, as the users could mostly discern the differences in penetrations in the HC VE for varying n_{HC} values.

Chapter 3

Uncoupled Stability Analysis of Haptic Simulation Systems for Varying Material Properties

In the previous chapter, we determined the uncoupled stability range linear and nonlinear models of non-deformable objects, in this chapter, we will look at the uncoupled stability range for deformable objects.

Four gels of varying Young's Moduli, resulting in varying stiffness and damping, were fabricated. These gels were used in an uncoupled interaction with a Quanser Planer Twin Pantograph haptic device. The position and force data from this interaction was collected.

This data was used in the batch least squares identification to determine the stiffness and damping properties of each gel over penetration. Functions were fit to each of these stiffness and damper results. Varying damping functions were interpolated between, and just above and just below these functions, and varying stiffness functions were interpolated above these functions.

To better represent the physical gels, a spring-damper network is proposed. This mesh maps the stiffness and damping functions for each penetration value to the stiffness and damping of each link in the mesh for each penetration value. An equation will be proposed to map the stiffness to the stiffness in each link of the mesh, and an equation will be proposed to map the damping to each link in the mesh.

A VE was implemented on the Pantograph for uncoupled stability testing, where the stiffness and damping functions were implemented with the mesh to produce the VE. This testing was conducted by finding the maximum stable stiffness function each damping function could accommodate. This test was conducted for both low and high penetration, as penetration is both a factor in the value of stiffness and damping each function reached, as well a factor in the stability of interaction. This produced a stable implementable range of stiffness and damping.

To validate this range, three additional gels of varying stiffnesses were used in the physical uncoupled penetration testing, and the stiffness and damping properties were again found with through identification. Stiffness and damping functions were fit to these three new validation gels. These stiffness and damping functions were compared to the determined implementable stability range. These stiffness and damping function pairs were then each implemented as the VE in the uncoupled stability testing, and the stability response, compared to the stiffness and damping properties of these new gels, validated the stable implementable range of stiffness and damping found.

3.1 Experimental Setup and Procedure

3.1.1 Materials

Four gels of varying Young’s Moduli were created for the testing. The gels were made of Super Soft Plastic from MF Manufacturing [41], and hardener of softener add-in. The ratios of Super Soft plastic to hardener or softener for specific Young’s Moduli was found from [42]. The first gel, with an expected Young’s Modulus of 18 kPa, was made with five portions of Super Soft Plastic and two portions of softener. The second gel, with an expected Young’s Modulus of 26 kPa, was made with five portions of Super Soft Plastic and one portion of softener. The third gel, with an expected Young’s Modulus of 55 kPa, was made with six portions of Super Soft Plastic and no other add-ins. The fourth gel, with an expected Young’s Modulus of 132 kPa, was made with four portions of Super Soft Plastic and two portions of hardener. These four gels, their material portions, expected and actual Young’s Moduli (E), and method of determining the actual Young’s Modulus is shown in Table 3.1.1-1.

Since very soft gels can be nonlinear [25], the Young’s Moduli of the E = 26 kPa gel was tested in an unconfined compression test, using small sample of the gel in a MACH-1 single axis load cell, shown in Figure 3.1.1-1a. A duplicate of this E = 26 kPa gel was made, and six small circular samples were cut out from this gel, as shown in Figure 3.1.1-1b.

(a) MACH-1.

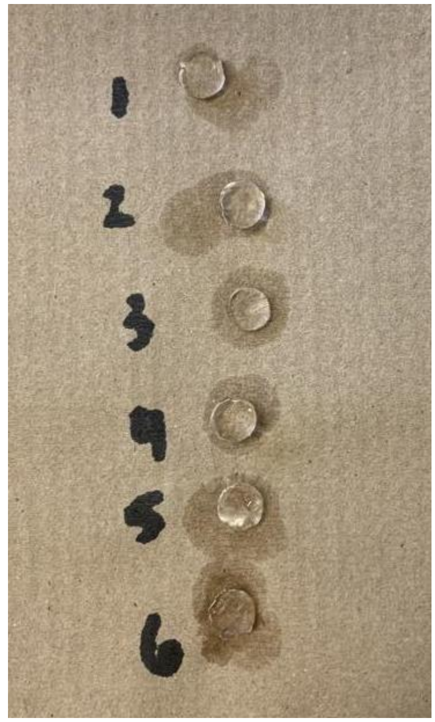

(b) Gel samples.

Figure 3.1.1-1: MACH-1 single axis load cell used for unconfined compression tests and the six samples that were used for this test.

Two trials were conducted with each of the six different samples from the gel. The data provided from this test was the position and force, which was used to find the stiffness of the trial, as

$$K = \frac{F}{x} \tag{3.1.1-1}$$

where K is the stiffness of the sample, x is the displacement of the load cell metres, and F is the force applied by the load cell in N. The stiffnesses found from each trial was averaged, and this averaged stiffness along with the averaged size of the samples was used to find the Young's Modulus, as

$$E = \frac{K_{avg} L_{avg}}{A_{avg}} \tag{3.1.1-2}$$

where K_{avg} is the averaged stiffness of all the trials, L_{avg} is the average thickness of all of the gel samples, and A_{avg} is the average area top face surface area of all of the gels.

The Young's Modulus found was 18.96 kPa, which is lower than the expected Young's Modulus of 26 kPa. This suggested that the gels with softener included did not have accurate expected Young's Moduli. Given the actual Young's Modulus of 18.96 kPa for one gel and given the Young's Modulus of 55 kPa for another, the Young's Modulus of the gel with two portions of softener was interpolated and found to be 16.05 kPa, as described in Table 3.1.1-1. These four gels are shown in Figure 3.1.1-2.

Table 3.1.1-1: Details of each fabricated gel.

Gel #	Portions of Softener	Portions of Super Soft Plastic	Portions of Hardener	Expected E from Literature (kPa)	Actual E (kPa)	Method of Determining Actual E
1	2	4	0	18	16.05	Interpolation with other actual E
2	1	5	0	26	18.96	Unconfined compression test
3	0	6	0	55	55	Literature
4	0	4	2	132	132	Literature

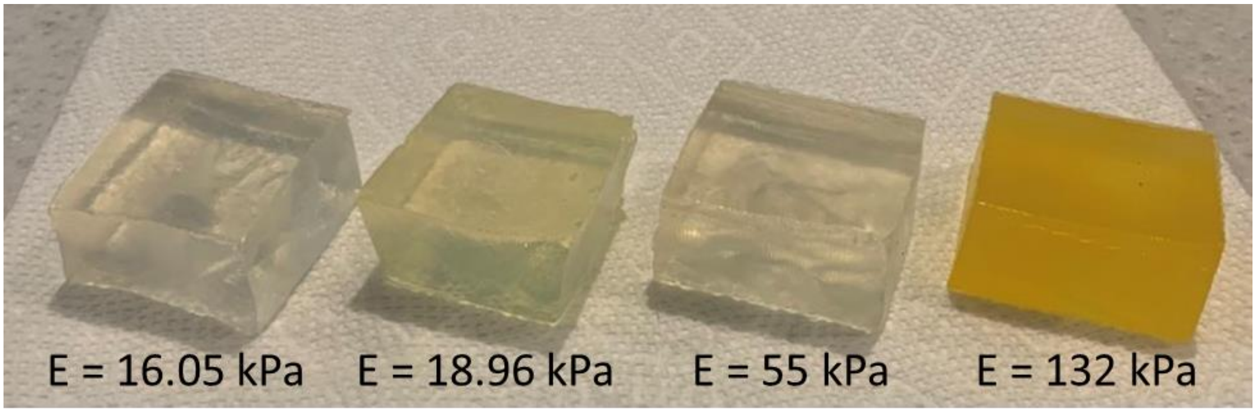

Figure 3.1.1-2: The four gels fabricated.

3.1.2 Experiment

To interact with the gels, a Quanser Haptic 3-DOF Planar Twin Pantograph, will be used. In the stability experiments, it will be assumed that the gel is planar, and the haptic interface was interacting with the center node on the side of the gel, as shown in Figure 3.1.2-1. To create this interaction with the Pantograph, a thin prodding device of the same height as the gel, 25 mm, and very thin, 2 mm, was 3D printed and fixed to the Pantograph, as shown in Figure 3.1.2-3. The interaction of this thin prodding device with the gel is shown in Figure 3.1.2-2, along with three “planes” of the gel. Since this thin prodding device will deform all three “planes” by the same amount apply the same force to each, and move at the same velocity, all three “planes” are identical, and can therefore be replace by one “plane” in the center, where a single point interaction can be used to replicate the thin prodding device interaction, as shown in Figure 3.1.2-1. The threads shown in this particular gel will be used for nodal tracking to validate the model.

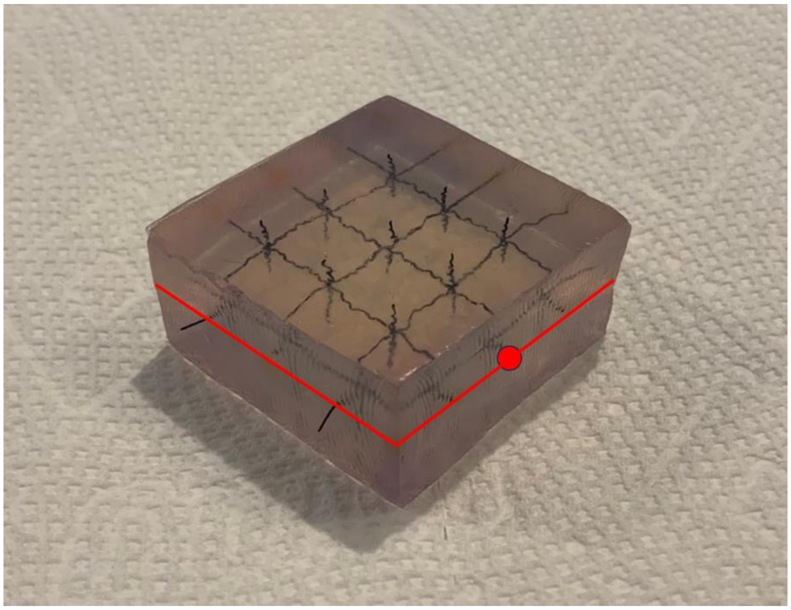

Figure 3.1.2-1: Gel with center node on the side of the gel marked. The “plane” that the later simulations will be assuming it also outlined.

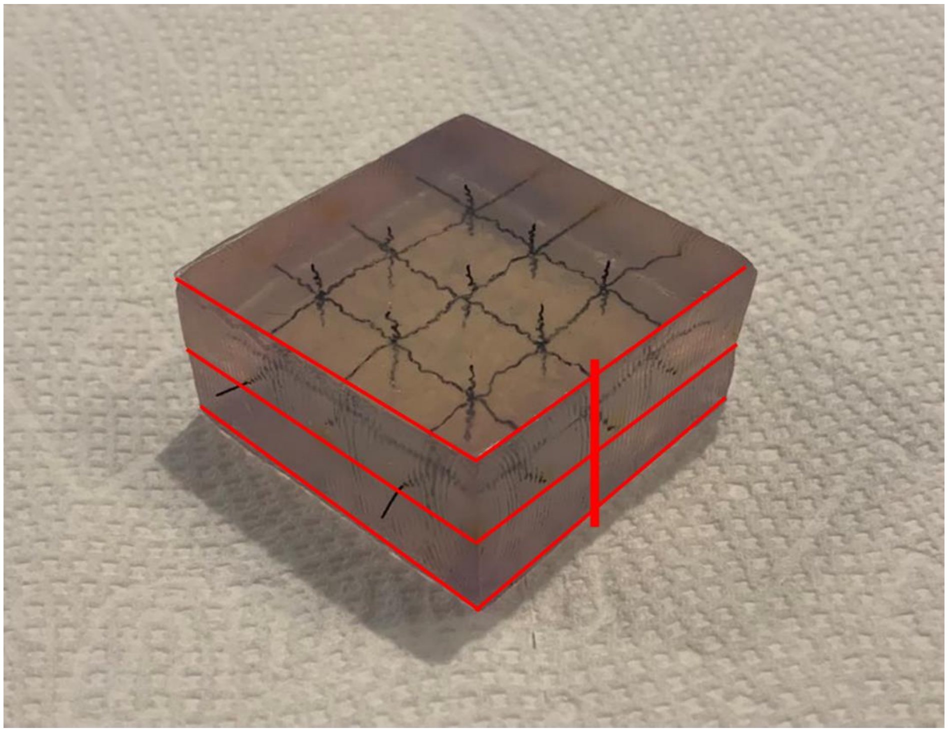

Figure 3.1.2-2: The interaction with the thin prodding device is shown by the thick vertical line. Three "planes" of the gel are show by the thin lines.

The Pantograph has two pantograph arms, as shown Figure 3.1.2-3, each with four links. Each arm has two direct-drive motors, and the encoders associated with these motors have 20k lines of count per revolution [43]. The Pantograph is capable of applying a maximum force of 3.1 N in the x-direction, and 2.3 N in the y-direction [44], which is the direction we are concerned with. During testing, the bottom and back of the surface where the gel rested was oiled, as well as the prodding device, to allow to gel to deform without any friction. An ATI Nano-25 force/torque sensor was fixed on the Pantograph before to prodding device to measure and record force data from the gel interaction. A Logitech camera was fixed over the setup to record the Pantograph-gel interaction, shown in Figure 3.1.2-4, to monitor the movement of the gel during interaction, which can be used for nodal tracking.

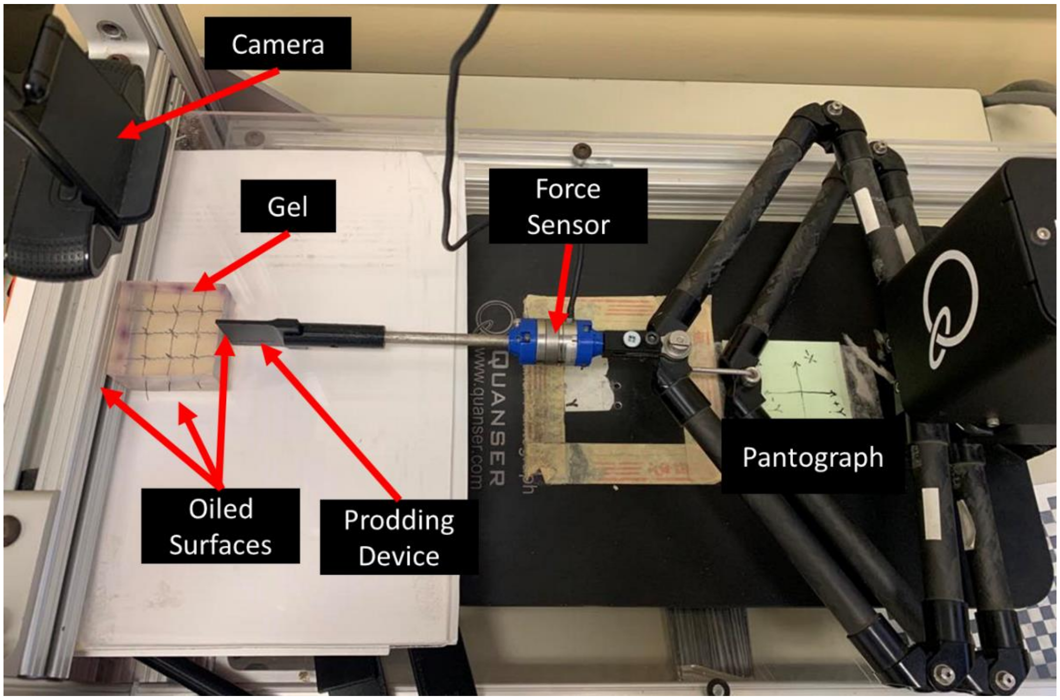

Figure 3.1.2-3: Experimental setup with Pantograph and gel.

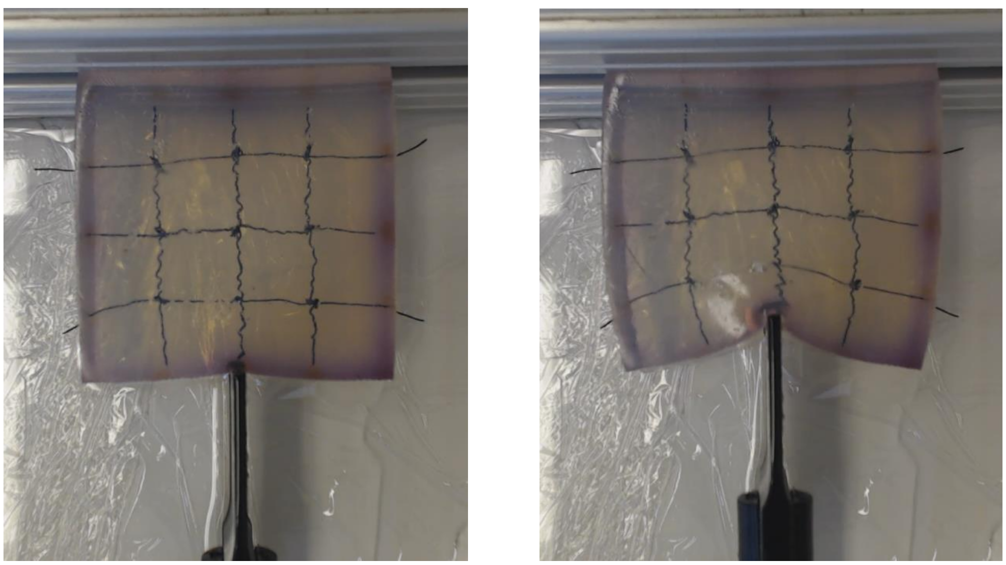

(a) Initial contact. *(b) Maximum penetration.*

Figure 3.1.2-4: Pantograph-gel interaction with the thin prodding device, captured with the Logitech camera.

When testing the haptic interaction with the gels, it was found that upon exiting and re-entering interaction with the gel, the contact force was inaccurate, so the stiffness and damping parameters during this contact were unrealistically large. To avoid this inaccuracy, the

Pantograph made to penetrate the gel to a point past what could be considered the initial contact, around 4 mm, then began the data collection and conducted multiple penetration cycles with the gel while never retracting past 4 mm. Since stiffness is penetration-dependent, the Pantograph was made to have a large range of penetration, from the initial 4 mm to 20 mm, which was the maximum the Pantograph could penetrate before reaching saturation. The damping is velocity-dependent, so in addition to the large penetration range implemented, overlaying signals with different frequencies were included to create a rich velocity profile for the damping identification. The desired position of the Pantograph over time is shown in Figure 3.1.2-5 for two cycles, and the three signals which were summed together are

$$y(t) = |0.018\sin\left(\frac{2\pi}{5}(t\text{-}10)\right)| + 0.002\sin(2\pi * 7t) + 0.0015\sin(2\pi * 13t) + 0.005; \quad (3.1.2\text{-}1)$$

where *y(t)* is the position in metres outputted to the Pantograph as a function of time, *t*, in seconds. The first function was added to control the length of each penetration cycle, and the depth of penetration reached. The additional functions added to create a rich velocity profile have vary frequencies that are not harmonics with different amplitudes to create a very rich function. This bias of 0.005 m was added to ensure contact with the gel was all maintained, and the prodding device never exited contact with the gel. This is because on initial contact with the gel, the initial contact force is very large, resulting in a very stiffness associated with initial contact, which does not correctly define the actual stiffness of the gel.

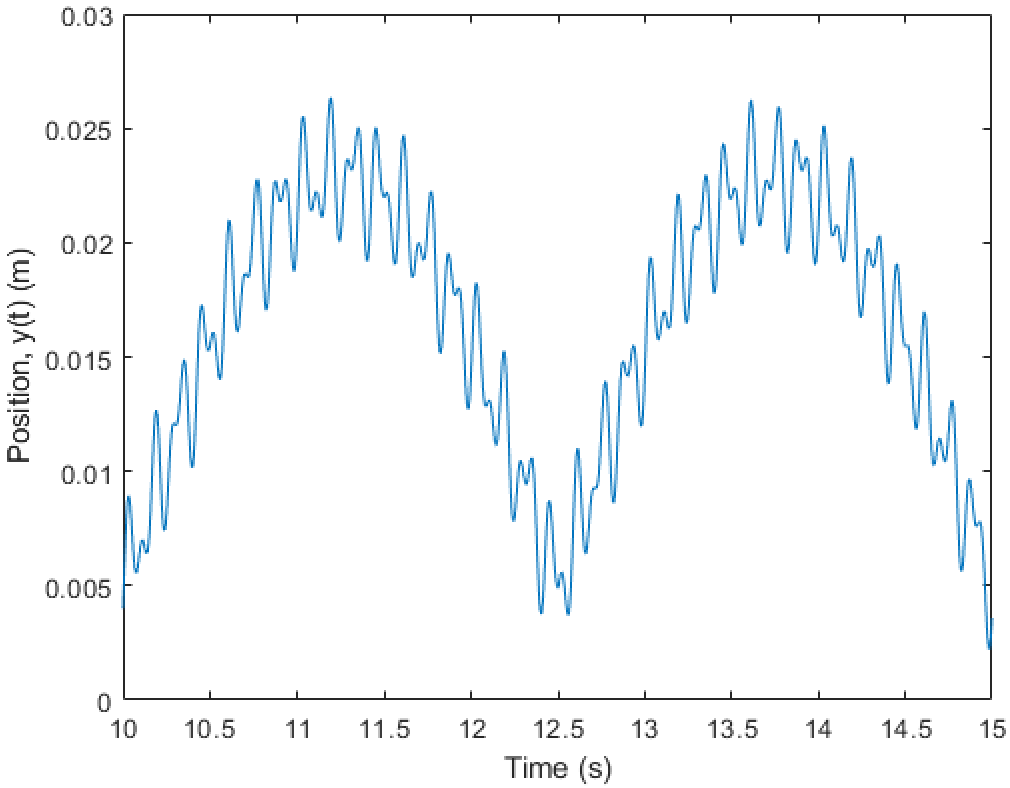

Figure 3.1.2-5: Desired penetration of the Pantograph prodding device with the gel.

The penetration of each gel is shown in Figure 3.1.2-6 and the corresponding force from each gel test is shown in Figure 3.1.2-7. As can be seen from these figures, multiple cycles of penetration and retraction were conducted to provide more data for the identification, as well as allow for the data to be split into identification and verification data. The sampling frequency was $1x10^3$ samples/second.

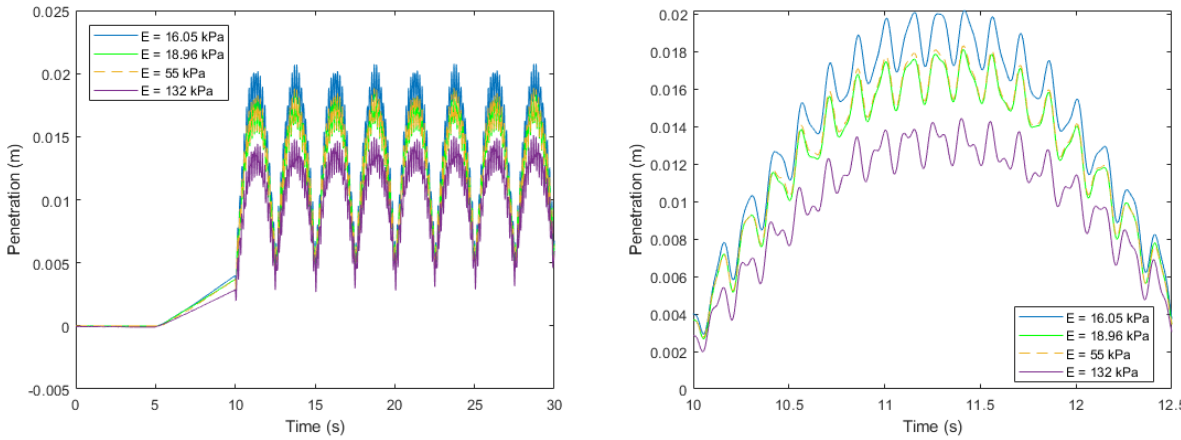

(a) All cycles.

(b) Single cycle.

Figure 3.1.2-6: Experimental penetration results of each gel.

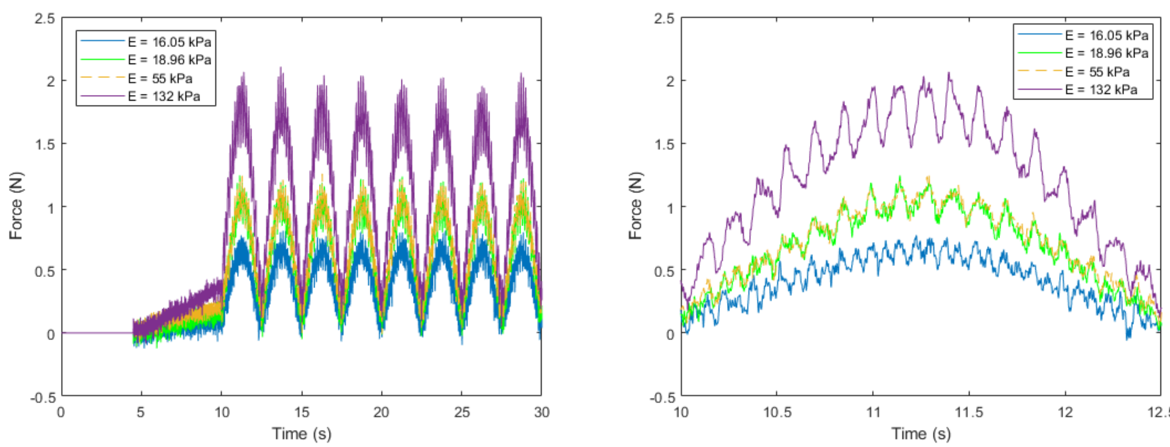

(a) All cycles.

(b) Single cycle.

Figure 3.1.2-7: Experimental force results of each gel.

Although all of the gel experiments had the same position signal controlling the Pantograph, the E = 16.05 kPa gel had the highest penetration, followed by the E =18.96 kPa gel, the E = 55 kPa gel, and finally the E = 132 kPa gel with the lowest penetration. The E = 16.05 kPa gel had the lowest force, followed by the E = 18.96 kPa gel, the E = 55 kPa gel, and finally the E = 132 kPa gel with the highest force. This is because the E = 16.05 kPa gel was the softest, so it could penetrate almost the full amount of the desired penetration with the least amount of force required. The E = 132 kPa gel was the stiffest, so it could not penetrate close to the full amount of the desired penetration, and it required the most force of all the gels to even penetrate the small amount that it did. Therefore, it is clear already from the feel of the gels, and the penetration and force requirements that the E = 16.05 kPa gel is the softest, so it should have the lowest stiffness, followed by the E = 18.96 kPa gel, the E = 55 kPa gel, and finally the E = 132 kPa gel appears to be the stiffest and should have the highest stiffness.

3.2 Identification and Results

3.2.1 Parameter Identification

The data collected from the experiments with the physical gels was used in batch least squares (LS) identification. The position and force data collected from the physical experiment for one gel is shown in Figure 3.2.1-1. The first ten seconds of data was removed, as this was the time when the Pantograph was initially penetrating the gel.

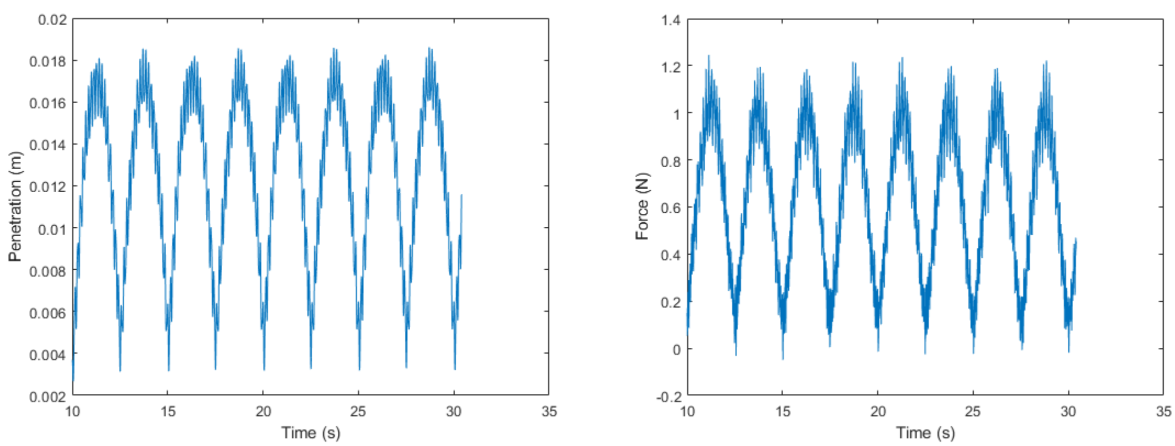

(a) Penetration data.

(b) Force data.

Figure 3.2.1-1: Data collected from the physical experiments for the E = 18.96 kPa gel.

The first step of the data processing was to separate the data into modelling, Figure 3.2.1-2, and validation, Figure 3.2.1-3, data. The modelling data will be used for the identification, and the validation data will be used for verification.

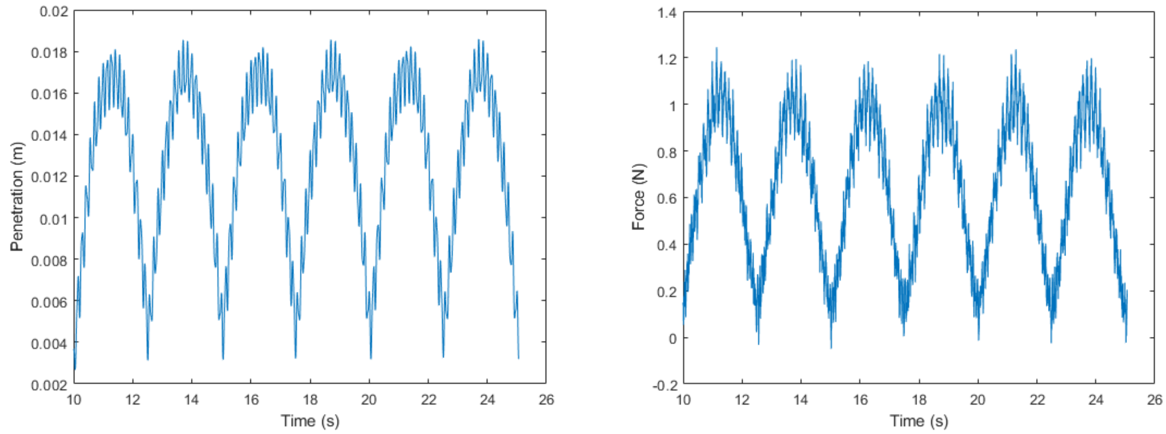

(a) Penetration data. *(b) Force data.*

Figure 3.2.1-2: Data separated into the modelling data for the E = 18.96 kPa gel.

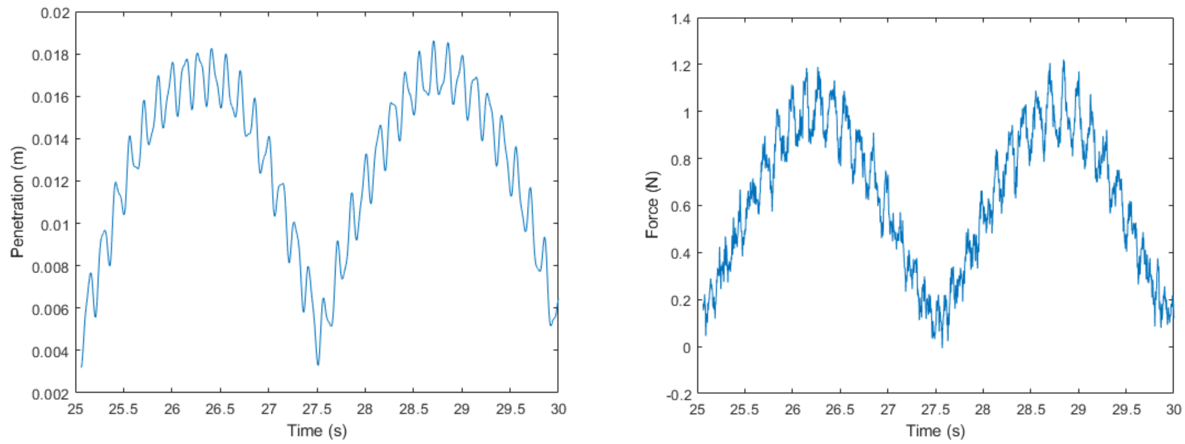

(a) Penetration data. *(b) Force data.*

Figure 3.2.1-3: Data separated into the validation data for the E = 18.96 kPa gel.

The velocities were found for both the modelling, Figure 3.2.1-4a, and validation data using BD, and filtered using a low-pass filter of passband frequency 60 Hz, Figure 3.2.1-4b, and are shown for just two cycles.

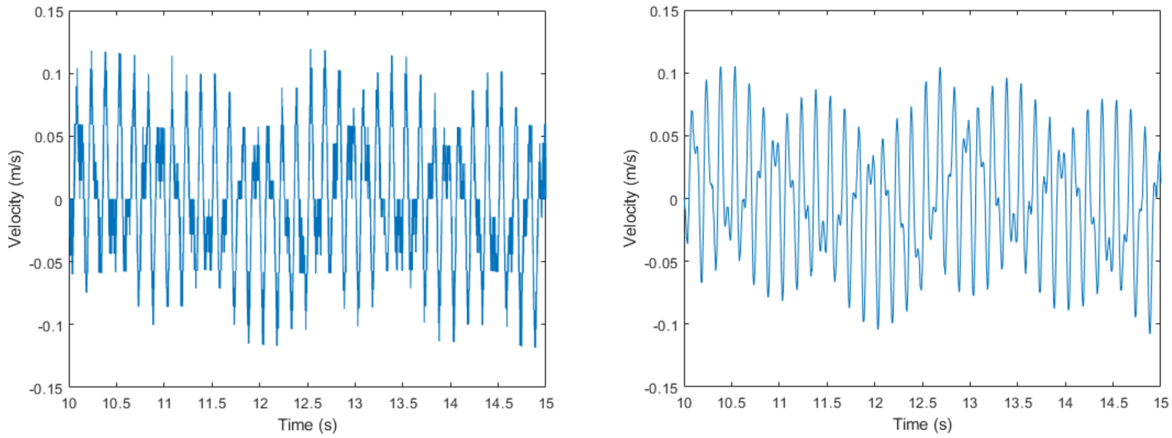

(a) Unfiltered velocity. *(b) Low-pass filtered velocity.*

Figure 3.2.1-4: Unfiltered and filtered velocity shown for two cycles of the modelling data for the E = 18.96 kPa gel.

To process the experimental data, batch least squares identification was conducted to determine the optimal stiffness and damping fits for the gel. The modelling data was used for this identification, and the unfiltered stiffness results are shown in Figure 3.2.1-5 and the damping in Figure 3.2.1-6. The sliding window used in the batch least squares had a window size of 100 samples, out of about 15k samples, since the sampling frequency was $1x10^3$ samples/second, and there is about 15 s of modelling data.

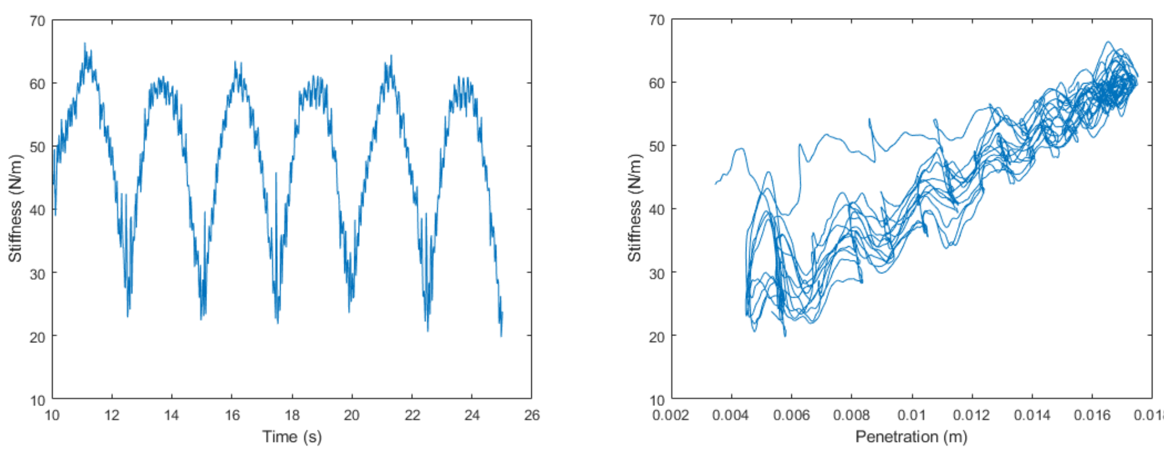

(a) Stiffness over time. *(b) Stiffness over penetration.*

Figure 3.2.1-5: Stiffness found from batch LS for the E = 18.96 kPa gel.

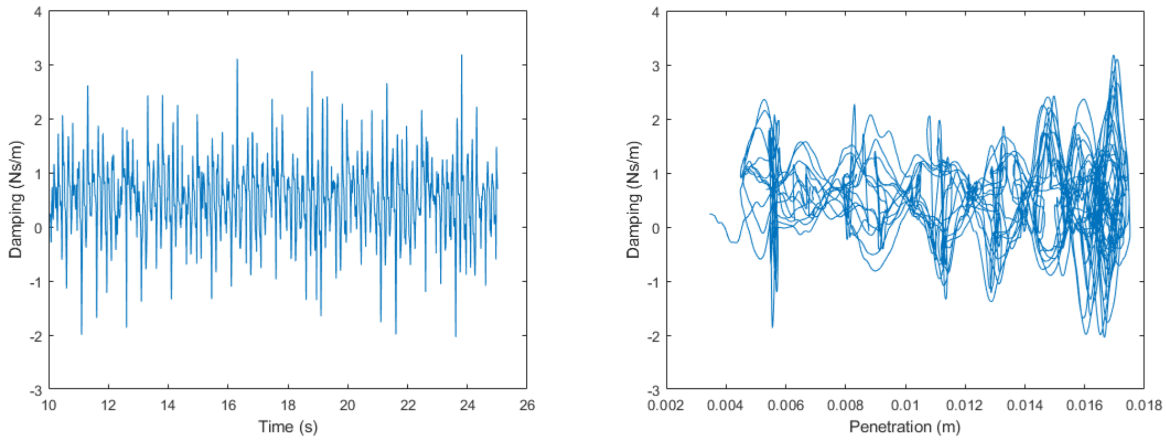

(a) Damping over time.

(b) Damping over penetration.

Figure 3.2.1-6: Damping found from batch LS for the E = 18.96 kPa gel.

The stiffness and damping found from batch LS was for all cycles of the experiment; however, this data must be averaged to create one set of stiffness and damping for one set of penetration and force data. The stiffness and damping data for all modelling cycles was averaged over time, then filtered. The filter used was a moving average filter with a sliding window size of 500 samples. The average stiffness value after filtering was 48.06 N/m and the filtered damping average was 0.54 Ns/m. This stiffness and damping averaged over all cycles and then filtered with the moving average filter is shown in Figure 3.2.1-7 and Figure 3.2.1-8 over the time of one cycle and over the average penetration.

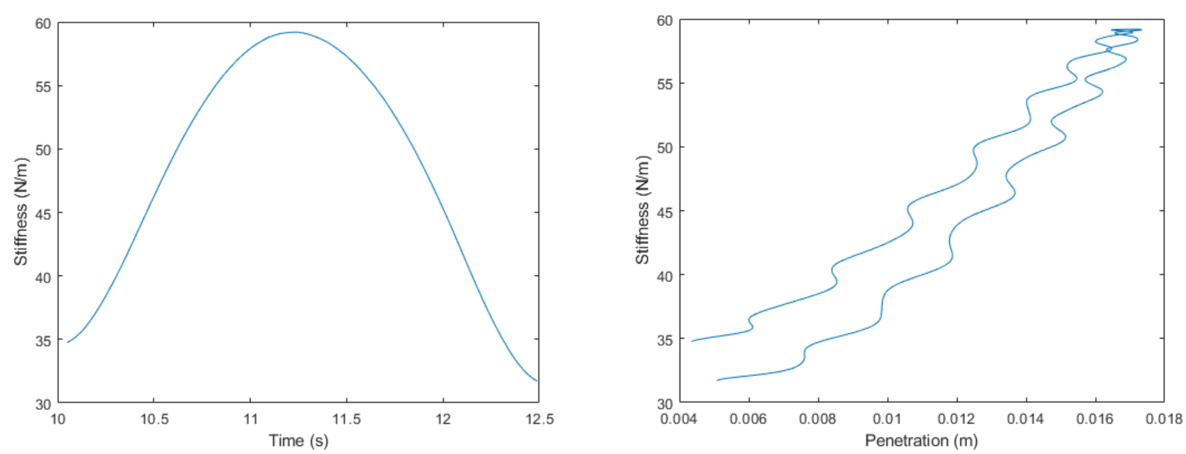

(a) Stiffness over time.

(b) Stiffness over penetration.

Figure 3.2.1-7: Averaged, then moving averaged filtered stiffness for the E = 18.96 kPa gel.

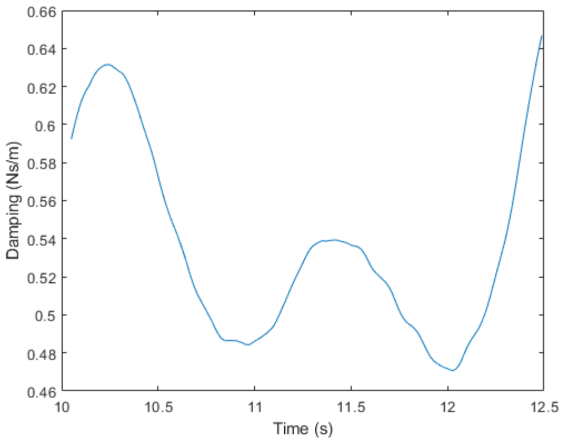

(a) *Damping over time.*

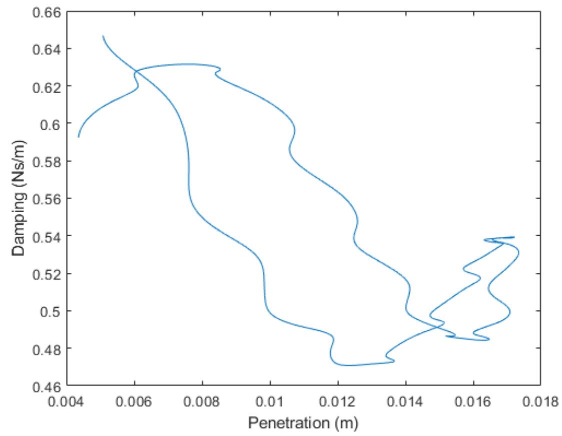

(b) *Damping over penetration.*

Figure 3.2.1-8: Averaged, then moving averaged filtered damping for the E = 18.96 kPa gel.

The penetration and force for a single cycle associated with the stiffness and damping for a single trial is shown in Figure 3.2.1-9 and Figure 3.2.1-10, respectively. These values were found by averaging all of the penetration and force cycles found from experiment.

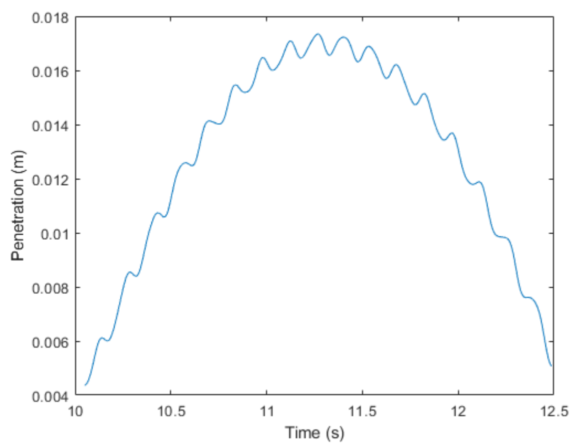

Figure 3.2.1-9: Averaged modelling penetration over time for the E = 18.96 kPa gel.

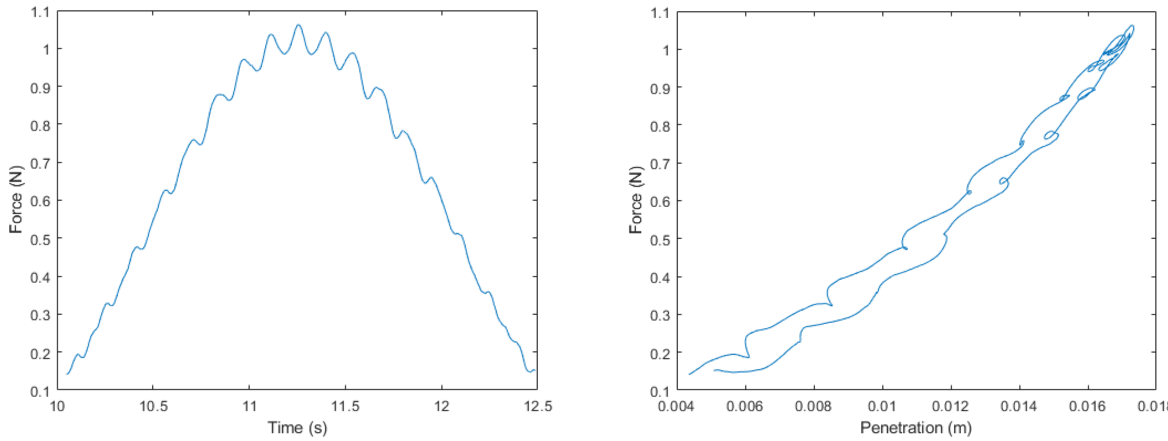

(a) Force over time. *(b) Force over penetration.*

Figure 3.2.1-10: Averaged modelling force for the E = 18.96 kPa gel.

This stiffness and damping data were used with the collected modelling penetration and filtered velocity data to find the calculated modelling force. This is shown compared to the actual collected modelling force with the calculated force contribution of stiffness and damping, shown in Figure 3.2.1-11.

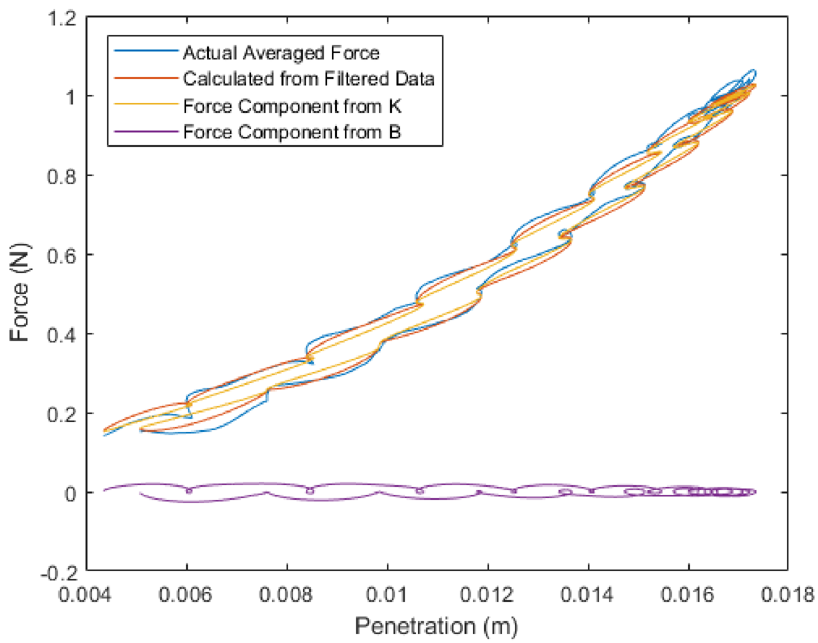

Figure 3.2.1-11: The actual modelling averaged force, the calculated force from stiffness and damping, and the force contribution of the stiffness and damping.

The validation penetration and velocity were used with the stiffness and damping from the batch LS with the modelling data to find calculated validation force. This was compared to the actual validation force, shown in Figure 3.2.1-12, to determine the validity of the stiffness and damping found, and found to have a %RMSE of 7.28% for the E = 18.96 kPa gel, which verifies the stiffness and damping accurately represent the properties of this gel.

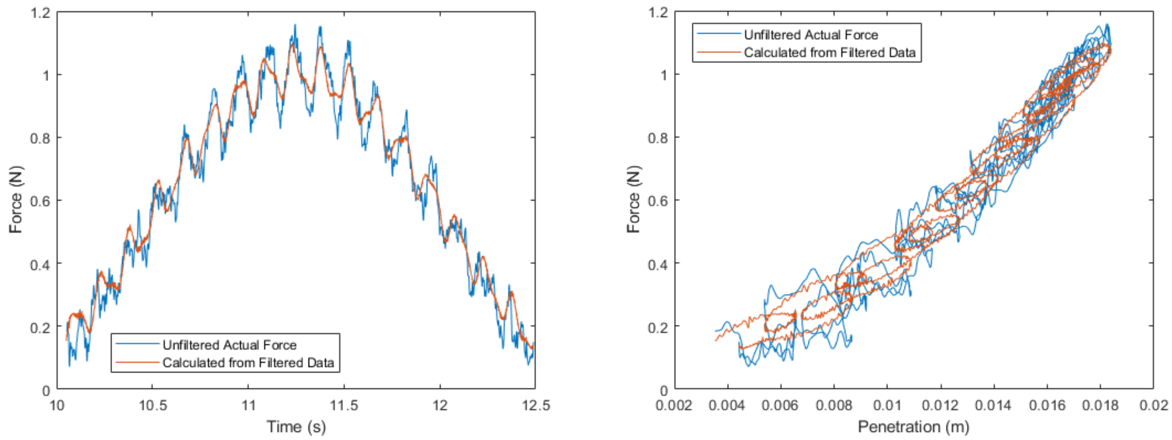

(a) Force over time. *(b) Force over penetration.*

Figure 3.2.1-12: The actual validation averaged force and the calculated force from stiffness and damping.

3.2.2 Experimental Results

This identification process was repeated for each of the gels to find to stiffness and damping of each of the gels for varying penetration. The stiffness and damping results for ach of the gels over penetration are shown in Figure 3.2.2-1. The E = 16.05 kPa gel has the lowest stiffness, followed by the E = 18.96 kPa gel, the E = 55 kPa gel, and finally the E = 132 kPa gel with the highest stiffness, as predicted in Section 3.1.2.

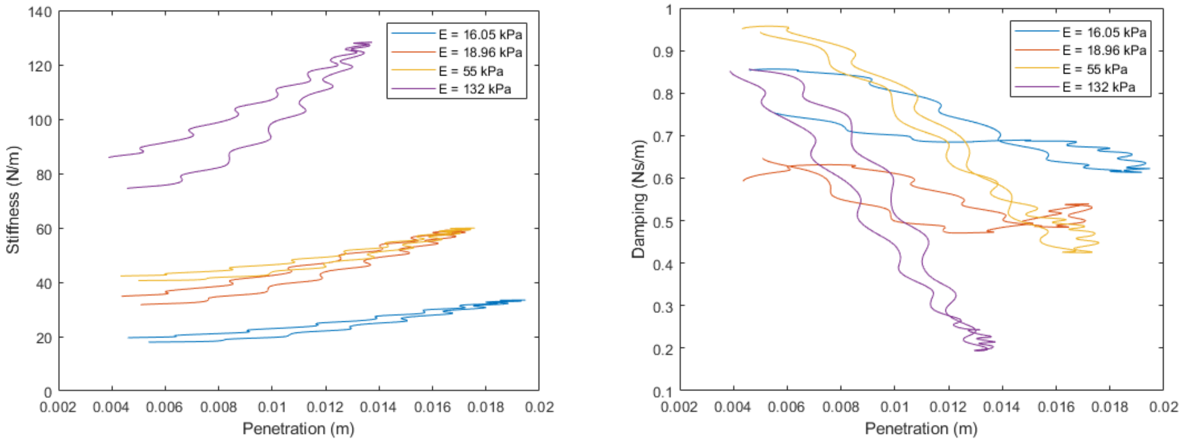

(a) Stiffness data. *(b) Damping data.*

Figure 3.2.2-1: Stiffness and damping results found from identification for each of the gels.

The stiffness and damping results from identification were then used to fit functions. For fitting functions to the data, only the penetration part of the experiment was considered, and not the retraction part. Therefore, the data was split up into penetration and retraction, as shown in Figure 3.2.2-2

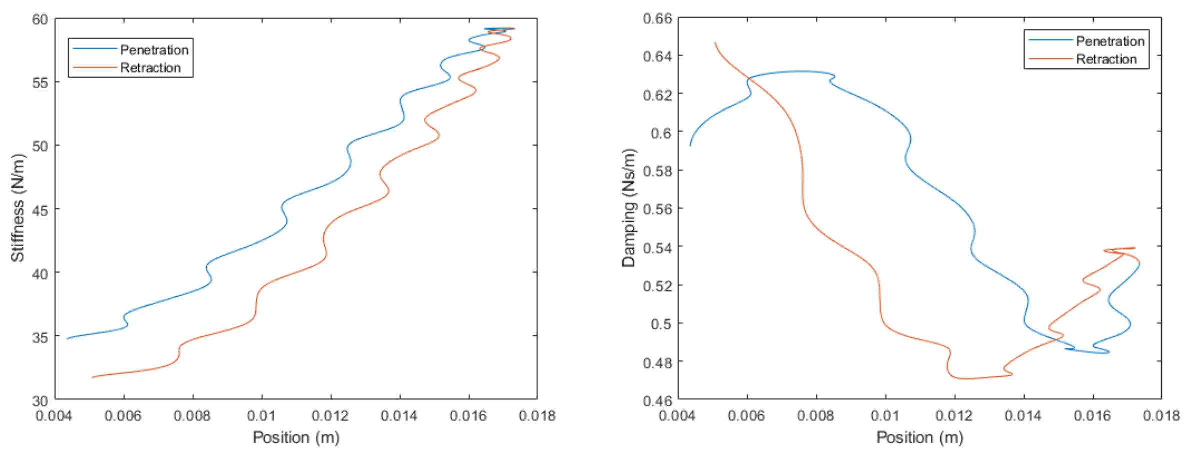

(a) Stiffness data. *(b) Damping data.*

Figure 3.2.2-2: Data split up into penetration and retraction data, shown for the E = 18.96 kPa gel.

The stiffness functions *(3.2.2-1)* and the damping functions *(3.2.2-2)* were fit to the sigmoid function using the MATLAB Curve Fitting tool.

$$K(y) = a_K * \frac{1}{1+e^{-388.6y+b_K}} + c_K; \tag{3.2.2-1}$$

$$B(y) = a_B * \frac{1}{1+e^{(y+b_B)^{c_B}+d_B}}; \tag{3.2.2-2}$$

where y is the penetration in metres and a_K, b_K, c_K, a_B, b_B, c_B, and d_B are constants to be solved for. The stiffness and damping data for each gel, and respective fitted functions, are shown in Figure 3.2.2-3

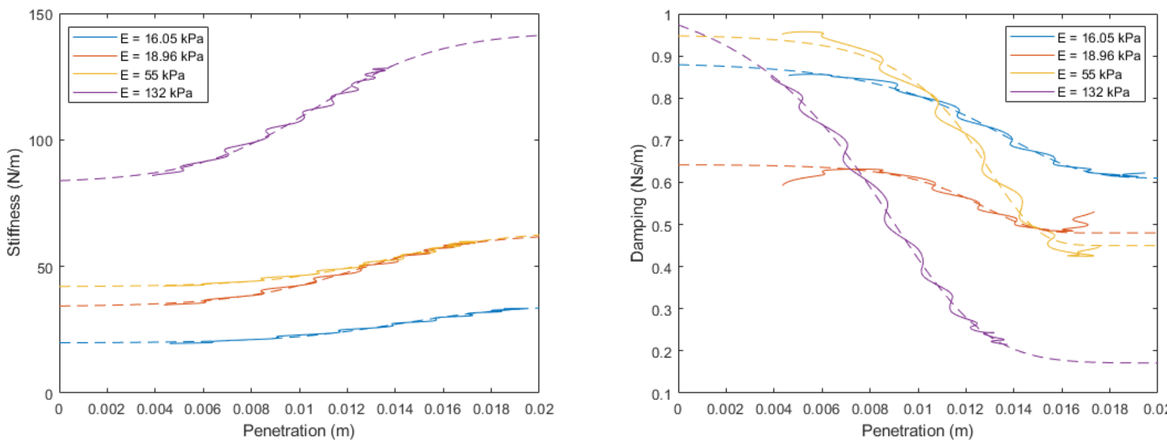

(a) Fitted function for stiffness. *(b) Fitted Function for Damping.*

Figure 3.2.2-3: Stiffness and damping data (solid lines) and fitted functions (dotted lines) for each gel.

The functions fitted to each of these data sets for stiffness and damping are shown in Table 3.2.2-1 and Table 3.2.2-2, respectively, along with the %RMSE of each fit.

Table 3.2.2-1: Fitted function equations for the stiffness data of each gel , and the %RMSE of the fitted function and the actual stiffness.

Young's Modulus	Fitted Function	%RMSE
16.05 kPa	$K(y) = 15.28 * \frac{1}{1+e^{-388.6y+5.521}} + 19.82$	1.57%
18.96 kPa	$K(y) = 28.94 * \frac{1}{1+e^{-388.6y+4.794}} + 34.15$	1.33%
55 kPa	$K(y) = 22.26 * \frac{1}{1+e^{-388.6y+5.362}} + 42$	1.07%
132 kPa	$K(y) = 59.89 * \frac{1}{1+e^{-388.6y+4.169}} + 82.97$	1.15%

Table 3.2.2-2: Fitted function equations for the damping data of each gel , and the %RMSE of the fitted function and the actual damping.

Young's Modulus	Fitted Function	%RMSE
16.05 kPa	$B(y) = 0.61 * \frac{1}{1 + e^{(y+0.9871)^{278.7}+0.9722}}$	0.88%
18.96 kPa	$B(y) = 0.48 * \frac{1}{1 + e^{(y+0.9874)^{457}+1.643}}$	2.95%
55 kPa	$B(y) = 0.45 * \frac{1}{1 + e^{(y+0.9881)^{387.2}}}$	3.0%
132 kPa	$B(y) = 0.1714 * \frac{1}{1 + e^{(y+1)^{126.2}-2.399}}$	3.0%

3.3 Spring-Mass-Damper Mesh

The fitted functions determined in Section 1 represent the stiffness, damping, and therefore force felt at the node of interaction. There is only one stiffness and damping value associated with each value of penetration; therefore, these fitted functions represent a single spring-damper with penetration-varying stiffness and damping values. However, the actual gel is not best represented by a single spring-damper, as each area on the object moves at a different rate and deforming by a different amount. One spring-damper cannot capture this. Therefore, it is beneficial to display and analyze the gel as a network of spring-dampers, so that different areas on the network will move at different rates, and deform by different amounts, just as the physical gel does.

Therefore, in this section we propose a method to map a single spring-damper, which will be referred to as the equivalent spring-damper with equivalent stiffness and damping, to a network of spring-dampers, referred to as the mesh, with the same stiffness and damping value in each link. To do this, there must be an equation equivalating the equivalent stiffness to the stiffness in each link of the mesh, and another equation equivalating the equivalent damping to the damping in each link of the mesh. These equations will be formulated in this section.

3.3.1 Simulation Setup and Equations

The physical gel can be represented in a virtual environment as a 2D spring-mass-damper mesh, as described in Section 1, and shown in Figure 3.3.1-1. The properties of the gel can be represented as stiffness and damping in each link of the mesh, and the mesh nodes can be manipulated just as the surface of the gel can be manipulated. The mesh is a 2-dimensional representation of the gel and represents the center plane of the gel.

The mesh can have any number of links. The section of the mesh that is highlighted green contains the links that directly affect the force opposing the penetration at the point of contact; and therefore, it is the section of the mesh that will be considered when deriving the stiffness and damping mappings.

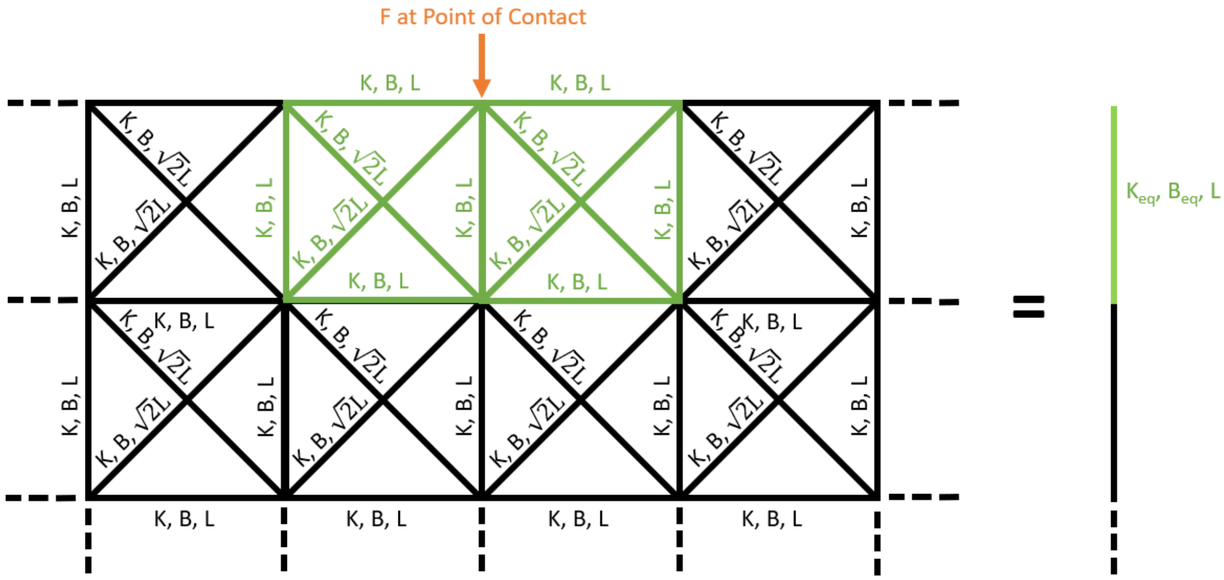

Figure 3.3.1-1: Spring-damper network and equivalent spring-damper.

There needs to be a method to map this equivalent stiffness and damping at the point of contact to the mesh stiffness and damping in each link of the mesh, as shown in Figure 3.3.1-2. This shows how the mesh and equivalent spring-damper are prior to deformation, and how they deformation when deformation is applied at the point of contact. The equivalent spring-damper simply contracts and moves in the direction of deformation. The mesh, however, has some spring-dampers that contract and move in the direction of deformation, where other links expand and move in other directions. This shows how the mesh maps the deformation of the gel much more accurately than the equivalent spring-damper does. This also shows how the mesh and equivalent spring-damper are related by force and penetration, and if they are accurately mapped to each other, the force, penetration, and velocity of penetration at each point of contact will be equal.

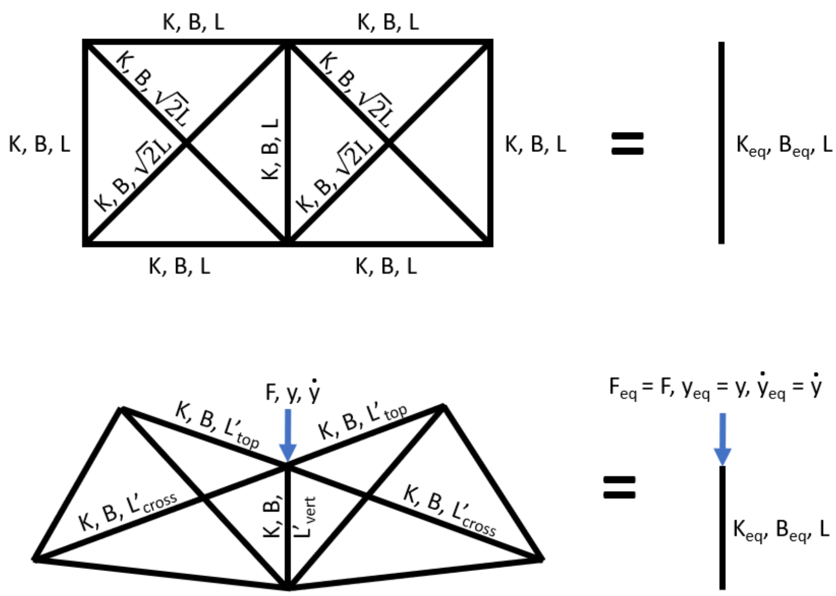

Figure 3.3.1-2: Simple spring-damper network with single equivalent spring-damper.

To achieve this mapping, the spring-dampers create direct reactions at the point of contact are analyzed separately, as shown in Figure 3.3.1-3. Since the forces in the vertical components cancel out, there is only a vertical component to the force, *F*, felt at the point of contact, which can be achieved by determining the force in each of the vertical, top, and cross components for both the stiffness and damping components, according to

$$F_y = F_{y,vert} + 2F_{y,top} + 2F_{y,cross} = F_{eq}. \tag{3.3.1-1}$$

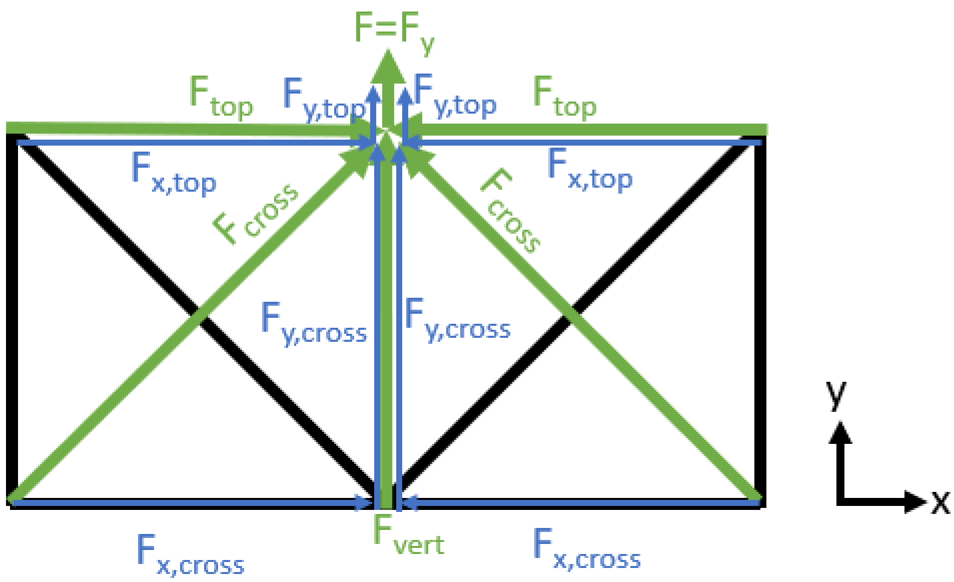

Figure 3.3.1-3: Simple spring-damper network force breakdown.

Each force component is made up of a stiffness and damping component

$$F_y = F_{y,K} + F_{y,B} = K_y \Delta y + B_y \Delta y \tag{3.3.1-2}$$

The parameters used in this formulation are described in Appendix A Table 4.2-1.

3.3.1.1 Stiffness Equation Formulation

In this section, the stiffness breakdown of the vertical, top, and cross spring-dampers is shown, and the force equation for each of these components is formulated. The force equations for each of the components will then be combined, and mapped to the equivalent spring-damper, to create a relationship between the stiffness felt at the point of contact in the mesh, and that of the equivalent spring-damper.

Vertical Spring: The vertical spring breakdown is shown in Figure 3.3.1.1-1.

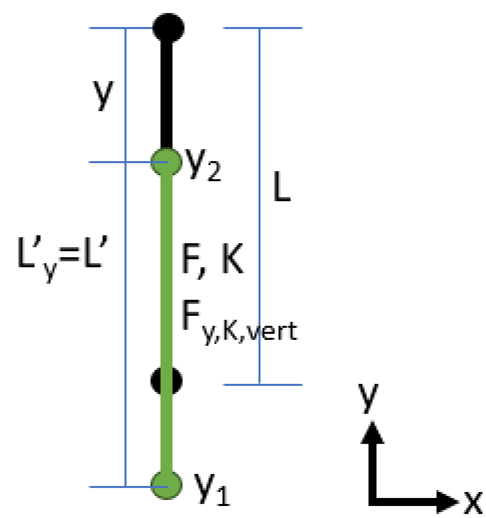

Figure 3.3.1.1-1: Vertical spring breakdown.

The mapping of the equivalent spring to the vertical spring is

$$F_{y,K,vert} = F = K(L - L') = K(L - (y_2 - y_1)) \qquad (3.3.1.1\text{-}1)$$

Top Springs: The breakdown of the two top springs is shown in Figure 3.3.1.1-2.

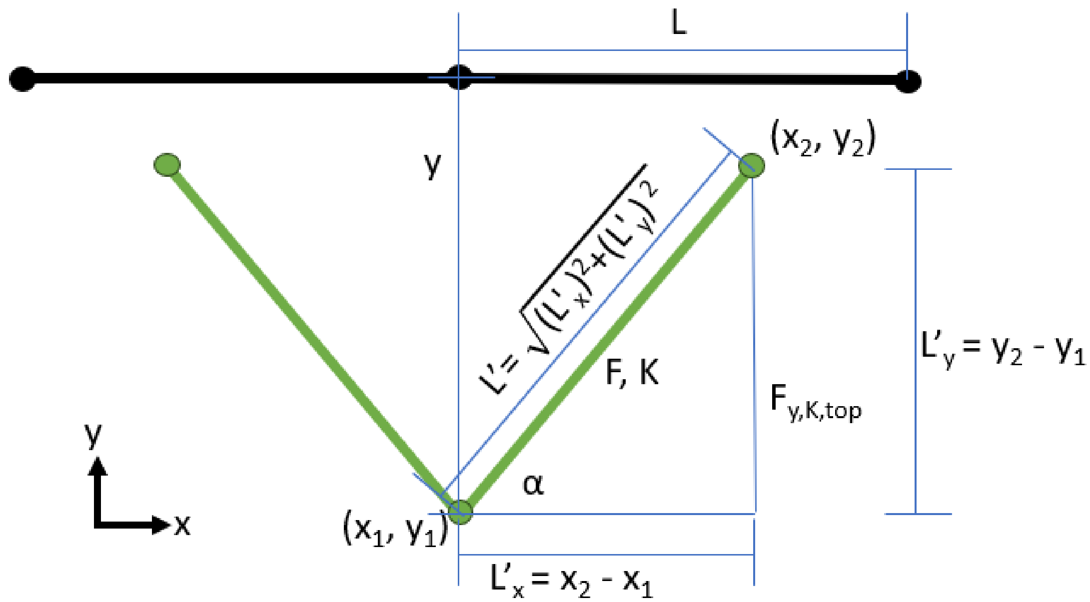

Figure 3.3.1.1-2: Breakdown of the two top springs.

The mapping of the equivalent spring to the one of the two top springs is

$$F_{y,K,top} = Fsin\alpha = K(L' - L)sin\alpha = K\left(\sqrt{(L'_x)^2 + \left(L'_y\right)^2} - L\right)sin\alpha =$$

$$K\left(\sqrt{(L'_x)^2 + \left(L'_y\right)^2} - L\right)\frac{L'_y}{L'} = \frac{K\left(\sqrt{\left(L'_x\right)^2+\left(L'_y\right)^2}-L\right)}{\sqrt{\left(L'_x\right)^2+\left(L'_y\right)^2}}(y_2 - y_1) \tag{3.3.1.1-2}$$

<u>Cross Springs:</u> The breakdown of the two cross springs is shown in Figure 3.3.1.1-3.

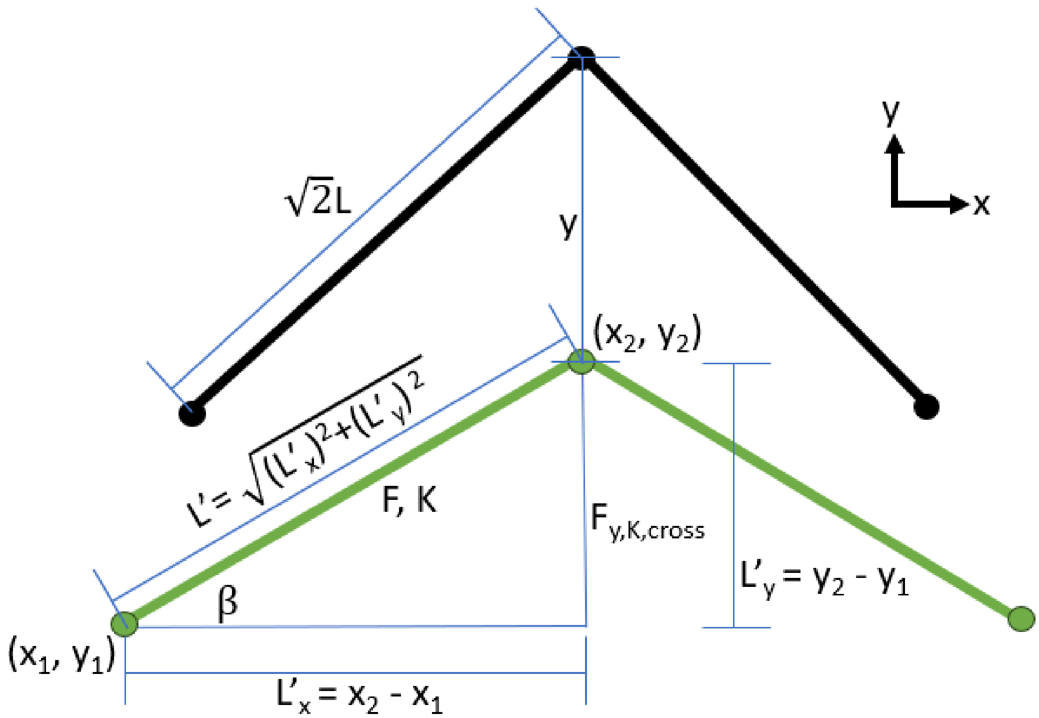

Figure 3.3.1.1-3: Breakdown of the two cross springs.

The mapping of the equivalent spring to one of the two cross springs is

$$F_{y,K,cross} = Fsin\alpha = K\left(\sqrt{2}L - L'\right)sin\beta = K\left(\sqrt{2}L - \sqrt{(L'_x)^2 + \left(L'_y\right)^2}\right)sin\beta =$$

$$K\left(\sqrt{2}L - \sqrt{(L'_x)^2 + \left(L'_y\right)^2}\right)\frac{L'_y}{L'} = \frac{KL'_y(\sqrt{2}L-\sqrt{\left(L'_x\right)^2+\left(L'_y\right)^2})}{\sqrt{\left(L'_x\right)^2+\left(L'_y\right)^2}} \tag{3.3.1.1-3}$$

Overall Stiffness Equation: These individual mappings are combined to provide the mapping for the equivalent spring at the point of contact to the stiffness in each spring in the mesh and vise versa.

$$F_{y,K} = F_{y,K,vert} + 2F_{y,K,top} + 2F_{y,K,cross} \tag{3.3.1.1-4}$$

$$K_{eq}y_{eq} = K(L-(y_2-y_1)_{vert}) + 2\frac{K\left(\sqrt{\left(L'_{x,top}\right)^2+\left(L'_{y,top}\right)^2}-L\right)}{\sqrt{\left(L'_{x,top}\right)^2+\left(L'_{y,top}\right)^2}}(y_2-y_1)_{top} + 2\frac{KL'_{y,cross}\,(\sqrt{2}L-\sqrt{\left(L'_{x,cross}\right)^2+\left(L'_{y,cross}\right)^2})}{\sqrt{\left(L'_{x,cross}\right)^2+\left(L'_{y,cross}\right)^2}} \tag{3.3.1.1-5}$$

$$K_{eq} = \frac{K(L-(y_2-y_1)_{vert})+2\frac{K\left(\sqrt{\left(L'_{x,top}\right)^2+\left(L'_{y,top}\right)^2}-L\right)}{\sqrt{\left(L'_{x,top}\right)^2+\left(L'_{y,top}\right)^2}}(y_2-y_1)+2\frac{KL'_{y,cross}(\sqrt{2}L-\sqrt{\left(L'_{x,cross}\right)^2+\left(L'_{y,cross}\right)^2})}{\sqrt{\left(L'_{x,cross}\right)^2+\left(L'_{y,cross}\right)^2}}}{yeq}$$

$$K = \frac{K_{eq}yeq}{(L-(y_2-y_1)_{vert})+2\frac{\left(\sqrt{\left(L'_{x,top}\right)^2+\left(L'_{y,top}\right)^2}-L\right)}{\sqrt{\left(L'_{x,top}\right)^2+\left(L'_{y,top}\right)^2}}(y_2-y_1)+2\frac{KL'_{y,cross}(\sqrt{2}L-\sqrt{\left(L'_{x,cross}\right)^2+\left(L'_{y,cross}\right)^2})}{\sqrt{\left(L'_{x,cross}\right)^2+\left(L'_{y,cross}\right)^2}}} \tag{3.3.1.1-6}$$

3.3.1.2 Damping Equation Formulation

In this section, the damping breakdown of the vertical, top, and cross spring-dampers is shown, and the force equation for each of these components is formulated. The force equations for each of the components will then be combined, and mapped to the equivalent spring-damper, to create a relationship between the damping felt at the point of contact in the mesh, and that of the equivalent spring-damper.

This process was then repeated to determine the mapping for the damping felt at the point of contact to the damping in each damper in the mesh.

Vertical Spring: The vertical damping breakdown is shown in Figure 3.3.1.2-1.

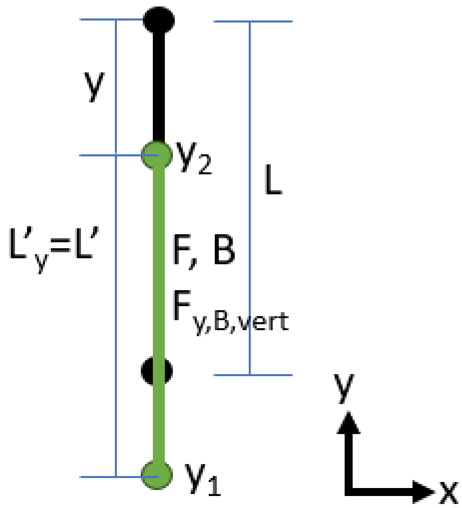

Figure 3.3.1.2-1: Vertical damper breakdown.

The mapping of the equivalent damper to the vertical dampers is

$$F_{y,B,vert} = F = B(L \dot{-} L') = B\,\frac{(L-L\prime)-(L-L')_{prev}}{\Delta t} \tag{3.3.1.2-1}$$

Top Dampers: The breakdown of the two top dampers is shown in Figure 3.3.1.2-2.

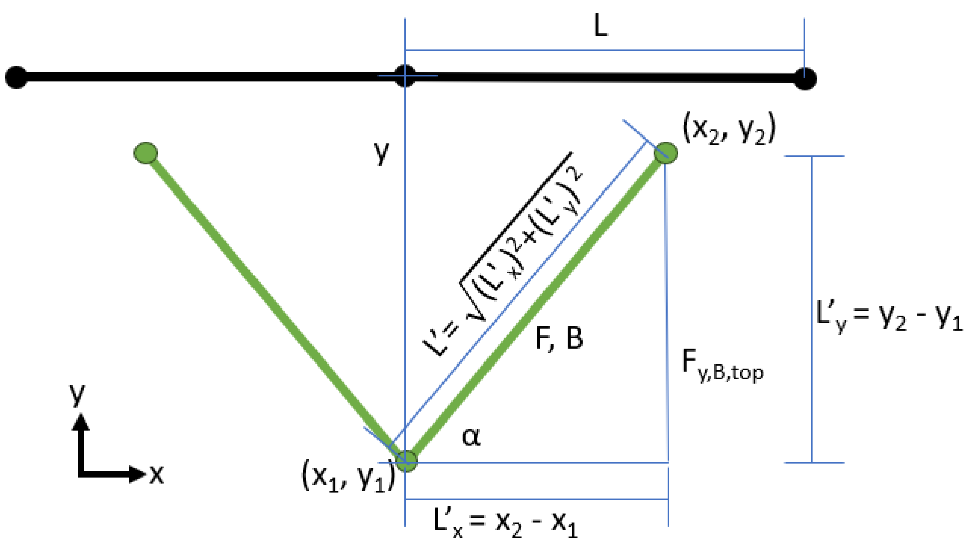

Figure 3.3.1.2-2: Breakdown of the two top dampers.

The mapping of the equivalent damper to one of the two top dampers is

$$F_{y,B,top} = Fsin\alpha = B(L' \dot{-} L)sin\alpha = B\frac{(L'-L)-(L'_{prev}-L)}{\Delta t}sin\alpha =$$
$$B\frac{(L'-L)-(L'_{prev}-L)}{\Delta t}\frac{L'_y}{L'} = B\frac{(L'-L)-(L'_{prev}-L)}{\Delta t}\frac{L'_y}{\sqrt{(L'_x)^2+(L'_y)^2}} = \tag{3.3.1.2-2}$$
$$\frac{BL'_y}{\sqrt{(L'_x)^2+(L'_y)^2}}\frac{\left(\sqrt{(L'_x)^2+(L'_y)^2}-L\right)-\left(\sqrt{(L'_{x,prev})^2+(L'_{y,prev})^2}-L\right)}{\Delta t}$$

Cross Dampers: The breakdown of the two cross dampers is shown in Figure 3.3.1.1-3.

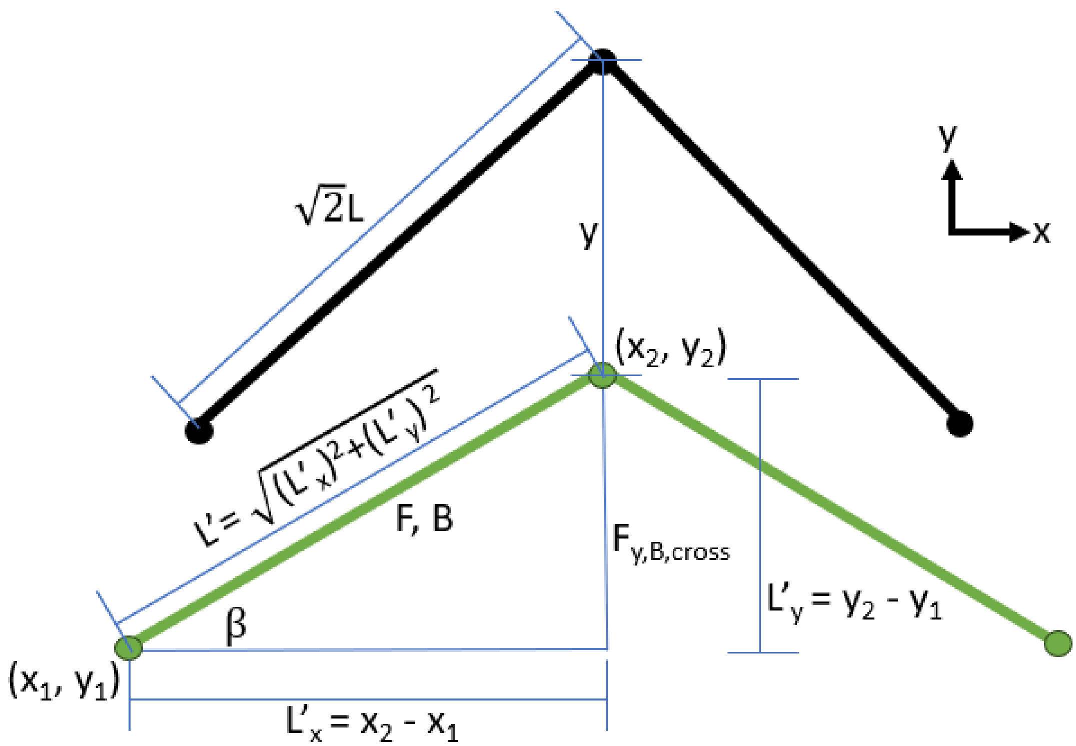

Figure 3.3.1.2-3: Breakdown of the two cross dampers.

The mapping of the equivalent damper to one of the two cross dampers is

$$F_{y,B,cross} = Fsin\beta = B(\sqrt{2}\dot{L} - L')sin\beta = B\,\frac{(\sqrt{2}L-L')-(\sqrt{2}L-L'_{prev})}{\Delta t}\,sin\beta =$$
$$B\,\frac{(\sqrt{2}L-L')-(\sqrt{2}L-L'_{prev})}{\Delta t}\,\frac{L'_y}{L'} = B\,\frac{(\sqrt{2}L-L')-(\sqrt{2}L-L'_{prev})}{\Delta t}\,\frac{L'_y}{\sqrt{(L'_x)^2+(L'_y)^2}} =$$
$$\frac{BL'_y}{\sqrt{(L'_x)^2+(L'_y)^2}}\,\frac{\left(\sqrt{2}L-\sqrt{(L'_x)^2+(L'_y)^2}\right)-\left(\sqrt{2}L-\sqrt{(L'_{x,prev})^2+(L'_{y,prev})^2}\right)}{\Delta t} \tag{3.3.1.2-3}$$

<u>Overall Damping Equation:</u> These individual mappings are combined to provide the mapping for the equivalent damper at the point of contact to the damping in each damper in the mesh and vise versa.

$$F_{y,B} = F_{y,B,vert} + 2F_{y,B,top} + 2F_{y,B,cross} \tag{3.3.1.2-4}$$

$$B_{eq}\dot{y}_{eq} = B\,\frac{(L-L'_{vert})-(L-L'_{vert})_{prev}}{\Delta t} +$$
$$2\,\frac{BL'_{y,top}}{\sqrt{(L'_{x,top})^2+(L'_{y,top})^2}}\,\frac{\left(\sqrt{(L'_{x,top})^2+(L'_{y,top})^2}-L\right)-\left(\sqrt{(L'_{x,prev,top})^2+(L'_{y,prev,top})^2}-L\right)}{\Delta t} +$$
$$2\,\frac{BL'_{y,cross}\left(\sqrt{2}L-\sqrt{(L'_{x,cross})^2+(L'_{y,cross})^2}\right)-\left(\sqrt{2}L-\sqrt{(L'_{x,prev,cross})^2+(L'_{y,prev,cross})^2}\right)}{\sqrt{(L'_{x,cross})^2+(L'_{y,cross})^2}\,\Delta t}$$

$$B_{eq} = \left(B\,\frac{(L-L')-(L-L')_{prev}}{\Delta t} + 2B\,\frac{L'_y\left(\sqrt{(L'_x)^2+(L'_y)^2}-L\right)-\left(\sqrt{(L'_{x,prev})^2+(L'_{y,prev})^2}-L\right)}{\sqrt{(L'_x)^2+(L'_y)^2}\,\Delta t} + \right.$$
$$\left. 2B\,\frac{L'_y\left(\sqrt{2}L-\sqrt{(L'_x)^2+(L'_y)^2}\right)-\left(\sqrt{2}L-\sqrt{(L'_{x,prev})^2+(L'_{y,prev})^2}\right)}{\sqrt{(L'_x)^2+(L'_y)^2}\,\Delta t}\right)/\dot{y}_{eq} \tag{3.3.1.2-5}$$

$$B = B_{eq}\dot{y_{eq}} / \left(B\frac{(L-L'_{vert})-(L-L'_{vert})_{prev}}{\Delta t} + \right.$$

$$2\frac{BL'_{y,top}\left(\sqrt{\left(L'_{x,top}\right)^2+\left(L'_{y,top}\right)^2}-L\right)-\left(\sqrt{\left(L'_{x,prev,top}\right)^2+\left(L'_{y,prev,top}\right)^2}-L\right)}{\sqrt{\left(L'_{x,top}\right)^2+\left(L'_{y,top}\right)^2}\Delta t} +$$

$$\left. 2\frac{BL'_{y,cross}\left(\sqrt{2}L-\sqrt{\left(L'_{x,cross}\right)^2+\left(L'_{y,cross}\right)^2}\right)-\left(\sqrt{2}L-\sqrt{\left(L'_{x,prev,cross}\right)^2+\left(L'_{y,prev,cross}\right)^2}\right)}{\sqrt{\left(L'_{x,cross}\right)^2+\left(L'_{y,cross}\right)^2}\Delta t} \right) \quad (3.3.1.2\text{-}6)$$

3.3.1.3 Spring-Damper VE Implementation

The spring-damper mesh was then implemented as a virtual environment, as shown in Figure 3.3.1.3-1. The base for this code was from [45] and modified for our purposes. The VE receives the contact position "*y*" and the contact equivalent stiffness "K_{eq}" and damping "B_{eq}" as a function of contact position as input and outputs the contact force "*F*". The Mesh Simulation block receives the contact position, and the mesh link damping and stiffness to generate *F*. In this process the block also generates the position of the mesh nodes. The node positions, the contact position, the equivalent stiffness and damping as well as the contact velocity obtained form BD method are fed to the mapping blocks "K_{eq} to K" and "B_{eq} to B" to generate the link stiffness and damping needed for Mech Simulation block. To implement the virtual version of the four gels, the values of $K_{eq}(y)$ and $B_{eq}(y)$ functions were derived from the physical experiments with the gel as reported in Section 1.

Our simulation in Figure 3.3.1.3-1 not only implements the damper-spring VE, it also validates it with equivalent model, by passing the output force of the Mesh Simulation block through the contact equivalent model to find the equivalent contact position. The contact position y and the equivalent contact position are then compared for validation of the Mesh Simulation.

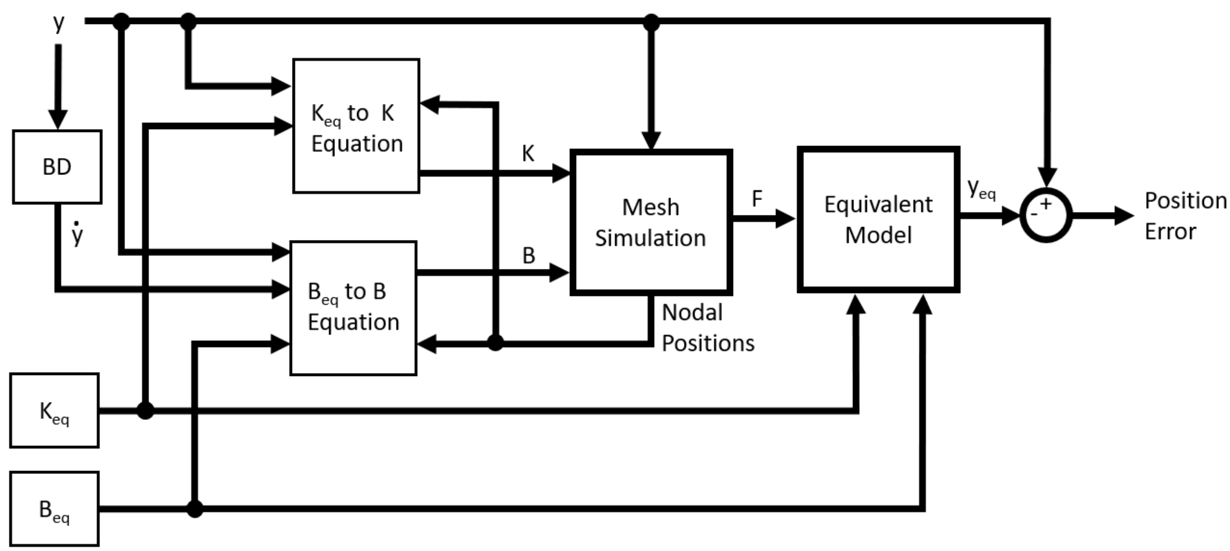

Figure 3.3.1.3-1: Block diagram for the spring-mass-damper mesh simulation.

For accuracy, the mass of the gel was included in the simulation, as

$$m_{node} = \frac{m_{gel}}{\#_{nodes}} \tag{3.3.1.3-1}$$

where the mass of the gel, in kg, was measured from each physical gel, the number of nodes was 25 for this simulation, and the mass of each node, in kg, was set in the simulation code.

3.3.2 Simulation Results and Analysis

3.3.2.1 Mesh Implementation Results in the Simulation

The mesh, Figure 3.3.2.1-1, can be analyzed by using the stiffness and damping functions fitted from the stiffness and damping found for the physical gel from the batch least squares identification. The *y(t)* array can be replaced with the position data from the physical gel experiment so that the physical experimental force and the force at the manipulated node of the mesh can be compared. This analysis that will be described in the section is summarized in Figure 3.4.1-1.

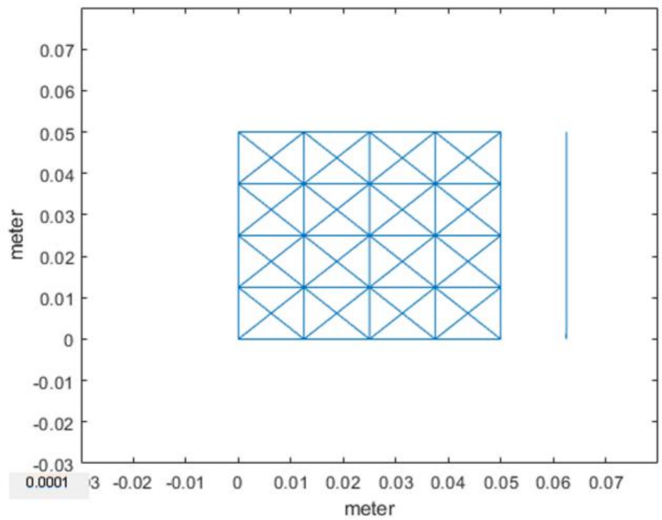

Figure 3.3.2.1-1: The graphics for the mesh (left) and equivalent spring-mass-damper (right). The manipulated node of the mesh is the top center node, and the manipulated node of the equivalent is the top node.

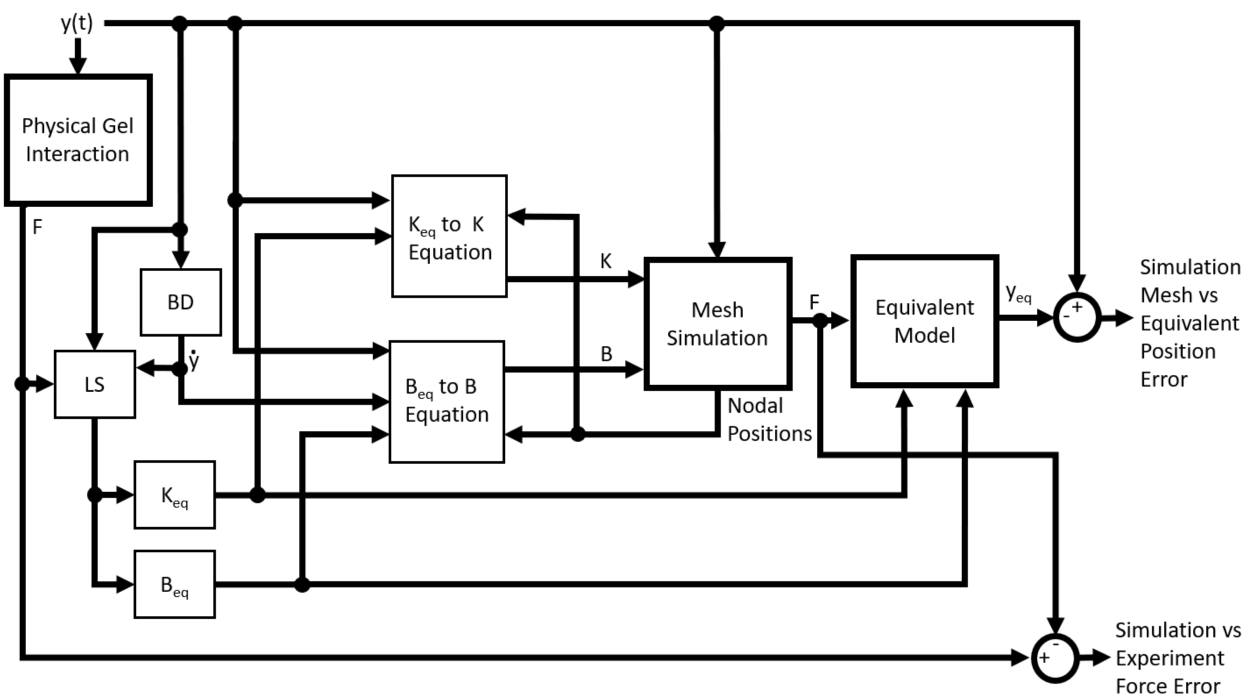

Figure 3.3.2.1-2: Block diagram showing the relationship between the physical gel experiments and the spring-mass-damper mesh simulation.

The mesh stiffness and damping for each spring-mass-damper in the mesh over time for a specific gel is shown in Figure 3.3.2.1-3, found from equation

(3.3.1.1-6) and Figure 3.3.2.1-3b, found from equation *(3.3.1.2-6)*, respectively.

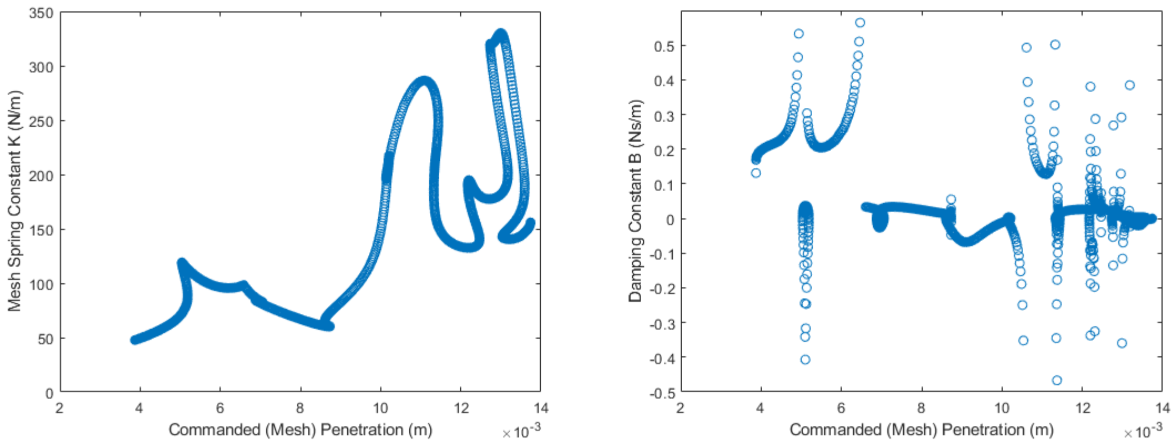

(a) Mesh stiffness. *(b) Mesh damping.*

Figure 3.3.2.1-3: Mesh stiffness and damping for each spring-mass-damper in the mesh.

The penetration comparison between the manipulated mesh node and the equivalent spring-mass-damper is shown in Figure 3.3.2.1-4a, as mentioned in Figure 3.3.2.1-2. The position error is shown in Figure 3.3.2.1-4b, with an average error of 3.79x10^{-7} mm, verifying that equation (*3.3.1.1-6*) and equation (*3.3.1.2-6*) correctly map the equivalent stiffness and damping to that of the mesh.

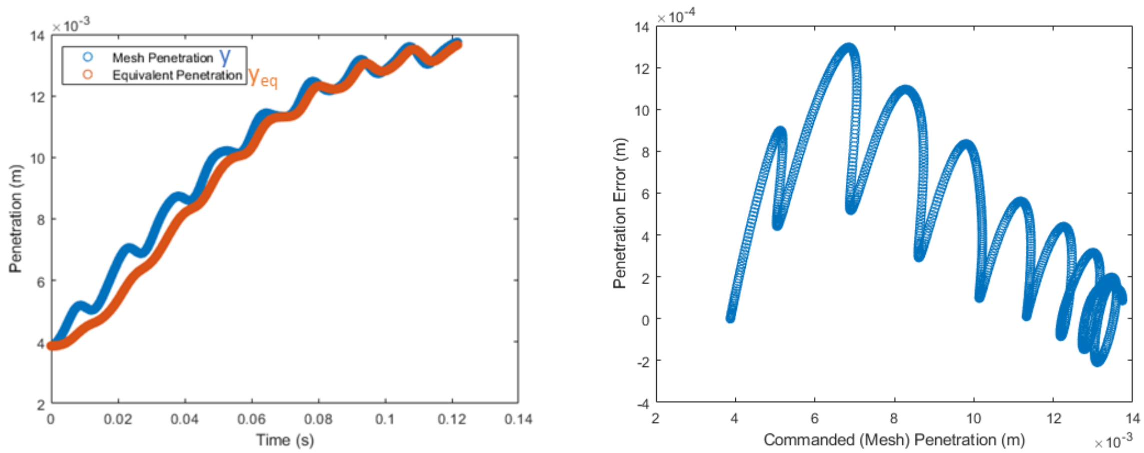

(a) The penetration at the manipulated nodes. *(b) The penetration error between the nodes.*

Figure 3.3.2.1-4: The penetration at the manipulated mesh node compared to that of the equivalent and the error between these two penetrations.

The actual force from experiment is compared to the simulated force and shown in Figure 3.3.2.1-5, as mentioned in Figure 3.3.2.1-2, with a %RMSE of 2.08%, verifying that the mesh simulation correctly follows the physical response.

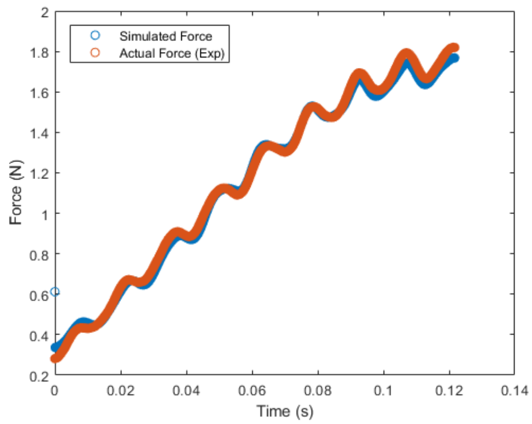

Figure 3.3.2.1-5: The simulated force, which is the same for the mesh and equivalent, compared to the actual force from the physical experiment.

3.3.2.2 Mesh Simulation Results Comparison

The point of contact in the mesh simulation clearly follows the equivalent spring-damper and the physical interaction at the point of contact. However, we can also determine if each point in the spring-mass-damper network in the mesh simulation follows each point in the physical experiment, as well as a 3D FEM model. The FEM model is included in this comparison to provide a third view of the gel deformation. The FEM model only includes stiffness; therefore, for this purpose, only stiffness will be included in the simulation. The gel deformation, Figure 3.3.2.2-1, is shown for the top "plane" of the gel, as all "planes" deformed by the same amount, so the top "plane" is an accurate representation of all "planes". The FEM deformation, Figure 3.3.2.2-2, has three planes, as is a five by five by three nodal model, making each of the face planes the same as the simulation mesh, which is a five by five nodal model. The FEM was deformed by a thin prodding device matching that from the physical experiments and interacting with the gel in the same way. The simulation mesh deformation is shown in Figure 3.3.2.2-3. All three deformations had the same penetration and velocity of interaction applied. The mesh and FEM nodal locations after deformation are accurate, as they were calculated by the software. However, the physical gel nodal locations were manually determined by measuring the changes in nodal location and are not as accurate. However, this analysis is meant to provide a general idea of how the nodal points after deformation match. From this comparison, it is clear that the nodes do match each other in each of the models, as the nodal locations of each node are very similar.

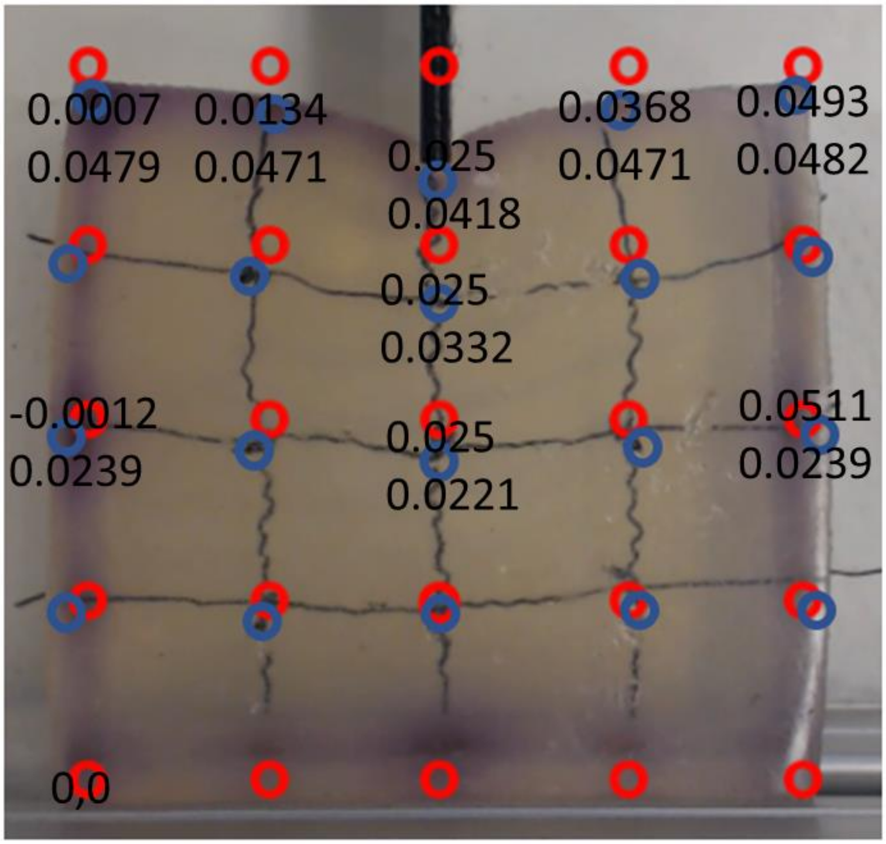

Figure 3.3.2.2-1: Nodal locations, in metres, after deformation for the physical gel. The initial nodal locations are shown in red, and the nodal locations after deformation are shown in blue. The coordinates are given as the horizontal then vertical location.

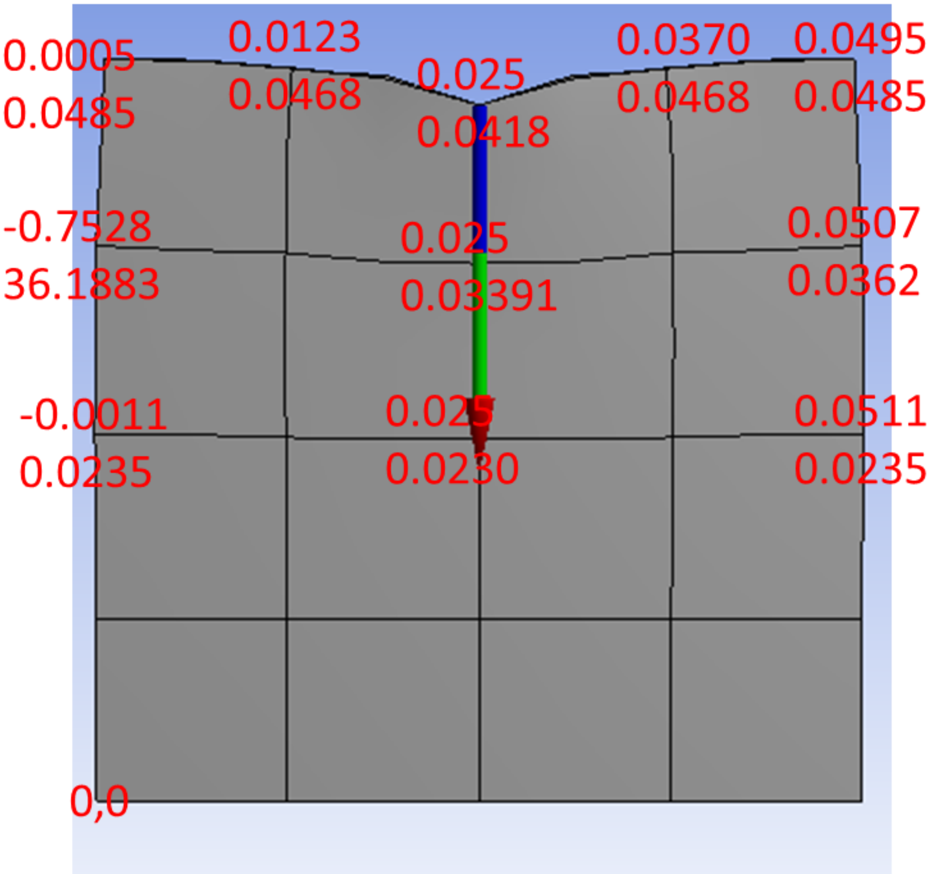

Figure 3.3.2.2-2: Nodal locations, in metres, after deformation for the FEM gel model. This is the middle plane of the 3D FEM model. The coordinates are given as the horizontal then vertical location.

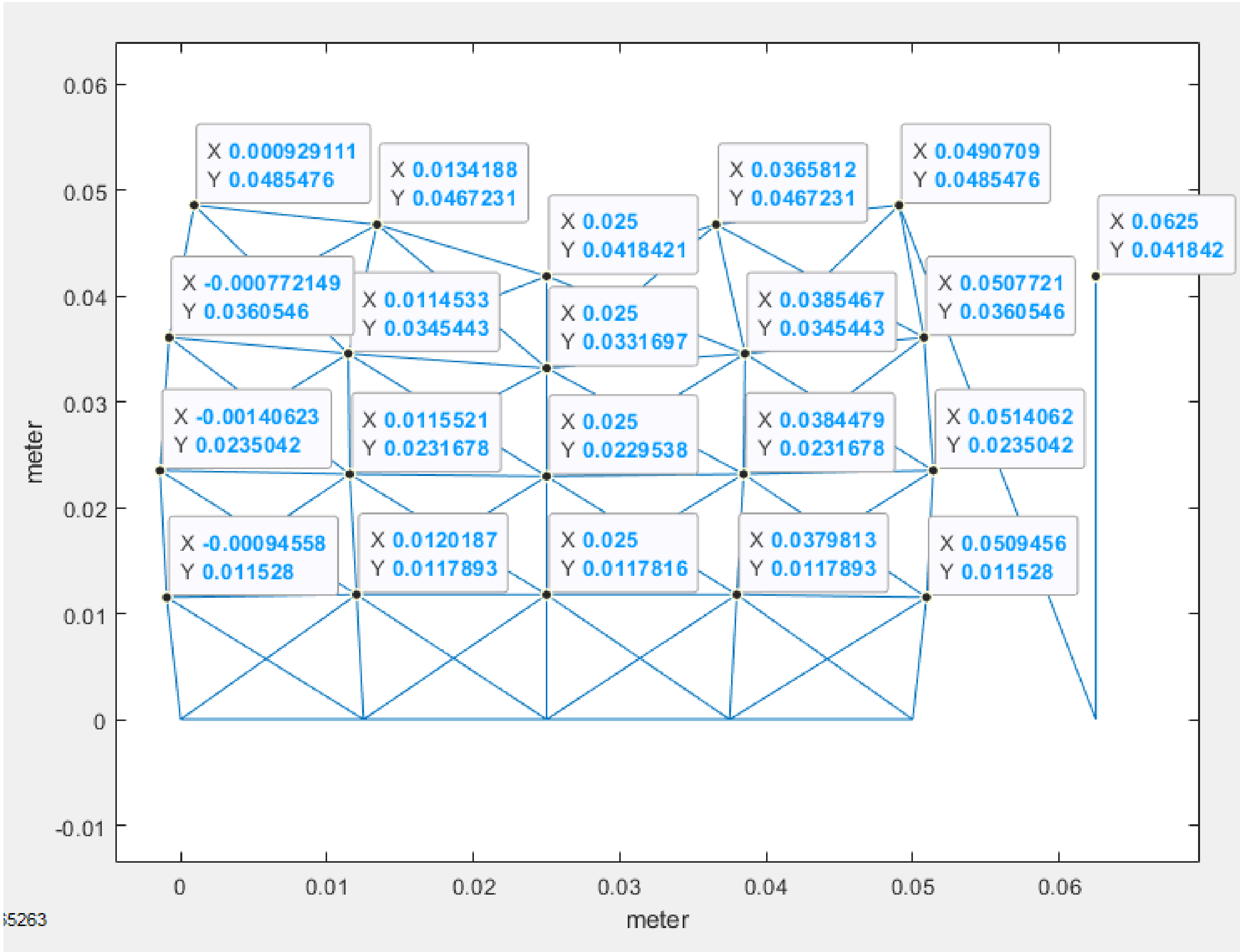

Figure 3.3.2.2-3: Nodal locations, in metres, after deformation for the mesh spring-mass-damper network. The equivalent spring-damper is also shown on the right of the mesh. The coordinates are given as the horizontal then vertical location.

3.4 Haptic Simulation System Implementation

3.4.1 Haptic Simulation System

The mesh is implemented as a virtual environment with the Pantograph to create an uncoupled haptic simulation system for uncoupled stability experiments, as shown in Figure 3.4.1-1. An initial penetration is provided only at the beginning of the simulation. This position is fed into the Pantograph, which provides its current position to the VE. The VE consists of the fitted and interpolated functions for stiffness and damping, and the Pantograph position which are provided to the mesh simulation block from Figure 3.3.2.1-2 in place of the *y(t)* array. The VE is implemented bidirectionally, meaning that when the prodding device exited the virtual gel, the gel environment is mirrored so that the same environment would be felt regardless of the direction penetration. The computer force of the VE is then fed to the Pantograph.

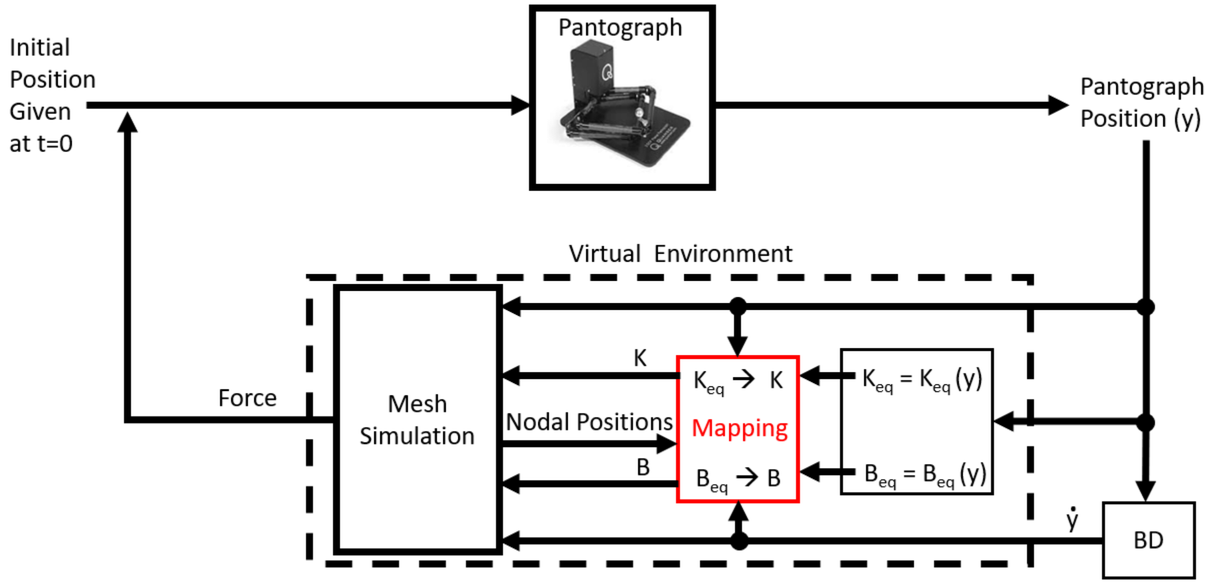

Figure 3.4.1-1: Block diagram for the VE implemented on the Pantograph.

3.4.2 Interpolated Dynamic Properties

To run the uncoupled stability experiments, we had four fitted virtual environment models of four gels. The stiffness and damping of these models are penetration dependent. In order to develop a stiffness versus damping chart, we considered the stiffness and damping of the point of contact as a point of the chart. To generate the other points of the chart, representing the stiffness and damping at the point of contact for other deformable environments, we interpolated and extrapolated the models we had for the four gels.

Figure 3.4.2-1 and Figure 3.4.2-2 show the four fitted stiffness and damping functions (solid lines) and the interpolated/extrapolated functions (dashed lines). The stiffness functions for the additional interpolated damping were chosen to provide more evenly spaced damping functions within the limits of the existing functions, as well as to add additional functions to test outside of the physical gel range. The stiffness functions for the additional interpolated stiffness functions were chosen during the stability experiments to determine the limits of stability of stiffness for each damping function, as described in Section 3.5.

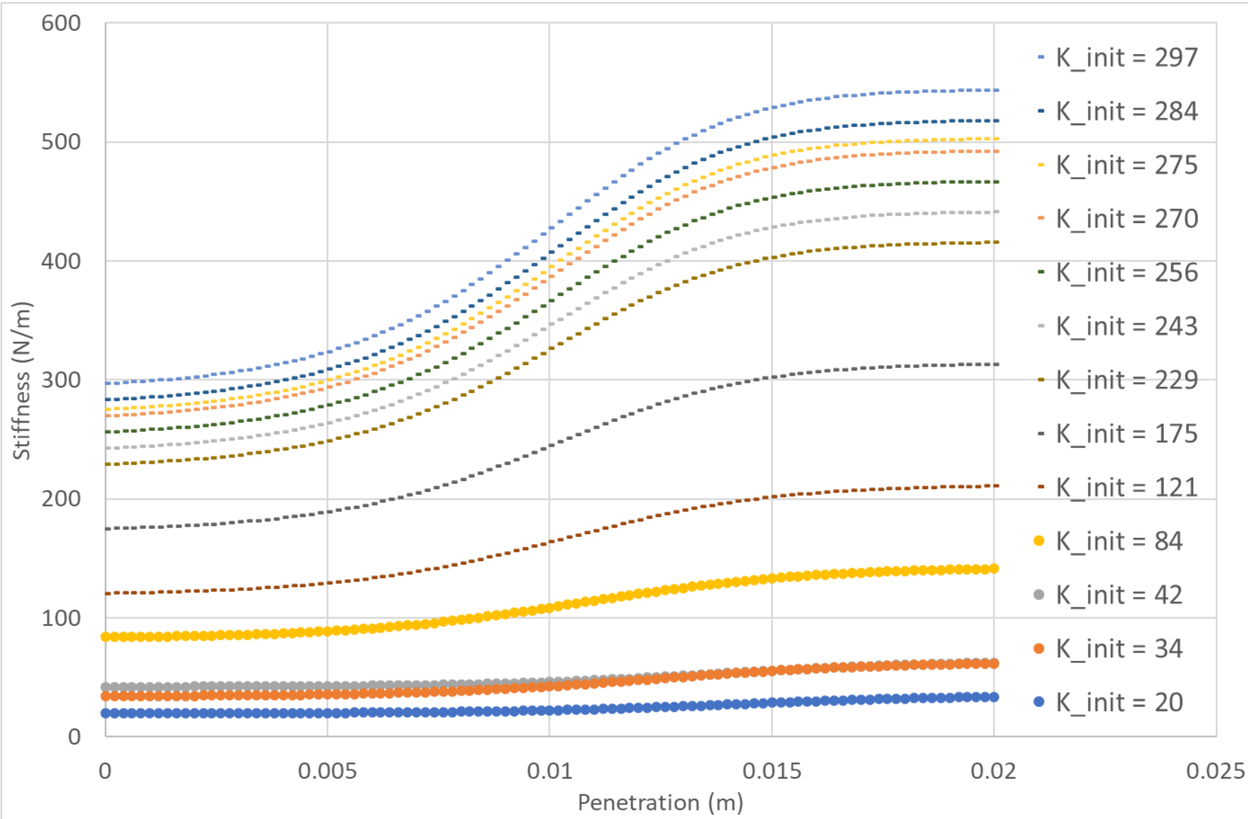

Figure 3.4.2-1: Identified and extrapolated, and interpolated stiffness for varying Young's Modulus values over penetration. The extrapolated parts and identified functions are represented by solid dots. The interpolated functions are represented by dashed lines.

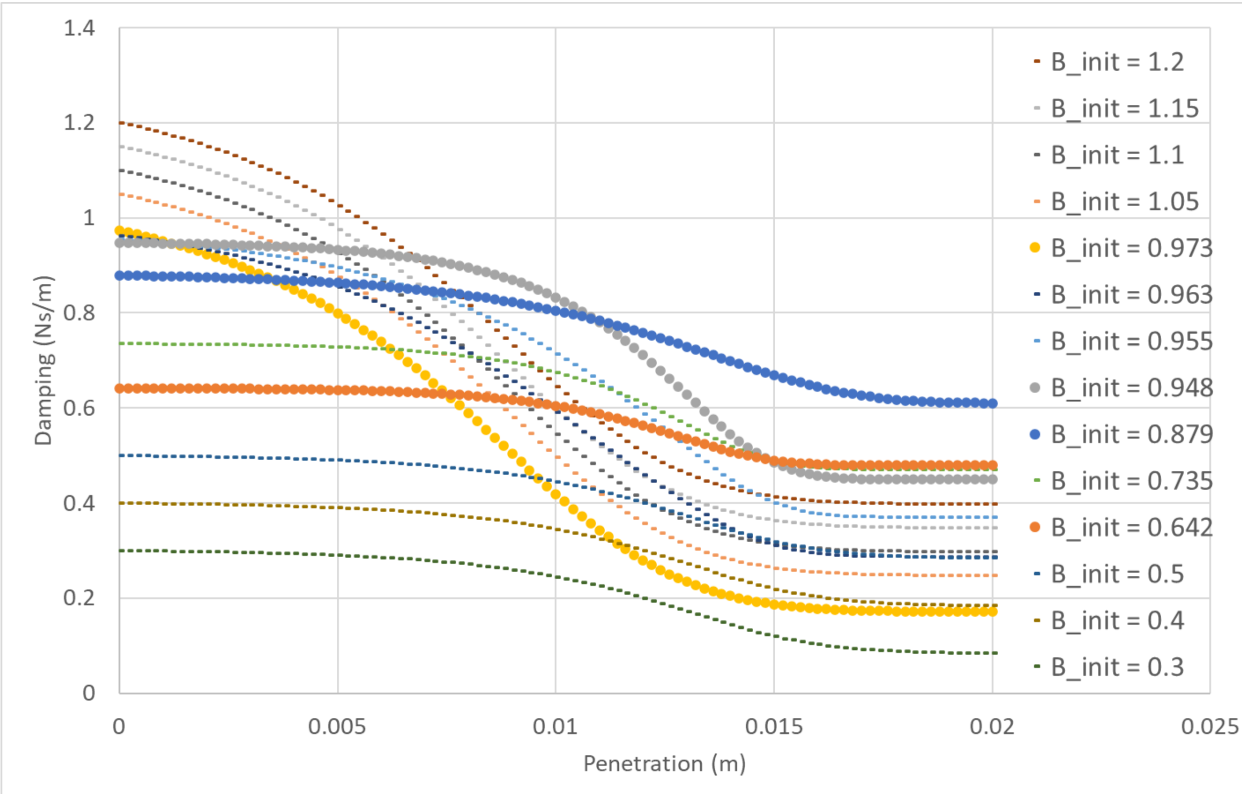

Figure 3.4.2-2: Identified and extrapolated, and interpolated damping for varying Young's Modulus values over penetration. The extrapolated parts and identified functions are represented by solid dots. The interpolated functions are represented by dashed lines.

These stiffness and damping functions vary significantly depending on the penetration. Therefore, when testing these functions for stability, it is important to test for stability at different penetrations, as the stability may vary significantly depending on the penetration. For the stability tests, a low penetration of 0.01 m, and a high penetration of 0.02 m, will each be tested to ensure the varying stiffness and damping over penetration is considered.

The position and force for each physical gel simulated in the VE for the lower penetration experiments is shown in Figure 3.4.2-3 and for the higher penetration experiments in Figure 3.4.2-4.

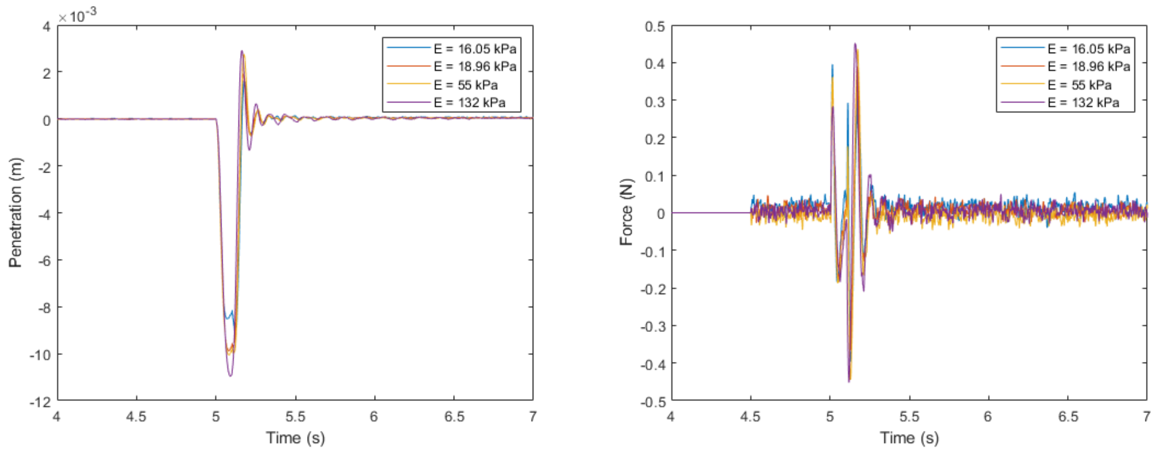

(a) Position responses for all virtual gel models. *(b) Force responses for all virtual gel models.*

Figure 3.4.2-3: Position and force responses in the VE for smaller penetration.

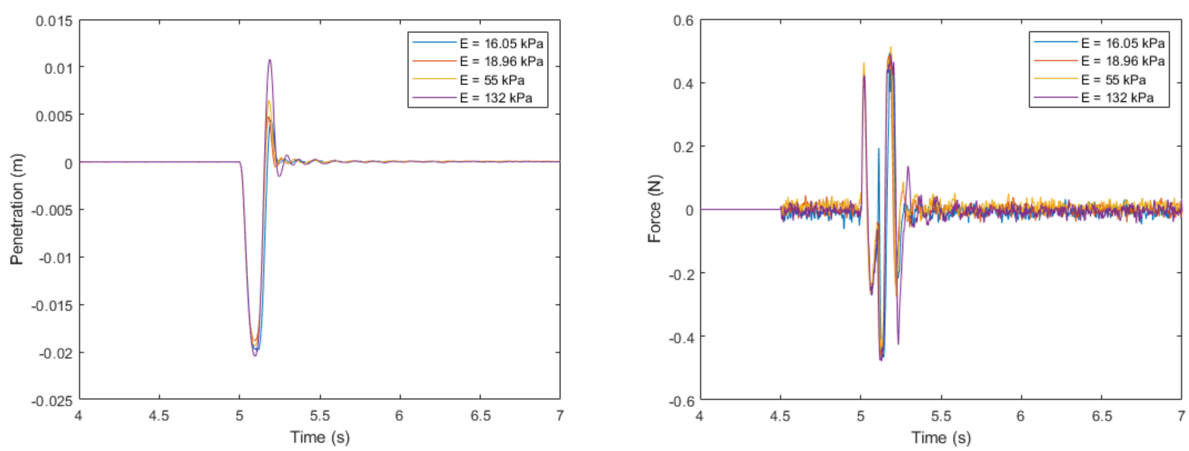

(a) Position responses for all virtual models. *(b) Force responses for all virtual gel models.*

Figure 3.4.2-4: Position and force responses in the VE for larger penetration.

The time profile of the equivalent stiffness and damping for each physical gel simulated in the VE for the lower penetration experiments is shown in Figure 3.4.2-5, and Figure 3.4.2-6 for the higher penetration experiments. This equivalent stiffness and damping are the stiffness and damping from the fitted and interpolated functions.

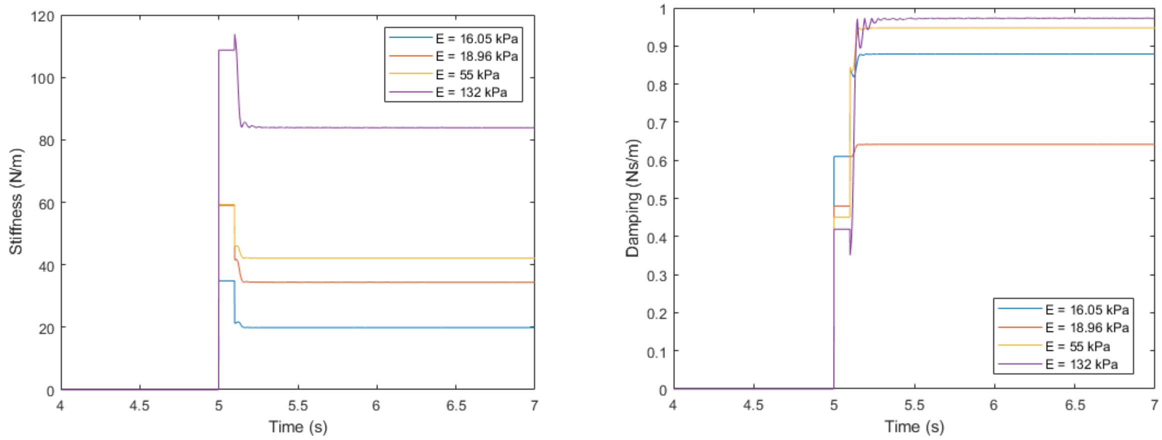

(a) Mesh stiffness responses for all gels. *(b) Mesh damping responses for all gels.*

Figure 3.4.2-5: Mesh stiffness and damping responses in the VE for smaller penetration.

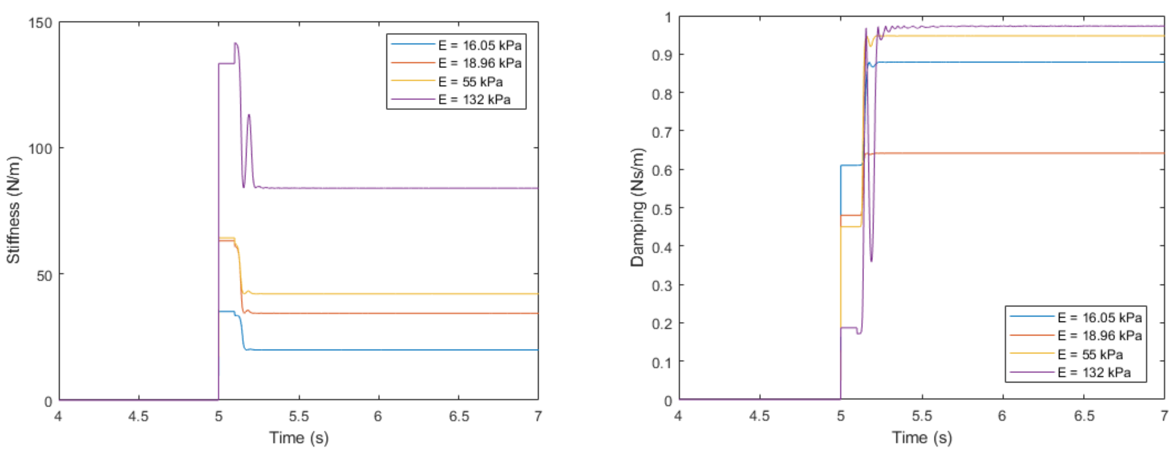

(a) Mesh stiffness responses for all gels. *(b) Mesh damping responses for all gels.*

Figure 3.4.2-6: Mesh stiffness and damping responses in the VE for larger penetration.

3.5 Stability of Haptic Simulation System

3.5.1 Uncoupled Stability Experimental Procedure

To test for the stable implementable range of stiffness and damping in the virtual environment, each damping function must be tested with each stiffness function. The limits of damping tested were chosen to be slightly lower and slightly higher than the damping range from the physical gels. The limit of stiffness tested for each damping function will depend on the stability for that set. The stiffness functions used in the experiment will be K_0 = 20, 34, 42, 84 N/m up until the highest stiffness function that is stable for each damping function. These stiffness functions will be compared for each of the following damping functions, B_0 = 0.3, 0.4, 0.5, 0.642, 0.735, 0.879, 0.948, 0.955, 0.962, 0.973, 1.05, 1.1, 1.15, and 1.2 Ns/m.

For each damping function, each stiffness function will be considered implementable if it meets the stability criteria. If the amplitude of oscillation is less than 2% of the initial position, the stiffness function being tested for that specific damping function is considered stable. If the amplitude of oscillation is greater than 2% of the initial position, the stiffness function for that specific damping function is considered unstable, and the limit of stable implementable stiffness for that specific damping has been reached.

An example of stable and unstable stiffness for a specific damping is shown for the small penetration case, in Figure 3.5.1-1

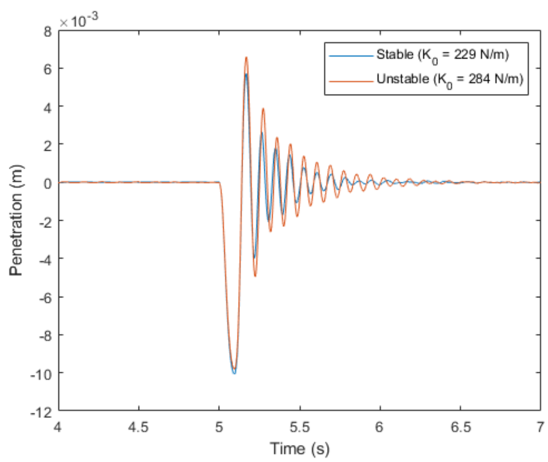

(a) Position responses for B_0 = 0.973 Ns/m.

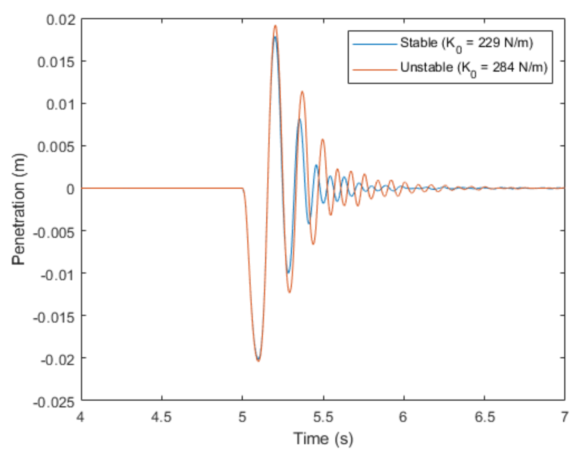

(b) Position responses for B_0 = 0.948 Ns/m.

Figure 3.5.1-1: Stable and unstable position responses for low (left) and high (right) initial penetrations.

The corresponding forces for these penetration and stability cases are shown in Figure 3.5.1-2

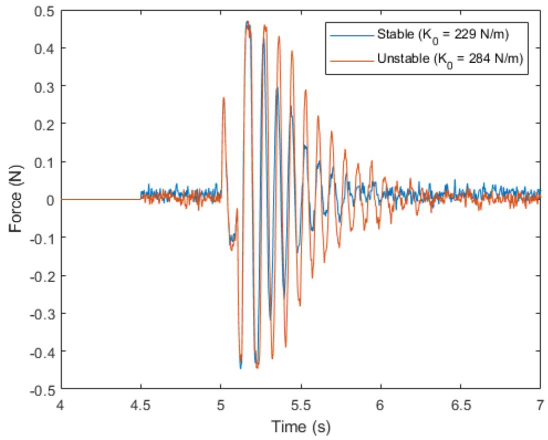

(a) Force responses for B_0 = 0.973 Ns/m.

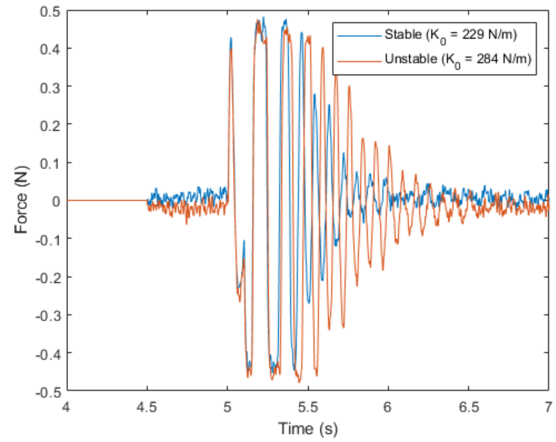

(b) Force responses for B_0 = 0.948 Ns/m.

Figure 3.5.1-2: Force responses for stable and unstable cases for low (left) and high (right) penetrations.

3.5.2 Uncoupled Stability Results and Analysis

The uncoupled stability results from the VE uncoupled stability tests are shown in Table 3.5.2-1 for small penetration, and in Table 3.5.2-2 for large penetration. The green shows the stable stiffness and damping function combinations, and the red shows the unstable stiffness and damping combinations, using the stability criteria described in Section 3.5.1.

Table 3.5.2-1: Stability results for varying damping and stiffness functions, shown with the initial stiffness and damping values of each function, for small penetration (0.01 m). The green combinations show stability, and the red combinations show instability.

K_0 (N/m) / B_0 (Ns/m)	20	34	42	84	121	175	229	243	256	270	275	284	297
0.3													
0.4													
0.5													
0.642													
0.735													
0.879													
0.948													
0.955													
0.962													
0.973													
1.05													
1.1													
1.15													
1.2													

Table 3.5.2-2: Stability results for varying damping and stiffness functions, shown with the initial stiffness and damping values of each function, for large penetration (0.02 m). The green combinations show stability, and the red combinations show instability.

K_0 (N/m) / B_0 (Ns/m)	20	34	42	84	121	175	229	243	256	270	275	284	297
0.3													
0.4													
0.5													
0.642													
0.735													
0.879													
0.948													
0.955													
0.962													
0.973													
1.05													
1.1													
1.15													
1.2													

These stability results are summarized in Figure 3.5.2-1. The stable stiffness for each damping value is the area under and including the stability limit points. The physical gels are shown with this range in Figure 3.5.2-2, showing that they are within the stability range. This range is shown with the upper limits of stiffness from each of the stiffness functions for small and large penetration in Figure 4.5.2-3. This range indicates the implementable stable range of stiffness and damping for deformable objects of similar properties to these viscoelastic gels; however, this range may not accurately represent deormable objects with different dynamic properties.

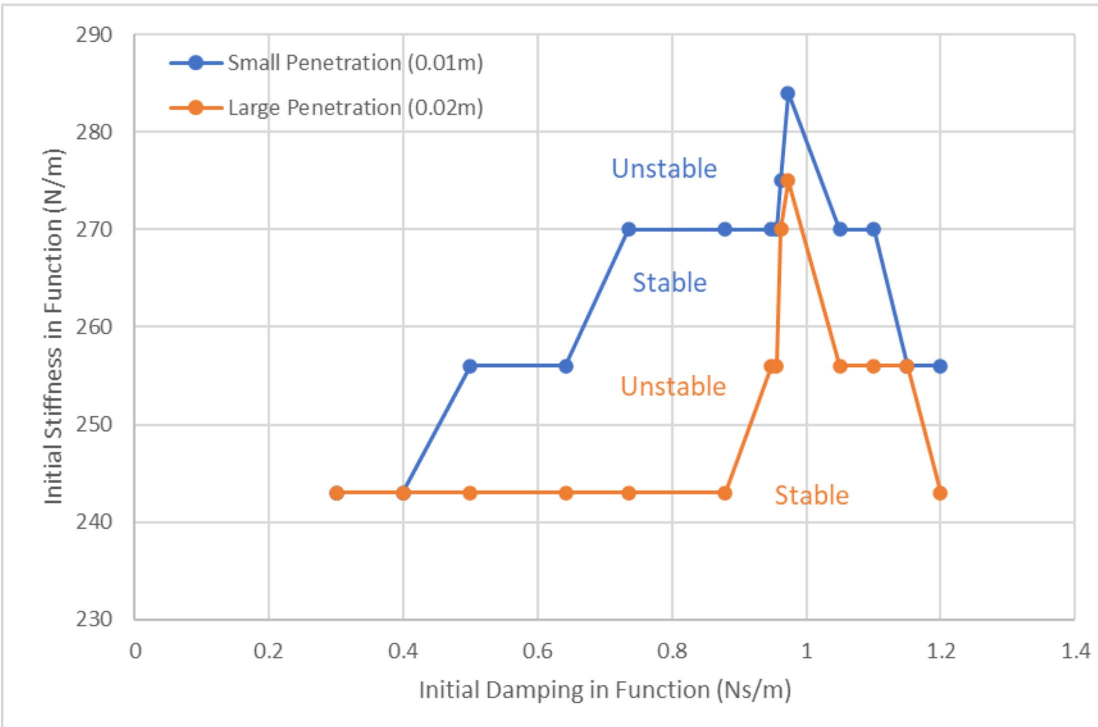

Figure 3.5.2-1: Limits of stability for stiffness vs damping functions. The function sets are stable for all area under and including the stability limit points.

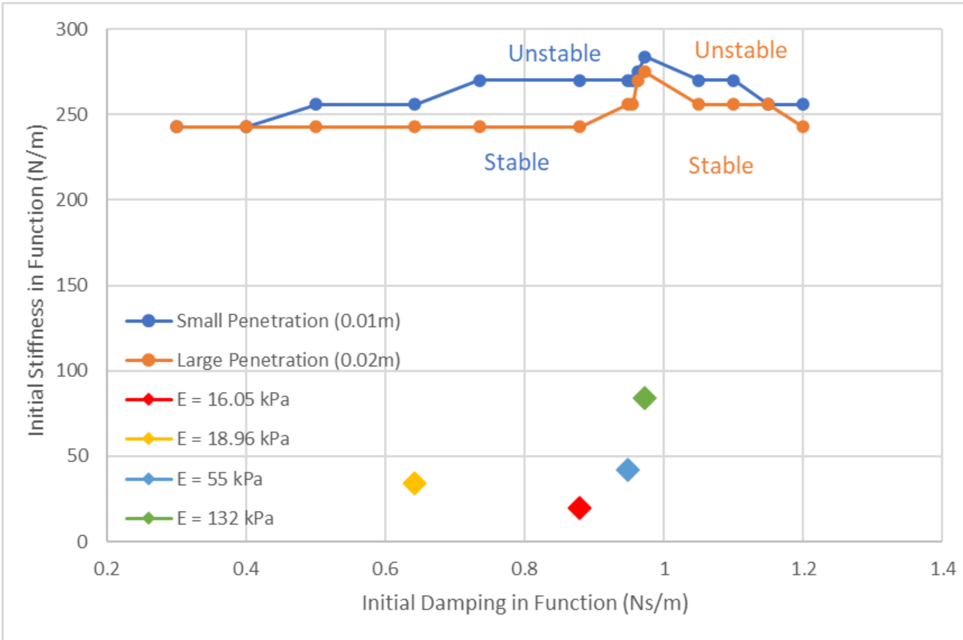

Figure 3.5.2-2: The physical gels shown in the stability range determined from the uncoupled stability testing.

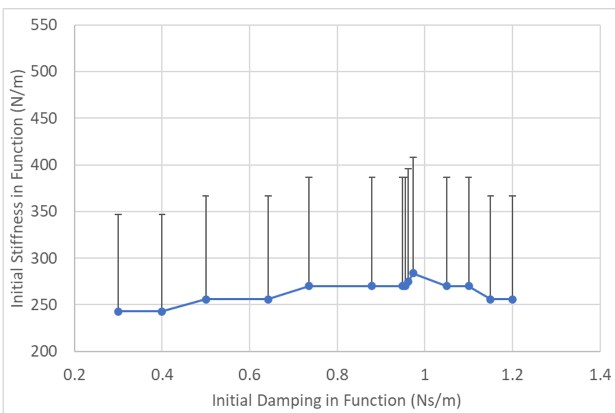

(a) Small penetration.

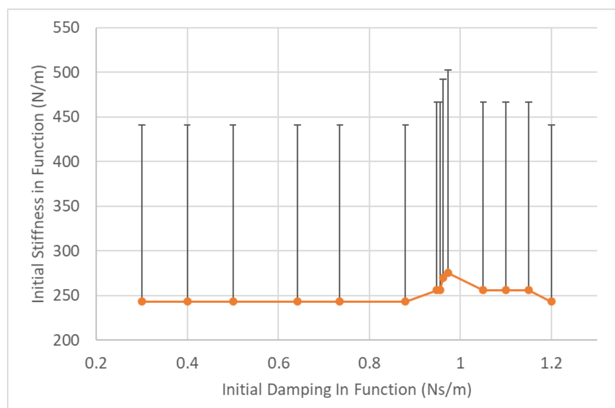

(b) Large Penetration.

Figure 3.5.2-3: Limits of stability for stiffness vs damping functions with data bars showing the range of stiffness of each of the stiffness functions.

From these results, it is clear that as penetration increases, the limits of stability decrease. This is likely because as penetration increases, stiffness increases according to the stiffness functions. Since the stiffness and penetration are increasing, the force increases and causes instability. In general, as the damping increases, the associated stiffness increases to a certain point, and then decreases.

3.5.3 Validation Results and Analysis

To validate the stability results, three alternate gels of varying stiffness were tested using the procedure from Section 3.5.1, and the position and force data is shown in Figure 3.5.3-1.

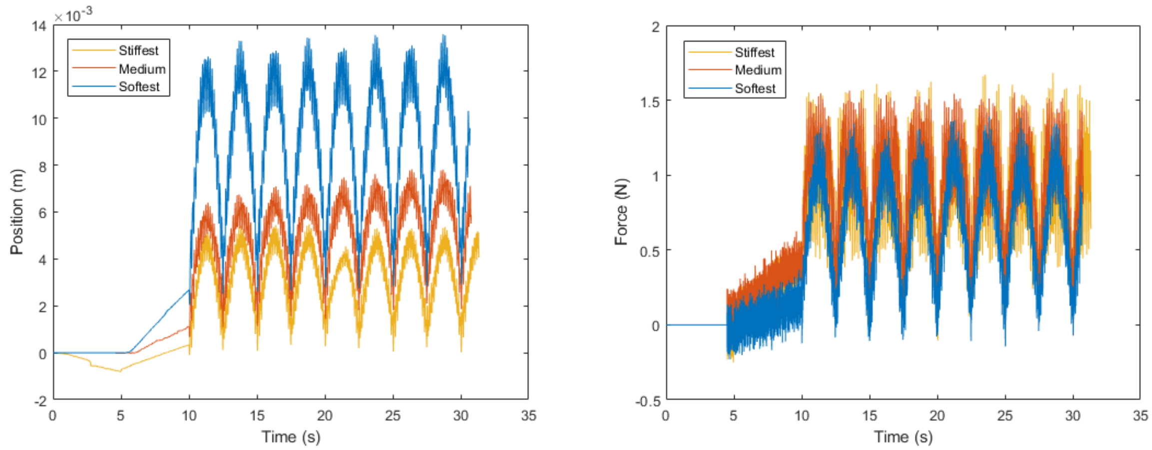

(a) Position data. *(b) Force data.*

Figure 3.5.3-1: Position and force data from the physical uncoupled stability tests.

The stiffness and damping values were found using the identification from Section 3.2.1, and these properties are shown in Figure 3.5.3-2 along with the fitted functions. During the physical penetration testing of these new gels, all had stable uncoupled interactions. The stiffest gel was identified to have negative damping. It is likely that this gel was identified to have negative damping for certain penetration because since the gel was so stiff, the Pantograph could not maintain the desired frequency when interacting with this gel; therefore, the velocity data was not rich enough for identification. Therefore, the damping data is not reliable. Although the stiffest gel was identified to have negative damping for certain penetration, the stiffness component is the primary contributor to the force; therefore, the damping when implementing the VE is not a contributor in the dynamic behaviour.

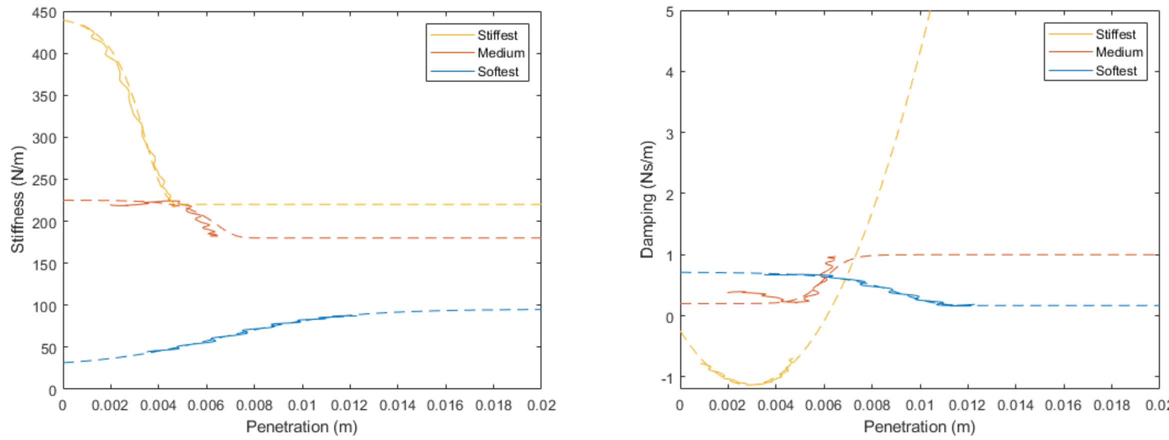

(a) *Stiffness.*

(b) *Damping.*

Figure 3.5.3-2: Stiffness and damping found from identification, with the fitted functions.

Each of these three stiffness and damping parameter sets were used in the uncoupled stability tests, and the penetration and force results are shown in Figure 3.5.3-3 for the small penetration tests, at 0.01 m, and Figure 3.5.3-4 for the large penetrations tests, at 0.02 m.

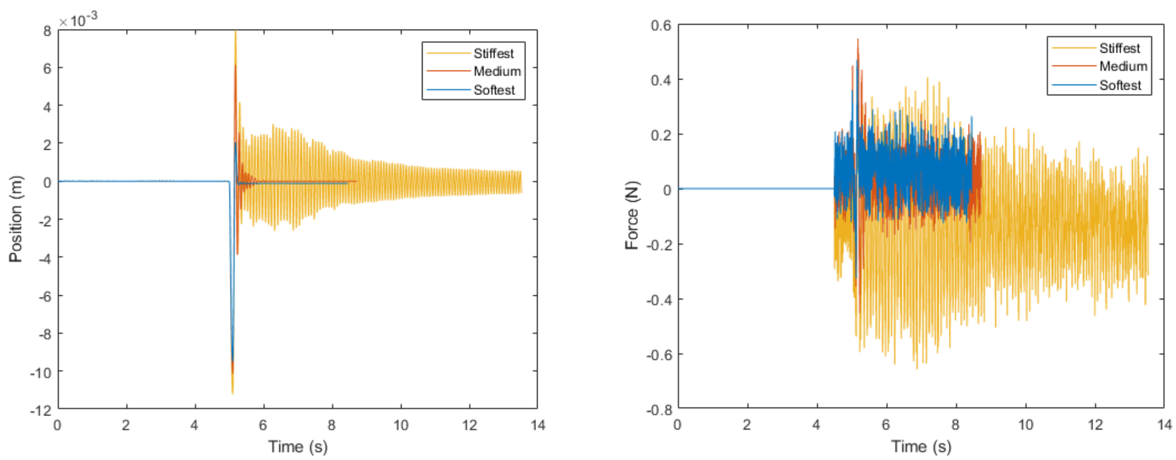

(a) Position responses for new validation gels.

(b) Force responses for new validation gels.

Figure 3.5.3-3: Position and force responses in the VE for smaller penetration.

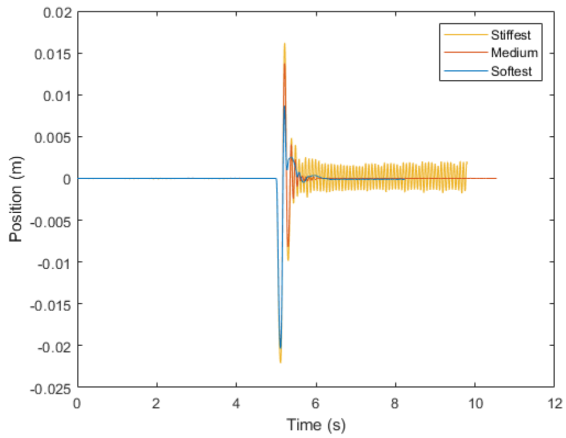

(a) *Position responses for new validation gels.*

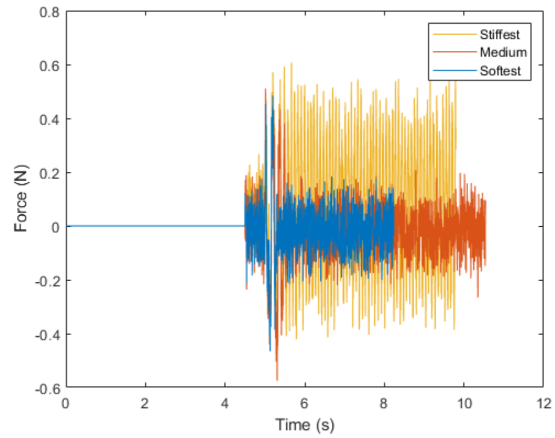

(b) *Force responses for new validation gels.*

Figure 3.5.3-4: Position and force responses in the VE for larger penetration.

The soft and medium gels had stable interactions, and the stiff gel had an unstable interaction, which validates the stability results as these soft and medium gels were within the stable range found, and the stiff gel was outside of this range, shown in Figure 3.5.3-5.

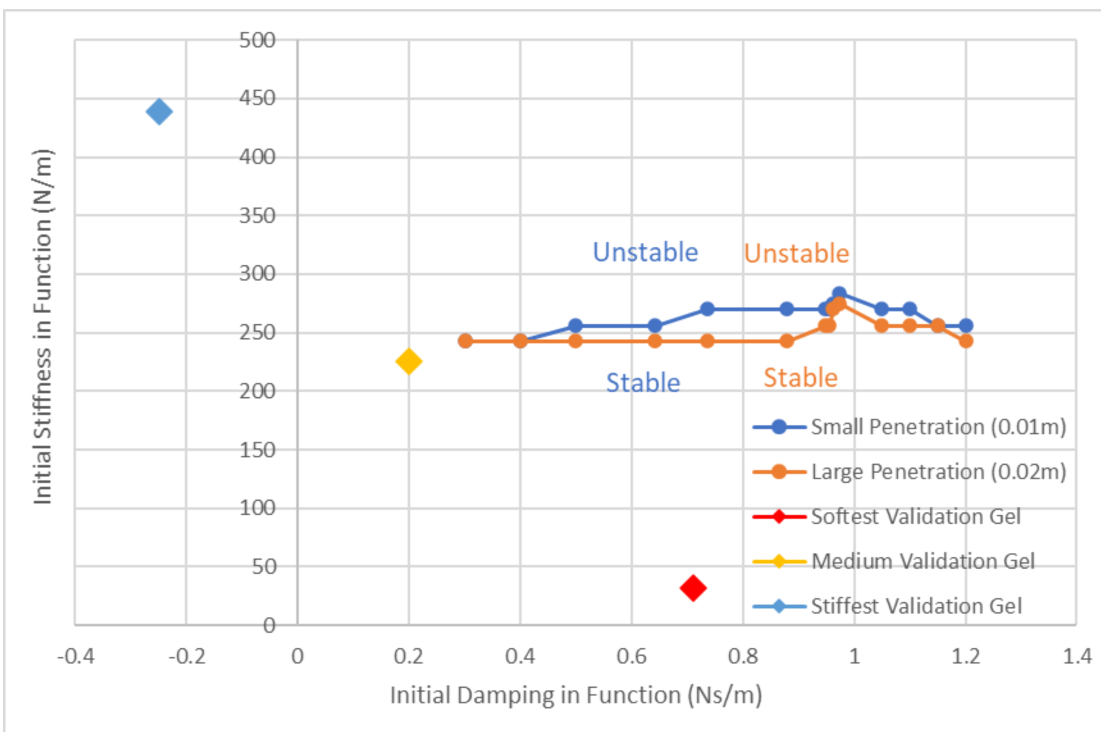

Figure 3.5.3-5: The validation gels shown in the stability range determined from the uncoupled stability testing.

The stiff gel has a stable physical uncoupled interaction, as shown in Figure 3.5.3-1, but had an unstable uncoupled interaction when implemented as a VE. The unstable interaction from the stiff gel shows how stiffer materials cannot be implemented in a VE, as they are well outside the stability range and result in uncoupled instability.

3.6 Summary

In this chapter, four fabricated gels were used in physical uncoupled stability tests, and the parameters from this testing was used in batch LS to determine the stiffness and damping properties of these gels. The properties were mapped to a mesh, using a proposed stiffness and proposed damping mapping equation. This mesh was implemented as a VE and tested for uncoupled stability for both low and high penetration. The implementable stability range of stiffness and damping for this mesh VE was determined for both low and high penetration.

To validate this range, three validation gels of varying stiffnesses were used in the physical uncoupled stability tests, and the stiffness and damping parameters were again found through batch LS. The two softer gels were found to have stiffness and damping parameters within the stable implementable range for both low and high penetration, but the stiffer gel was found to have parameters outside of these stable ranges.

These gels were implemented in the mesh VE. It was found that the two softer gels had stable uncoupled interactions in the mesh VE for both low and high penetration, validating the range as their parameters show they are within the stable range. The stiffer gel has an unstable interaction in the mesh VE for both low and high penetration, again validating the range as the stiffness and damping parameters of this gel were outside of the stable range.

Therefore, the uncoupled stable implementable range of stiffness and damping in a VE found in this chapter is accurate.

Chapter 4

Conclusions

4.1 Summary

In Chapter 1, the existing literature regarding haptic simulations systems, virtual environments, and deformable and non-deformable objects was reviewed. The current models and implementation, and dynamic parameter identification methods were discussed. Finally, the current stability conditions for haptic simulation systems were reviewed, which included a discussion on passivity, implementable dynamic parameter ranges, and uncoupled stability.

In Chapter 2, the HC modeled VE uncoupled stability conditions in a haptic simulation system were experimentally determined. A dynamic parameter mapping scheme was proposed to identify the equivalent KV dynamic parameters.

The mapped experimental uncoupled stability range for the varying n_{HC} at each penetration were determined, and it was found that for each individual penetration, the stiffness range increased slightly, and the damping range decreased significantly for each n_{HC} increment of 0.25. This suggests that higher values of n_{HC} are more suitable for interactions with stiffer environments, at the expense of damping. Compared to the dynamic range obtained from using KV virtual environment, the HC model offers lower stiffness but higher damping range.

A user study found that varying the penetration showed that different penetrations may not affect the stable HC elastic and viscous ranges, but it affects the feel of the HC modeled environment. This confirms that the HC model is penetration dependent.

This range compared the uncoupled stable implementable HC parameters to that of the KV model for nonlinear and linear models, respectively, for non-deformable VEs. However, the uncoupled stable implementable stiffness and damping parameters for deformable objects is also important when determining the implementable range of dynamics in a VE for haptic simulation systems.

In Chapter 3, the properties of four physical gel were determined through experiment and identification. These properties were mapped to a mesh, which was implemented as a VE for uncoupled stability tests for both low and high penetration. It was found that the for the smaller penetration, the stability range included larger stiffness values than the larger penetration. For both small and large penetration, it was found that as damping increased, the stiffness increased up until a certain point, and then decreased, as was found in the stability testing conducted in Chapter 2.

To validate this range, three alternate gels of varying stiffnesses were physically interacted with to find the stiffness and damping, which were used in the VE for the uncoupled stability test. The two softer gels had stiffness and damping properties within the stable implementable range for both low and high penetration, and in the uncoupled stability tests, both were found to be stable, validating the stability range. The stiffer gel had stiffness and damping properties well outside of the stable implementable range for both low and high penetration, and from the uncoupled stability tests, it was found to be unstable, again validating the stability range. This also shows that although the physical interaction was stable, the same interaction in the VE for the same gel properties was unstable, showing that stiffer environments in VE can have unstable uncoupled interactions.

4.2 Future Work

In this work the mesh links were modeled by the KV model; in future work, the HC model could be expanded into deformable object modelling, which could include the mesh representation. The stability ranges for the KV model compared to that of the HC model could be determined for deformable object uncoupled stability testing.

In future, the 2D mesh model can be expanded to a 3D mesh model. This may provide a more accurate representation of the physical gel. This will also provide a better representation of how the physical gel would deform. This would also allow the physical gel interaction to not be restricted to a line of contact interaction and could instead be a point of contact interaction at any point on the gel and would still be able to be simulated in the mesh interaction.

The mesh could also be adjusted in future works to include more nodes, and the accuracy of this mesh simulation compared to the physical gel interaction could be compared for different number of nodes, to determine how the number of nodes affects the accuracy.

Bibliography

[1] C. A. Perez-Gomez, J. U. LICEAGA-CASTRO and I. I. SILLER-ALCALA, "Comparative Study Between Classical Controllers and Inverse Dead Zone Control for Position Control of a Permanent Magnet DC Motor with Dead zone," *WSEAS TRANSACTIONS on POWER SYSTEMS,* vol. 15, pp. 180-190, 2020.

[2] "Quanser Targets Library," Quanser, 13 September 2023. [Online]. [Accessed 20 September 2023].

[3] A. Pappalardo, A. Albakri, C. Liu, L. Bascetta, E. De Momi and P. Poignet, "Hunt–Crossley model based force control for minimally invasive robotic surgery," *Biomedical Signal Processing and Controls,* vol. 29, pp. 31-43, 2015.

[4] K. X. Khor, P. J. H. Chin, H. A. Rahman, C. F. Yeong, E. L. M. Su and A. L. T. Narayanan, "A novel haptic interface and control algorithm for robotic rehabilitation of stoke patients," in *Proceedings of IEEE Haptics Symposium*, 2014.

[5] A. M. Tahmasebi, K. Hashtrudi-Zaad, D. Thompson and P. Abolmaesumi, "A Framework for the Design of a Novel Haptic-Based Medical Training Simulator," *IEEE Transactions on Information Technology in Biomedicine,* vol. 12, no. 5, pp. 658-666, 2008.

[6] J. Ko, S.-w. Jang and Y.-S. Kim, "Development of epiduroscopy training simulator using haptic master device," in *Proceedings of 14th International Conference on Ubiquitous Robots and Ambient Intelligence*, 2017.

[7] B. Hannaford and J.-H. Ryu, "Time-domain passivity control of haptic interfaces," *IEEE Transactions on Robotics and Automation,* vol. 18, no. 1, pp. 1-10, 2002.

[8] B. Hannaford and R. J. Adams, "Stable haptic interaction with virtual environments," *IEEE Transactions on Robotics and Automation,* vol. 15, no. 3, pp. 465-474, 1999.

[9] S. Sadeghnejad, M. Esfandiari, F. Farahmand and G. Vossoughi, "Phenomenological contact model characterization and haptic simulation of an endoscopic sinus and skull base surgery virtual system," in *Proceedings of 4th International Conferece on Robotics and Mechatronics*, 2016.

[10] M. Esfandiari and F. Farahmand, "EMG-Based Neural Network Model of Human Arm Dynamics in a Haptic Training Simulator of Sinus Endoscopy," in *Proceedings of IEEE International Conference on Robotics and Automation*, 2021.

[11] J. E. Colgate and G. G. Schenkel, "Passivity of a class of sampled-data systems: Application to haptic interfaces," *Journal of Robotic Systems*, vol. 14, no. 1, pp. 37-47, 1997.

[12] N. Diolaiti, C. Melchiorri and S. Stramigioli, "Contact impedance estimation for robotic systems," *IEEE Transactions on Robotics,* vol. 21, no. 5, pp. 925-935, 2005.

[13] G. Gilardi and I. Sharf, "Literature survey of contact dynamics modelling," *Mechanism and Machine Theory,* vol. 37, no. 10, pp. 1213-1239, 2002.

[14] H. Kolbari, S. Sadeghnejad, M. Bahrami and A. Kamali, "Bilateral adaptive control of a teleoperation system based on the hunt-crossley dynamic model," in *Proceedings of RSI International Conference on Robotics and Mechatronics*, 2015.

[15] Y. Huang, P. Souères and J. Li, "Contact dynamics of massage compliant robotic arm and its coupled stability," in *Proceedings of IEEE International Conference Robotics and Automation,* 2014.

[16] F. Courreges, M. Laribi, M. Arsicault and S. Zeghloul, "An in Vivo Experiment to Assess the Validity of the Log Linearized Hunt-Crossley Model for Contacts of Robots with the Human Abdomen," in *Proceedings of Robotics and Mechatronics,* 2016.

[17] X. Zhu, B. Gao, Y. Zhong, C. Gu and K.-S. Choi, "Extended Kalman filter for online soft tissue characterization based on Hunt-Crossley contact model," *Journal of the Mechanical Behavior of Biomedical Materials,* vol. 123, p. 104667, 2021.

[18] A. Haddadi and K. Hashtrudi-Zaad, "A new method for online parameter estimation of Hunt-Crossley environment dynamic models," in *2008 IEEE/RSJ International Conference on Intelligent Robots and Systems,* Nice, France, 2008.

[19] A. Haddadi and K. Hashtrudi-Zaad, "Real-Time Identification of Hunt–Crossley Dynamic Models of Contact Environments," *IEEE Transactions on Robotics,* vol. 28, no. 3, pp. 555-66, 2012.

[20] F. Barbagli, K. Salisbury and D. Prattichizzo, "Dynamic local models for stable multi-contact haptic interaction with deformable objects," in *11th Symposium on Haptic Interfaces for Virtual Environment and Teleoperator Systems, 2003. HAPTICS 2003. Proceedings.*, 2003.

[21] D. Deo and S. De, "A higher order polynomial reproducing radial basis function neural network (HOPR-RBFN) for real-time interactive simulations of nonlinear deformable bodies with haptic feedback," in *2010 IEEE Haptics Symposium,* 2010.

[22] G. Schillhuber and H. Ulbrich, "Haptic Simulation of Deformable Bodies with Consideration of the Human Sensation of Continuous Forces," in *2008 Symposium on Haptic Interfaces for Virtual Environment and Teleoperator Systems,* 2008.

[23] M. Bro-Nielsen, "“Finite element modeling in surgery simulation," *Proceedings of the IEEE,* vol. 86, no. 3, pp. 490-503, 1988.

[24] S. Cotin and H. Delingette, "Real-time surgery simulation with haptic feedback using finite elements," *Proceedings. 1998 IEEE International Conference on Robotics and Automatio,* vol. 4, pp. 3739-3744, 1998.

[25] S. DiMaio and S. E. Salcudean, "Needle Insertion Modeling and Simulation," *IEEE Transactions on Robotics and Automation,* vol. 19, no. 5, pp. 864-875, 2003.

[26] D. Cleveland and K. Hashtrudi-Zaad, "The effect of discretization techniques on uncoupled stability of haptic simulation systems," in *2018 IEEE Haptics Symposium (HAPTICS)*, 2018.

[27] L. Pecly and K. Hashtrudi-Zaad, "Uncoupled Stability of Kinesthetic Haptic Systems Simulating Mass-Damper-Spring Environments with Complementary Filter," in *2022 IEEE/ASME International Conference on Advanced Intelligent Mechatronics (AIM)*, Sapporo, Japan, 2022.

[28] V. Luna, D. Cleveland and K. Hashtrudi-Zaad, "Uncoupled Stability of a Haptic System with Position-Velocity Sampling," 2019 IEEE World Haptics Conference (WHC)," in *2019 IEEE World Haptics Conference (WHC)*, Tokyo, Japan, 2019.

[29] K.-S. Choi, H. Sun and P.-A. Heng, "Interactive Deformation of Soft Tissues With Haptic," *IEEE Transactions on Information Technology n Biomedicine,* vol. 7, no. 4, pp. 358-363, 2003.

[30] J. E. Colgate and N. Hogan, "Robust control of dynamically interacting systems," *International Journal on Control,* vol. 48, no. 1, pp. 65-88, 1988.

[31] M. Xia, P. J. Antsaklis and V. Gupta, "Passivity Analysis of Human as a Controller," University of Notre Dame, 2014.

[32] V. A. Luna, D. Cleveland and K. Hashtrudi-Zaad, "Uncoupled Stability of a Haptic System with Position-Velocity Sampling," in *Proceedings of IEEE World Haptics Conference,* 2019.

[33] D. Cleveland and K. Hashtrudi-Zaad, "The effect of discretization techniques on uncoupled stability of haptic simulation systems," in *Proceedings of IEEE Haptics Symposium,* 2018.

[34] J. J. Gil, A. Avello, A. Rubio and J. Florez, "Stability analysis of a 1 DOF haptic interface using the Routh-Hurwitz criterion," *IEEE Transactions Control Systems Technology,* vol. 12, no. 4, pp. 583-88, 2004.

[35] V. A. Luna, P. Gizem Ozdil and K. Hashtrudi-Zaad, "Effect of Direct Velocity Measurement on the Stability of Haptic Simulation Systems," in *Proceedings of IEEE Haptics Symposium*, 2020.

[36] L. Pecly and K. Hashtrudi-Zaad, "Uncoupled Stability Evaluation for Haptic Interaction with Hunt-Crossley Virtual Environments," in *2020 Haptic Symposium*, 2020.

[37] L. S. D. Pecly, M. L. O. Souza and K. Hashtrudi-Zaad, "Offline and online synchronization of position derived signals for identification of dynamic systems," in *Proceedings of Latin American Robotics Symposium*, 2017.

[38] K. J. Kuchenbecker, D. Ferguson, M. Kutzer, M. Moses and A. M. Okamura, "The Touch Thimble: Providing Fingertip Contact Feedback During Point-Force Haptic Interaction," in *Proceedings of Symposium on Haptic Interfaces for Virtual Environment and Teleoperator Systems*, 2008.

[39] B. Khademian and K. Hashtrudi-Zaad, "Novel shared control architectures for enhanced users' interaction in haptic training simulation systems," in *Proceedings of IEEE/RSJ International Conference on Intelligent Robotics and Systems*, 2009.

[40] B. Khademian and K. Hashtrudi-Zaad, "Experimental performance evaluation of a haptic training simulation system," in *Proceedings of IEEE/RSJ International Conference on Intelligent Robotics and Systems*, 2009.

[41] "M-F Manufacturing," M-F Manufacturing Company, 2023. [Online]. Available: https://www.m-fmanufacturing.com/. [Accessed 6 October 2023].

[42] A. Baghani, H. Eskandari, S. Septimiu and R. Rohling, "Measurement of Viscoelastic Properties," *IEEE Transactions on Ultrasonics, Ferroelectrics, and Frequency Control,* vol. 56, no. 7, pp. 1405-1418, 2009.

[43] A. Smith, F. Mobasser and K. Hashtrudi-Zaad, "Neural-Network-Based Contact Force Observers for Haptic Applications," *IEEE Transactions on Robotics,* vol. 22, no. 6, pp. 1163-1175, 2006.

[44] B. Khademian and K. Hashtrudi-Zaad, "Dual-User Teleoperation Systems: New Multilateral Shared Control Architecture and Kinesthetic Performance Measures}," *EEE/ASME Transactions on Mechatronics,* vol. 17, no. 5, pp. 895-906, 2012.

[45] A. Manurung, "GitHub," 8 June 2021. [Online]. Available: https://github.com/auralius/matlab-mass-spring-damper-network-deformable-object.

[46] "MF Manufacturing Company," MF Manufacturing Company, [Online]. Available: https://www.facebook.com/pouryourownworms/. [Accessed 23 April 2023].

[47] S. M. Oliver, K. Hashtrudi-Zaad and L. S. D. Pecly, "Uncoupled Stability Dynamic Range for Kelvin-Voigt and Hunt-Crossley Virtual Environments," in *EuroHaptics*, 2022.

[48] C. Liu, J. Guo and P. Poignet, "Nonlinear Model-Mediated Teleoperation for Surgical Applications under Time Variant Communication Delay," *IFAC-PapersOnLine,* vol. 51, no. 22, pp. 493-499, 2018.

[49] C. Xiaojun, L. Yanping, W. Chengtao, W. Yiqun, W. Xudong and S. Guofang, "“An integrated surgical planning and virtual training system using a force feedback haptic device for dental implant surgery," *Proceedings of IEEE International Conference on Audio Language and Image Processing*, pp. 1257-1261, 2010.

Appendix A

Spring-damper Mesh

Table 4.2-1: Parameters and their relation to the mesh components.

Parameter	Relation
K	Stiffness in the link
B	Damping in the link
F	Force the link is applying
K_y	Stiffness of the link in the vertical direction
B_y	Damping of the link in the vertical direction
F_y	Force the link is applying in the vertical direction
L	Length of the link before deformation
L'	Length of the link at the current time step in deformation
L'_x	Length of the horizontal component of the link at the current time step in deformation
L'_y	Length of the vertical component of the link at the current time step in deformation
ΔL	Change in length of the link since deformation began
ΔL_y	Change in the vertical component of length of the link since deformation began
x_1	Horizontal position of the first node
y_1	Vertical position of the first node
x_2	Horizontal position of the second node
y_2	Vertical position of the second node
α, β	Angles between the link and horizontal axis at current time step in deformation
y	Total vertical deformation at current time step
y_{prev}	Total vertical deformation at previous time step

Δt	Time step
$\Delta\dot{L}$	Difference between the change in the total length of the link at the current time and that of the previous time step overt the difference in time
$\Delta\dot{L}_y$	Difference between the change in the total length of the link in the vertical component at the current time step and that of the previous time step overt the difference in time
L'_{prev}	Length of the link at the previous time step in deformation
$L'_{y,prev}$	Length of the vertical component of the link at the previous time step in deformation